Improving the Reconstruction of Neutral Pions in Tau Decays Using the Strip Layer of the ATLAS Electromagnetic Calorimeter

Stephanie P. Yuen

Masterarbeit in Physik
angefertigt im Physikalischen Institut

vorgelegt der
Mathematisch-Naturwissenschaftlichen Fakultät
der
Rheinischen Friedrich-Wilhelms-Universität
Bonn

Oktober 2013

1. Gutachter: Prof. Dr. Jochen Christian Dingfelder
2. Gutachter: Prof. Dr. Klaus Desch

Acknowledgements

I express my gratitude to my supervisor, Professor Jochen Dingfelder, without whom this thesis would not be possible. I am indebted to Jochen for the opportunity to conduct valuable research and could not be prouder of my academic roots in the Dingfelder group at Bonn. He has not only imparted his knowledge of physics, but also what it means to educate and to lead. I could not wish for a better supervisor.

I also thank my co-supervisors and officemates, Dr. Will Davey and Benedict Winter, both of whom never hesitated to share their passion for physics and to teach, by example, what it means to be a physicist. I am especially grateful to Benedict for his help with German-related things and for sharing the opportunity to work on the cell-based algorithm. The clarity of his explanations during spontaneous discussions in the office helped me avoid potential *Verschlimmbesserungen*. I could not have asked for a more supportive colleague.

Lastly, I thank my family and friends. Despite being far away, my family has been an invaluable and constant source of support and stability. And I cannot thank the friends I have made in Bonn enough for helping me to create a work-life balance during my past two years in Germany.

Contents

Introduction 1

1 Theoretical Background 3

1.1 The Standard Model of Particle Physics . . . 3

1.1.1 Shortcomings of the Standard Model . . . 6

1.2 Properties of the Tau Lepton . . . 6

1.3 Polarization Studies with Tau Leptons . . . 7

2 The ATLAS Experiment at the Large Hadron Collider 13

2.1 Overview of the LHC . . . 13

2.2 Overview of the ATLAS Detector . . . 15

2.2.1 The Coordinate System . . . 16

2.3 The Inner Detector . . . 17

2.4 The Calorimeter System . . . 18

2.4.1 The Electromagnetic Calorimeter . . . 19

2.4.2 The Hadron Calorimeter . . . 21

2.4.3 The Forward Calorimeter . . . 21

2.4.4 Calibration of the Calorimeter System . . . 22

2.4.5 Clustering in the Calorimeters . . . 22

3 Tau Leptons in the ATLAS Detector 23

3.1 Tau Reconstruction in ATLAS . . . 23

3.2 Tau Substructure Reconstruction . . . 25

3.2.1 Neutral Pion Reconstruction in the Cell-Based Algorithm . . . 25

4 Improving Neutral Pion Reconstruction Using Strip Layer Information 29

4.1 Data Samples . . . 29

4.1.1 Monte Carlo $Z \rightarrow \tau\tau$ Sample with Pileup . . . 29

4.1.2 Monte Carlo Single π^0 Sample without Pileup . . . 32

4.1.3 Monte Carlo Single $\pi^{\pm}$ Sample without Pileup . . . 33

4.2 Identifying Photons from Tau Decays in the Strip Layer . . . 34

4.2.1 Photon Showers in the Strip Layer from a Hadronically Decaying Tau . . . 36

4.2.2 Local Maximum Finder to Identify Seed Cells for Candidate Photon Shots . . . 38

4.2.3 Truth-Matching of Candidate Shots to True Photons . . . 41

4.2.4 Performance of Shot Seeding . . . 43

4.2.5 Photon Conversions . . . 45

4.3 Improving the Classification of τ Decay Modes by Counting Photons . . . 48

4.3.1 Counting Neutral Pions Using Shots . . . 49

4.3.2 Further Improvements . . . 56

4.4 Development of a New Approach to the Subtraction of $\pi^{\pm}$ Subshowers Using the Strip Layer . . . 62
4.5 Feasibility of an Alternative Approach to π^0 Reconstruction in τ Decays . . . 69
4.5.1 Energy and p_T Resolution . . . 69
4.5.2 Outlook of the Alternative Approach . . . 71

5 Outlook **73**
5.1 Validation between Monte Carlo and Data . . . 73
5.2 Ideas for Further Improvement of the Algorithms Presented in This Thesis . . . 73
5.3 Ideas for Future Uses of the Photon Shot . . . 74

6 Conclusions **75**

A Relevant Properties of the ATLAS Detector **77**
A.1 Segmentation of the Calorimeters at ATLAS . . . 77
A.2 Amount of Material in the ATLAS Detector . . . 78
A.3 Noise in the ATLAS Detector . . . 79

B Variables Used for π^0 cluster Identification in the Cell-Based Algorithm **81**

List of Figures **83**

List of Tables **85**

Bibliography **87**

Introduction

In 2013, the Large Hadron Collider (LHC) concluded Run 1 of collision data-taking at center-of-mass energies of 7 and 8 TeV in 2011 and 2012, respectively. The LHC is now in a two-year hiatus for maintenance and upgrades, in preparation for the second run of collisions at higher energies. Since the beginning of its first three-year run, the LHC has been at the frontier of particle physics, accessing energies in the TeV energy region never before achieved by a man-made accelerator. At this energy scale, physicists are able to better investigate pressing fundamental questions. On July 4th, 2012, the ATLAS and CMS collaborations discovered a new resonance at the LHC in the search for the Standard Model Higgs boson. Other observations at the LHC include observations of quark-gluon plasma, particle-antiparticle mixing in the D meson system, and the rare $B_s \rightarrow \mu^+\mu^-$ decay. Up to the energies that the LHC has reached, it is conclusive that there have been no signs of new physics beyond the Standard Model. The LHC will begin to collide protons at a center-of-mass energy of 13 TeV in 2015, which will allow the experiments to better probe new physics that should manifest at the TeV scale.

Tau leptons play an important role in the physics goals of the LHC. The new particle discovered in 2012 has only been observed in bosonic decay channels, and searches for the decay into two taus will be an important test of the couplings of the Standard Model Higgs boson to elementary fermions. In models beyond the Standard Model, final states with tau leptons are also pertinent because they have enhanced coupling over large regions of parameter space. Another advantage of the tau is that it is the only known lepton whose polarization is experimentally accessible at the LHC. Tau leptons decay in the beam pipe of the LHC, so they are reconstructed from their decay products. The leptonic decay channel of the tau is the cleanest to measure, since muons and electrons leave distinct and easily identifiable signatures in detectors. Tau leptons decay into hadrons over half of the time, predominantly into a low multiplicity of charged and neutral pions. The overwhelming production of hadronic jets at the LHC can fake the signature of hadronically decaying taus. This jet production has a cross section many of magnitudes higher than the signal processes involving taus. The hadronic decay channel of the tau lepton, however, is an important signature in physics analysis of importance at the LHC. The reconstruction of neutral pions from hadronically decaying taus is relevant for physics analyses that have been increasingly making use of tau polarization. Predicting the number of neutral pions, by first subtracting charged pion showers in the detector, is necessary to achieve a good resolution of the reconstructed four-momenta of individual neutral pions because it can better provide the four-momentum reconstruction the correct neutral and charged components to use.

In this thesis, an algorithm is proposed that identifies individual photons that are emitted close to each other in neutral pion decays from tau leptons in the ATLAS detector. The algorithm takes advantage of the fine segmentation of cells in the first layer of the ATLAS electromagnetic calorimeter, since photon showers in that layer are narrow and photons in neutral pion decays from taus are produced in close proximity to each other, especially for tau decays at high momenta. The identification of individual photons is applied to the counting of neutral pions in order to correctly identify the decay mode a tau undergoes, a classification which is important for polarization measurements. In addition, the thesis presents applications for the subtraction of charged pion energy deposits to improve the reconstruction of neutral pions and a test of the feasibility of predicting neutral pion showers by first identifying their daughter photons. The thesis documents the development of algorithms to improve the reconstruction

of neutral pions and the detailed studies their performance in Monte Carlo simulation.
The thesis is structured according to the chapters listed below.

- Chapter 1 provides the theoretical background and motivation for the analyses presented in this thesis. First, the Standard Model of particle physics is introduced. Then, two detailed sections follow focusing on the properties of the tau lepton and polarization studies with tau leptons.
- Chapter 2 gives an overview of the LHC and the ATLAS detector. A description of the tracking system and the calorimeter of the ATLAS detector is provided in more detail since they are the most important detector components for the studies of this thesis.
- Chapter 3 describes the reconstruction and identification of hadronically decaying taus in the ATLAS detector.
- Chapter 4 prefaces the analysis by introducing the data samples used in this thesis. Then, the next sections present the identification of individual photons that are emitted close to each other from a π^0 in a tau decay and the applications of this algorithm.
- Chapter 5 is an outlook describing the prospects for the validation of the algorithms presented in this thesis in data. This chapter also provides ideas for further improvements to the presented algorithms and future applications using the photon identification developed in this thesis.
- Finally, the conclusions of the thesis are given in Chapter 6.

Throughout the chapters, SI units and space-time coordinates, where $c = 1$, are used, unless otherwise noted.

Chapter 1

Theoretical Background

The following chapter provides the theoretical background for the work presented in this thesis. The first section introduces the Standard Model of particle physics (SM), the second section discusses the tau lepton and its decay modes, and the third and final section discusses tau lepton polarization, which is experimentally accessible using the decay kinematics of the tau lepton.

1.1 The Standard Model of Particle Physics

The Standard Model of particle physics is a gauge-invariant, chiral, local quantum field theory that describes the universe in energy ranges currently accessible by experiment. It identifies each constituent particle of ordinary matter and interactions. It also describes three of the four fundamental interactions between these elementary particles. Each particle identified by the Standard Model is uniquely characterized by a set of quantum numbers. The force that is not included in the Standard Model is gravity. For interactions between relativistic particles, gravity can be safely neglected at energies below the Planck scale ($\sim 10^{19}$ GeV) and is many orders of magnitude weaker than the other fundamental forces. Since its development in the 1970s, the Standard Model has been extensively tested by numerous experiments and has been in good agreement with experimental results. The new resonance at $\sim$125 GeV observed in July 2012 by the ATLAS and CMS experiments at the Large Hadron Collider could very likely correspond to the elusive SM Higgs boson, H [1, 2].

The Standard Model identifies the types of elementary particles. They consist of fermions, which have half-integer spin, and bosons, which have integer spin. Each particle has a corresponding antiparticle, which is identical, except for an opposite charge and parity. The antiparticle is a consequence of combining the quantum mechanical description of subatomic particles with special relativity. The interactions between these fermions are mediated by the vector bosons, which are spin-1 particles. The Higgs mechanism is employed in the SM to generate mass terms for the massive vector bosons and the chiral fermions [3]. The Higgs boson is a quantum of the scalar Higgs field and is a spin-0 particle. A summary of the bosons and fermions and their properties is shown in Tables 1.1 and 1.2.

Force	Mediating particle	Mass of Mediating Particle (GeV)	Relative strength	Range (m)
Weak	$W^{\pm}$ bosons	80.385±0.015	10^{-5}	10^{-18}
	Z boson	91.188±0.002		
Electromagnetic	Photon, γ	Massless	10^{-2}	∞
Strong	Gluon, g	Massless	1	10^{-15}

Tab. 1.1: The fundamental forces and their properties. Relative strength is described by the ratio to the strong coupling. Masses are from [4].

The electroweak and strong interactions are invariant under the gauge group SU(3)$_C$⊗SU(2)$_L$⊗U(1)$_Y$, where SU(3) is the gauge symmetry group of the strong interaction, and the weak and electromagnetic interactions are unified in the SU(2)$_L$⊗U(1)$_Y$ symmetry group of the electroweak force. Leptons are fermions coupling to the electromagnetic and weak forces. Quarks are fermions that couple to the strong, electromagnetic, and weak forces. Each of these groups has three generations, where the particles in each generation are identical except for mass. Fermions in the second and third generations are produced in high-energy collisions and subsequently decay into first generation fermions. The charged leptons obey lepton flavor conservation, so electron (muon, tau) decays always have an associated electron- (muon-, tau-) neutrino produced. Neutrino oscillations, where one neutrino flavor can change to another neutrino flavor, violate lepton flavor conservation. Table 1.2 shows the three generations of quarks and leptons, their masses, and their quantum numbers.

Generation	Symbol	Quarks Mass	Charge	Symbol	Leptons Mass	Charge
I	u	≈2.3 MeV	2/3	e	0.511 MeV	-1
	d	≈4.8 MeV	-1/3	ν_e	<2.2 eV	0
II	c	≈1.275 GeV	2/3	μ	105.7 MeV	-1
	s	≈95 MeV	-1/3	ν_μ	<0.17 MeV	0
III	t	≈173.07 GeV	2/3	τ	1.777 GeV	-1
	b	≈4.18 GeV	-1/3	ν_τ	<15.5 MeV	0

Tab. 1.2: The spin-$\frac{1}{2}$ fermions and their properties. Quarks are shown on the left side of the table, and leptons are shown on the right side of the table. Masses are from [4].

The quantum field theory that describes the electromagnetic force is Quantum Electrodynamics (QED). This elementary force is mediated by the massless, electrically neutral photon. The weak force is mediated by the $W^\pm$ and Z bosons, which couple to weak charge. The weak interaction is unified together with the electromagnetic force under an SU(2)⊗U(1) gauge group in the electroweak theory by Glashow, Salem, and Weinberg [5–7]. The electroweak theory defines the weak hypercharge, Y_W, as

$$Y_W = 2(Q - I_3). \tag{1.1}$$

The weak hypercharge connects the third component of the weak isospin, I_3, with the electric charge, Q (units of elementary charge). The corresponding gauge bosons of the electroweak gauge group are eigenstates (W^+, W^0, W^-) of the isospin from SU(2) and the massless B^0 boson of weak hypercharge from U(1). The $W^\pm$ and Z^0 bosons are massive through the breaking of electroweak symmetry according to SU(2)⊗U(1)$_Y$ →U(1)$_{\mathrm{em}}$. The three massive weak bosons that mediate the weak interaction and the photon (gauge field A_μ) are rewritten as linear combinations of the $W^a_{\mu\nu}$ and $B_{\mu\nu}$ gauge fields as

$$W^\pm_\mu = \frac{1}{\sqrt{2}}(W^1_\mu \pm iW^2_\mu) \tag{1.2}$$

$$\begin{aligned} Z_\mu &= W^3_\mu \cos\theta_W - B_\mu \sin\theta_W \\ A_\mu &= W^3_\mu \sin\theta_W + B_\mu \cos\theta_W, \end{aligned} \tag{1.3}$$

where θ_W is the weak mixing angle. The electroweak symmetry occurs at energies above the electroweak scale, ~125 GeV. At energies below this range, the electroweak symmetry is spontaneously broken by the Higgs mechanism [3, 8, 9].

The strong force is described by Quantum Chromodynamics and is mediated by the gluon, as shown in Table 1.1. The strong interaction is described by the SU(3) gauge symmetry group. Quarks (antiquarks) can carry three types of (anti) color charge. Gluons carry a superposition of red, green, or blue and anti red, anti green, or anti blue color charge, and this superposition is given by the Gell-Mann matrices. Color-charged particles exhibit a phenomenon known as color confinement, so they always bind together to form hadrons with zero color charge in the hadronization, or fragmentation, process. Hadrons come in two forms: mesons are formed by quark and antiquark pairs and baryons are formed by quark triplets.

A problematic aspect of the Standard Model is that it predicts the mediators of the weak force to be massless, while experiments have determined the $W^{\pm}$ and Z bosons to be massive [10]. In addition, the cross section of longitudinal WW boson scattering diverges at the TeV scale, and unitarity is violated without the introduction of a scalar field. The masses of the $W^{\pm}$ and Z bosons cannot be generated by adding mass terms to a vector field. Mass terms for the weak bosons are forbidden by gauge invariance, and mass terms for fermions are forbidden by chiral symmetry. The bosons and fermions gain mass, instead, through spontaneous symmetry breaking. Spontaneous symmetry breaking occurs when the state of lowest energy, otherwise known as the vacuum state, is not unique. It is achieved in the electroweak interaction by the introduction of an SU(2) doublet of complex scalar fields,

$$\phi = \frac{1}{\sqrt{2}} \begin{pmatrix} \phi_1(x) + i\phi_2(x) \\ \phi_3(x) + i\phi_4(x) \end{pmatrix}, \tag{1.4}$$

to the Lagrangian to generate a potential $U(\phi)$,

$$U(\phi) = -\frac{1}{2}\mu^2\phi^{\dagger}\phi + \frac{1}{4}\lambda^2(\phi^{\dagger}\phi)^2. \tag{1.5}$$

The potential described in Equation 1.5 is shown in Figure 1.1 for $\mu^2 < 0$. With a potential of this form, the Lagrangian is invariant under rotations in the ϕ_1, ϕ_2 space. The ground state of this potential (e.g., a local minimum at $\frac{v}{\sqrt{2}}$ is stable), and the Lagrangian is invariant under the symmetry of this potential (e.g., reflections in the vertical axis are symmetric), but the ground state is not. The masses of

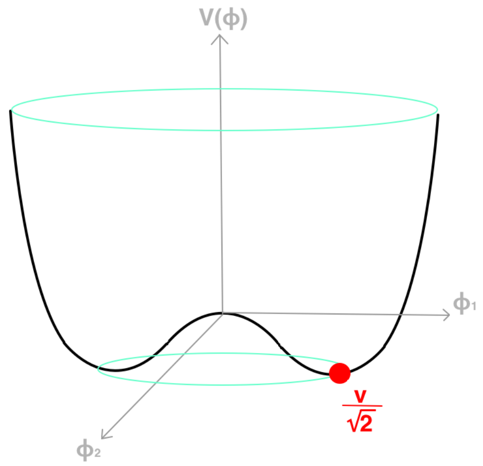

Fig. 1.1: The Higgs Potential described by $U(\phi)$ in Equation 1.5 for $\mu^2 < 0$

.

the $W^{\pm}$ and Z bosons are generated by three of the four degrees of freedom of ϕ. The fourth degree of freedom is for the Higgs boson. In the Lagrangian of the Standard Model, the couplings of the Higgs boson to fermions is proportional to the mass of that fermion.

1.1.1 Shortcomings of the Standard Model

The Standard Model is a low-energy effective theory that is in good agreement with numerous experimental results. However, there are several limitations of the Standard Model. Firstly, it does not include gravity. In addition, the Standard Model does not provide a candidate for the observed dark matter in the universe. Estimations of the matter and energy distribution of the universe show that ordinary matter accounts for a small percentage of the energy content of the universe [11]. The Standard Model cannot be an inclusive theory of particle physics if it can only explain the matter that makes up only a small fraction of energy content of the universe.

The Standard Model also does not explain why there is more matter than antimatter in the universe. It does not provide large enough CP-violation to explain matter-antimatter asymmetry. Another problem is that a satisfactory fundamental theory should not have so many free parameters. The Lagrangian of the Standard Model depends on over 18 free parameters, whose values must be measured by experiment. These parameters include the Weinberg angle, the gauge coupling, the masses of the quarks and leptons, the CKM matrix elements, the QCD vacuum angle, the vacuum expectation value of the Higgs field, and the Higgs mass.

An aesthetic problem of the Standard Model is that it is not a Grand Unified Theory (GUT). The coupling constants of the interactions described by the Standard Model do not coincide when extrapolated to higher energies. Another aesthetic limitation of the Standard Model are hierarchy problems. For example, there is a large discrepancy between the weak scale and the that of gravity. There are numerous theories that address one or more of the limitations of the Standard Model. These include models with extended gauge sector and Supersymmetry (SUSY). Attractive aspects of SUSY are that it provides a natural candidate for dark matter and that the fundamental forces can be unified when their coupling constants are extrapolated to the TeV scale.

1.2 Properties of the Tau Lepton

Tau leptons play an important role in the physics programs of the LHC. They are especially relevant in probing the nature of electroweak symmetry breaking since the Higgs boson couples proportionally to mass and tau leptons are the heaviest of the known fermions. The branching ratio of the Higgs boson to decay into a pair of tau leptons is significant around a mass near that of the 125 GeV resonance discovered at the LHC [1, 2]. In addition, many SUSY signatures contain tau leptons in the final state. In the Higgs sector of the Minimal Supersymmetry Model (MSSM), for example, there are enhanced couplings to tau leptons over large regions of parameter space. Couplings of the MSSM Higgs to vector bosons are suppressed, so searches involving taus are especially pertinent.

It was first detected in a series of experiments from 1974 to 1977 by Martin Lewis Perl and his research group at the LBL detector at SLAC [12]. M. L. Perl was awarded half of the 1995 Nobel Prize in Physics for the discovery of the tau lepton [13]. The tau lepton is the heaviest known lepton to date. Its mean lifetime is $(290.6 \pm 1.0) \times 10^{-15}$ seconds [4]. The mean free path length of the tau is 87 μm. Thus, taus decay before they can be detected by the ATLAS detector, and their signature must be extracted from their decay products.

The tau lepton is the only known lepton that decays both leptonically and hadronically. Table 1.3 shows the branching fractions of the most prominent tau decay modes. Taus decay hadronically 64.7%

of the time and typically into a low multiplicity of particles. Decays with dominant branching ratios are tau leptons decaying into one or three charged hadrons, a tau neutrino, and ≥ 0 neutral hadrons. The charged products of taus are usually charged pions, $\pi^{\pm}$, and, for a small percent of the time, charged kaons, $K^{\pm}$. Strangeness production is Cabibbo suppressed, so decays into charged kaons are rare. Taus with only one associated charged product (one-prong decays) occur 49.5% of the time, as shown in Table 1.3. Tau decaying into three associated charged products, or three-prong decays, occur 15.2% of the time. The neutral products of taus are usually neutral pions. With a mean lifetime of $(8.52 \pm 0.18) \times 10^{-17}$ seconds [4], the neutral pions decay before showering in the presampler or the ECAL. They decay via the electromagnetic interaction and predominately into two photons ((98.823 ± 0.034)% of the time). Dalitz decays of the π^0 into $e^+e^-\gamma$ are helicity suppressed and thus happen with a branching fraction of (1.174 ± 0.035)%. Thus, the final decay products of the tau seen in the detector are usually one or three charged pions and zero, two or four photons from the π^0.

		τ Decay Mode	Branching Fraction (%)
Leptonic		$\tau^{\pm} \to e^{\pm} + \overline{\nu}_e + \nu_\tau$	17.84 ± 0.04
		$\tau^{\pm} \to \mu^{\pm} + \overline{\nu}_\mu + \nu_\tau$	17.41 ± 0.04
Hadronic	One-prong	$\tau^{\pm} \to \pi^{\pm} + (\geq 0\, \pi^0) + \nu_\tau$	49.46 ± 0.10
		$\tau^{\pm} \to \pi^{\pm} + \nu_\tau$	10.83 ± 0.06
		$\tau^{\pm} \to \rho^{\pm}(\to \pi^{\pm} + \pi^0) + \nu_\tau$	25.52 ± 0.09
		$\tau^{\pm} \to a_1(\to \pi^{\pm} + 2\pi^0) + \nu_\tau$	9.30 ± 0.11
		$\tau^{\pm} \to \pi^{\pm} + 3\pi^0 + \nu_\tau$	1.05 ± 0.07
		$\tau^{\pm} \to h^{\pm} + 4\pi^0 + \nu_\tau$	0.11 ± 0.04
Hadronic	Three-prong	$\tau^{\pm} \to \pi^{\pm} + \pi^{\mp} + \pi^{\pm} + (\geq 0\pi^0) + \nu_\tau$	14.57 ± 0.07
		$\tau^{\pm} \to \pi^{\pm} + \pi^{\mp} + \pi^{\pm} + \nu_\tau$	8.99 ± 0.06
		$\tau^{\pm} \to \pi^{\pm} + \pi^{\mp} + \pi^{\pm} + \pi^0 + \nu_\tau$	2.70 ± 0.08

Tab. 1.3: Decay modes and branching fractions of the τ lepton. The $h^{\pm}$ symbol denotes a $\pi^{\pm}$ or a $K^{\pm}$. Branching fractions for K^0, ω, and/or η are not included.

1.3 Polarization Studies with Tau Leptons

This section introduces the concept of polarization and explains the motivations for polarization studies with tau leptons. Then, it discusses the sensitivity to polarization measurements using tau leptons as final state particles, giving reasons for using the the ρ decay mode of the tau.

Tau leptons decay via the weak interaction (see Figure 1.2). The theory for the weak interaction has a V-A (vector minus axial vector) form. In this theory, the weak interaction couples to left-handed fermions and right-handed antifermions. The helicity of a tau lepton is the spin of the particle projected onto its direction of motion and is given as

$$\lambda = \frac{1}{2}\frac{\sigma \cdot \mathbf{p}}{|\mathbf{p}|}. \tag{1.6}$$

From this equation, the flight direction of left-handed fermions, with an eigenvalue of $-\frac{1}{2}$, is opposite to the direction of its spin while the flight direction of right-handed fermions, with an eigenvalue of $+\frac{1}{2}$, is in the same direction as its spin. Although helicity is a good quantum number, it depends on a particle's

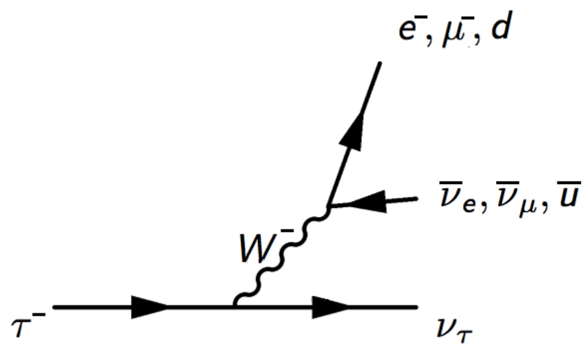

Fig. 1.2: Example Feynman diagram of the τ^- decaying via the weak interaction.

direction of motion, so it is not a Lorentz-invariant property for massive particles. For example, if a lower-velocity particle were to accelerate past a second massive particle, the second particle would appear to have had its helicity flipped. Helicity applies for massless particles. At the relativistic limit, where $m \ll E$, helicity states coincide with the states of chirality.

The polarization states of the tau lepton are experimentally accessible by studying the kinematics of its decay products because the angular distributions of tau decay products are affected by the polarization of the tau [14]. The following section provides applications of tau polarization measurements in physics analyses at the LHC. In order to explain the last two motivations presented, this section first provides a discussion of polarization measurements of individual taus for the simplest case, $\tau \to \pi\nu_\tau$, and then for the $\tau \to \rho\nu_\tau$. The decay of a tau via the ρ resonance (a ρ decay) is the most sensitive decay channel for tau polarization measurements in a hadron-hadron collider [15]. Afterward, a discussion of how tau polarization measurements are used to discriminate between $Z \to \tau^\pm\tau^\mp$ and $H \to \tau^\pm\tau^\mp$ decays is given. Finally, the section concludes with a motivation for using the ρ decay of the tau for polarization measurements and emphasizes the importance of correctly classifying ρ decays from the tau, which is improved by the algorithm presented in this thesis.

Tau polarization can be used to measure the spin of new $\tau^\pm\tau^\mp$ resonances. Moreover, tau polarization measurements contain information on SUSY couplings. The average tau polarization in the $\widetilde{\chi}^0_2 \to \widetilde{\tau}_1\tau \to \tau\tau\widetilde{\chi}^0_1$ decay depends on the couplings between τ, $\widetilde{\tau}_1$, and $\widetilde{\chi}^0_j$, where a tilde denotes a superpartner in SUSY [16]. Another application of tau polarization measurements is the discrimination against SM background processes in searches for new resonances. The irreducible background from $Z \to \tau\tau$ decays in $H \to \tau\tau$ searches can be suppressed, since the SM Higgs boson is a spin-0 particle and the Z boson is a spin-1 particle. In addition, polarization measurements can be used to discriminate against background processes in searches for charged MSSM Higgs bosons because the main SM backgrounds have an opposite polarization from, for example, $H^- \to \tau^-_R\overline{\nu}_R$ decays.

In the $\tau \to \pi\nu_\tau$ decay, the decay kinematics are dictated by conservation of angular momentum and the fixed chirality of the ν_τ. Figure 1.3 provides diagrams of the following discussion of the decay kinematics. The neutrino takes the spin of the tau since the pion is a pseudoscalar, spin-less meson. In the SM, the weak interaction couples to left-hand neutrinos and to right-handed antineutrinos, so the neutrino is emitted in again the spin direction of the tau in $\tau^- \to \pi^-\nu_\tau$ (and in the same direction of the spin of the tau in $\tau^+ \to \pi^+\overline{\nu}_\tau$). Due to conservation of momentum, the pion must then be emitted opposite to the direction of the neutrino. Transforming to the lab frame, experimental data would show that a tau with negative helicity will have a pion boosted in the flight direction of the tau. Inversely, a high-energy pion in the lab frame indicates a tau with positive helicity. The angular distribution of the pion is given as [16]

$$\frac{1}{\Gamma_\tau}\frac{\Gamma_\pi}{\mathrm{d}\cos\theta^*} = \frac{1}{2}\mathrm{BR}(\tau \to \pi\nu_\tau)(1 + P_\tau \cos\theta^*) \tag{1.7}$$

where θ^* is the angle between the vector meson and the direction of the tau's momentum, and P_τ is the polarization of the τ,

$$P_\tau = \frac{\sigma_\mathrm{R} - \sigma_\mathrm{L}}{\sigma_\mathrm{R} + \sigma_\mathrm{L}}. \tag{1.8}$$

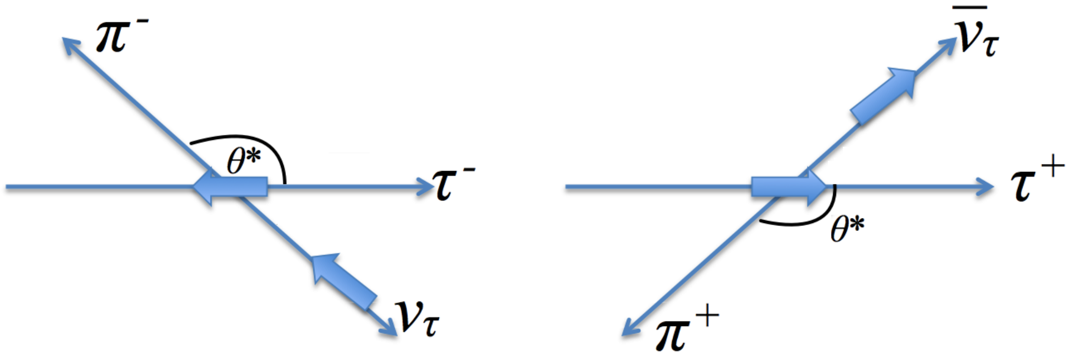

Fig. 1.3: The decay $\tau \to \pi\nu_\tau$ in the rest frame of the τ (the thin horizontal arrow shows the flight direction of the tau in the lab frame) showing the preferred decay kinematics of the π and ν_τ decay products for a left handed τ^- (left) and a right-handed τ^+. The other thin arrows show the directions of flight of the particles in the rest frame of the tau, and the thick arrows show the handedness of the particles.

For the case of a tau decaying into a hadron that also carries spin, the situation is more complicated. For a tau decaying through the ρ resonance, the $\rho^\pm$ meson can be either longitudinally polarized (aligned with the spin of the tau) or transversely polarized, from the conservation of angular momentum. The same spin possibilities exist for $\tau \to a_1\nu_\tau$ decays. Figure 1.4 shows the kinematics of the $\tau^- \to \rho^-\overline{\nu}_\tau$ decay in the rest frame of the tau, which contain information on whether the ρ was longitudinally or transversely polarized. The angular distribution of the products of a ρ^- decay depends on the polarization of the τ and is described by the following equations [14]:

$$\begin{aligned}\frac{1}{\Gamma_\tau}\frac{\Gamma_T}{\mathrm{d}\cos\theta^*} &\propto \frac{1}{2}\mathrm{BR}(\tau \to \rho\nu_\tau)(1 - P_\tau \cos\theta^*)\\ \frac{1}{\Gamma_\tau}\frac{\Gamma_L}{\mathrm{d}\cos\theta^*} &\propto \frac{1}{2}\mathrm{BR}(\tau \to \rho\nu_\tau)(1 + P_\tau \cos\theta^*),\end{aligned} \tag{1.9}$$

where T denotes the transverse vector meson state and L denotes the longitudinal vector meson state. The spin of the $\rho^\pm$ is transformed into orbital angular momentum in its decay into a $\pi^\pm$ and a π^0. When the spin of the ρ^- is perpendicular to that of a left-handed τ^-, the ρ^- is preferably emitted against the flight direction of the τ^-. Similarly, when the spin of the ρ^- is parallel to the spin direction of a left-handed τ^-, the ρ^- is preferably emitted in the flight direction of the τ^-. These two cases can be distinguished by measuring the momenta of the $\pi^\pm$ and the π^0. If the two pions have similar momenta, then the ρ^- was transversely polarized. If the two pions have opposite momenta (one high-energy, one low-energy), then the ρ^- was longitudinally polarized. The angular distributions between the $\pi^\pm$ and the ρ, in the rest frame of the ρ, separates these two polarization states [14].

For the application of tau polarization measurements to distinguish between $Z \to \tau^\pm\tau^\mp$ decays and $H \to \tau^\pm\tau^\mp$ decays, an explanation is given for the simplest case where both taus decay to a charged pion

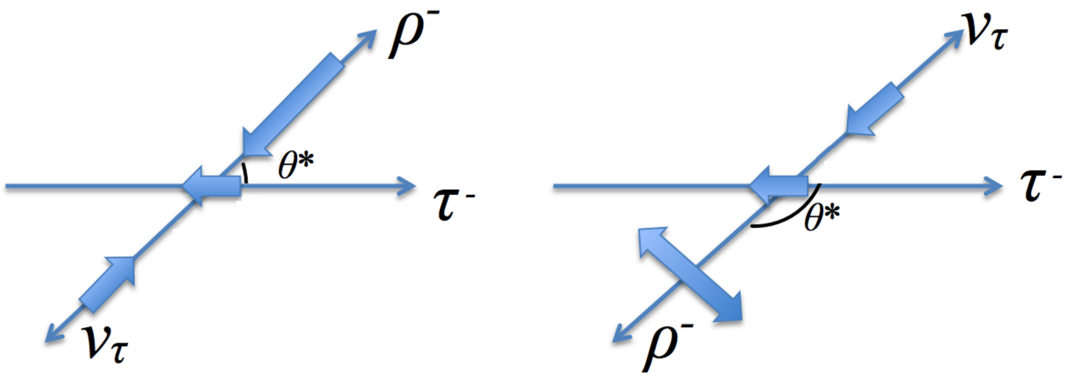

Fig. 1.4: The $\tau^- \to \rho^- \bar{\nu}_\tau$ decay in the rest frame of the ρ for a transversely polarized longitudinally polarized ρ (left) and a transversely polarized ρ (right). The thin horizontal arrow shows the flight direction of the tau in the lab frame, the other thin arrows show the direction of flight of the particle in the τ rest frame, and the thick arrows show the handedness of the particle.

and a tau neutrino. Figure 1.5 shows the decay of the Z boson to taus in the rest frame of the Z boson and how the polarization of the Z boson affects the flight direction of the decay products. Figure 1.6 shows a similar schematic, but for the decay of the Higgs boson to taus in the rest frame of the H boson. Only one of the charged pions from the $\tau^+\tau^-$ pair from H will have high energy, since it preferentially experiences a boost from being emitted in the flight direction of H, while the other will have low-energy, since it is preferentially emitted opposite to the flight direction of H. On the other hand, for a $Z \to \tau\tau$ decay, the two charged pions from the $\tau^+\tau^-$ pair will both be preferentially high energy (or low energy), since both taus are emitted in the direction (or opposite to the direction) of the flight path of Z.

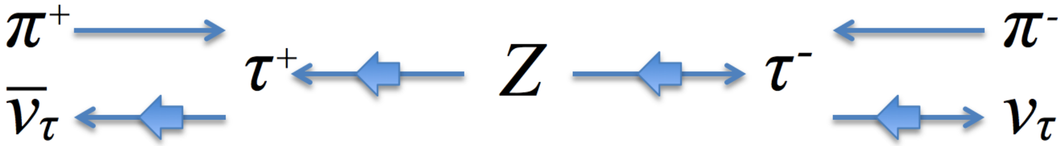

Fig. 1.5: The decay $Z \to \tau^+\tau^- \to \pi^+\nu_\tau\pi^-\bar{\nu}_\tau$ in the rest frame of the Z boson. The thin arrows show the direction of flight of the particle, and the thick arrows show the handedness of the particle.

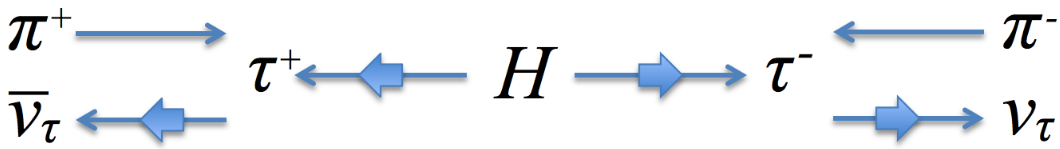

Fig. 1.6: The decay $H \to \tau^+\tau^- \to \pi^+\nu_\tau\pi^-\bar{\nu}_\tau$ in the rest frame of the H boson. The thin arrows show the direction of flight of the particle, and the thick arrows show the handedness of the particle.

The ρ decay channel of the tau is more sensitive to polarization measurements than the $\tau \to \pi\nu_\tau$ decay at hadron hadron colliders, such as the LHC [15]. Tau polarization measurements can be performed using the visible decay products from the ρ decay, while the $\tau \to \pi\nu_\tau$ decay relies also on the reconstruction of the four-momentum of the neutrino. At the LHC, only the missing energy in the plane perpendicular to the beam axis can be measured. The kinematics of the subsequent decay of the ρ

provide discriminatory angular distributions between the two polarization states that are not applicable for the $\tau \to \pi\nu_\tau$. Moreover, the ρ decay channel is more sensitive than the a_1 decay channel because polarization sensitivity depends on the boost of the vector meson emitted from the tau in the tau rest frame. The $\tau \to \rho\nu_\tau$ decay experiences a larger boost than does the $\tau \to a_1\nu_\tau$ decay, due to the larger mass difference between the ρ and the τ. The angular distribution of the a_1 decay is almost independent of the tau polarization. Also, the $\tau \to \rho\nu_\tau$ decay occurs 2.5 times more frequently than the $\tau \to a_1\nu_\tau$ decay, as shown in Table 1.3, thus increasing the sensitivity of the ρ decay to tau polarization measurements.

In conclusion, the sensitivity of polarization measurements can be significantly improved by studying ρ decays from the τ. Distinguishing between the ρ and a_1 decay modes improves the precision tau polarization measurements because including wrongly classified a_1 decays in the reconstruction of ρ decays will measurements of variables that are sensitive to tau polarization. Therefore, improving the purity of the $\rho^\pm$ decays classified by reconstruction algorithms of hadronically decaying taus and improving the four-momentum resolution of the pions from a $\rho^\pm$ decays are of vital importance. Decay modes of the tau can be determined by counting the number of charged and neutral particles, and, as a side effect, the four-momentum resolution can be improved by identifying the correct π^0 energy deposits in a particle detector. As will be shown as a result of this thesis, $\rho^\pm$ decays from the tau can be better identified by counting the number of photons from a neutral pion.

Chapter 2

The ATLAS Experiment at the Large Hadron Collider

An overview of the Large Hadron Collider and ATLAS detector are given in the first two parts of this section, followed by a description of the coordinate system at ATLAS. Then, the next sections provide a more detailed description of the tracking system and calorimeters, which are the most important detector components for tau reconstruction.

2.1 Overview of the LHC

The LHC is a particle accelerator at the European Organization for Nuclear Research (CERN) in Geneva, Switzerland, built 45-180 m underground in the tunnel of the erstwhile LEP (Large Electron-Positron Collider) accelerator. It collides counter-propagating beams of protons or heavy ions, grouped together in bunches. There are about 1.15×10^{11} protons per bunch and about 2808 bunches per beam at the LHC. When a bunch of protons collides with another bunch of protons, the most important process is the hard scattering process in which partons from the proton collide to create a system of large mass or large momentum transfer.

The proton bunches are brought to collide at a total of eight interaction points. Four of the interaction points are for the major experiments at the LHC, and the four other interaction points are used for acceleration, beam cleaning, etc. The major experiments at the LHC, as shown in Figure 2.1, are

- ALICE, A Large Ion Collider Experiment, point 2
  Studies quark-gluon plasmas with heavy ion collisions, using collisions of lead ions and protons.

- ATLAS, A Toroidal LHC ApparatuS, point 1
  General purpose detector, described in Section 2.2.

- CMS, Compact Muon Solenoid, point 5
  General purpose detector with same aims as ATLAS. ATLAS and CMS cross-check each other's results.

- LHCb, Large Hadron Collider beauty experiment, point 8
  Studies heavy flavor physics. Makes precision measurements of CP violation and rare B-meson decays.

The first collisions at the LHC began on November 2, 2009 [18]. Since then, data have been taken at center-of-mass energies, $\sqrt{s}$, of 2.76 TeV for one month in 2010, 7 TeV in 2011, and 8 TeV in 2012, with recorded integrated luminosities up to 9.2 μb^{-1}, 5.25 fb^{-1} and 21.7 fb^{-1}, respectively. Here, 1 fb =

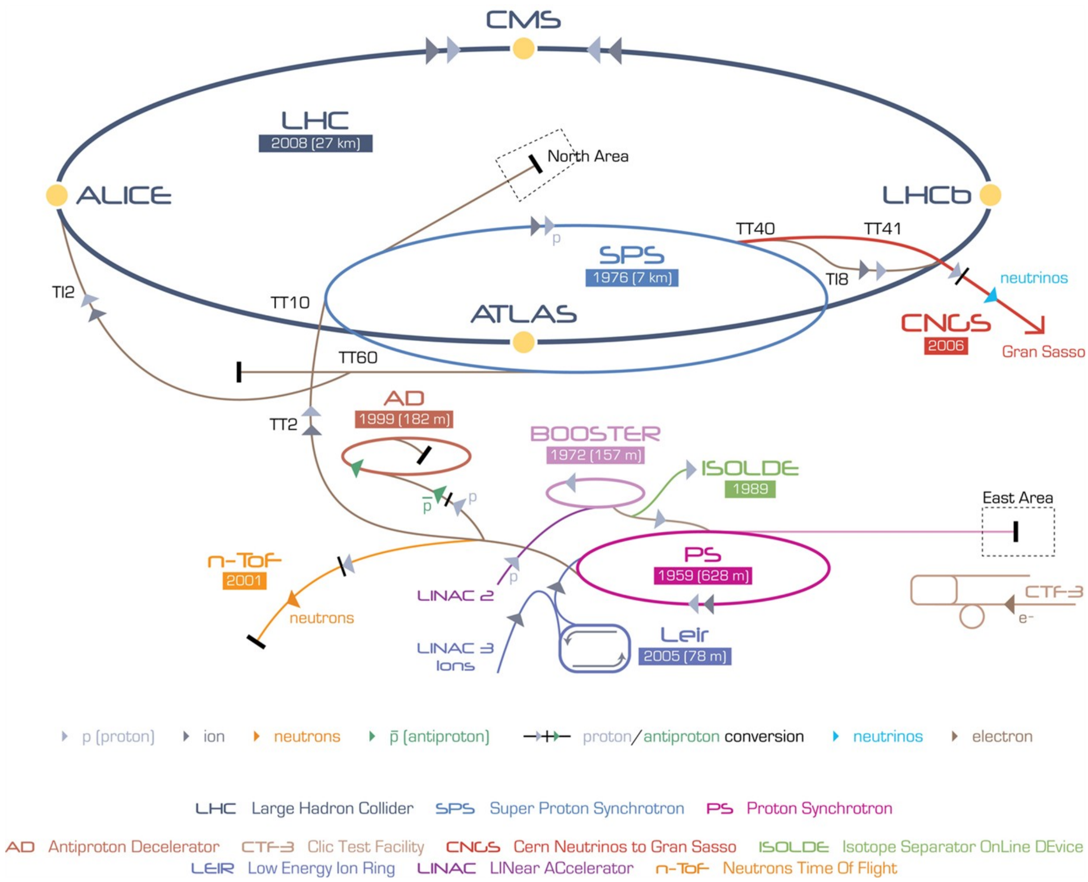

Fig. 2.1: Schematic of the LHC accelerator complex, showing the four major experiments and the accelerator injection chain [17].

10^{-39} cm^2, and, in this context, luminosity, $\mathcal{L}$, describes the number of collisions produced per area per second. The total number of recorded events for a given process, N_{process}, is then given by

$$N_{\text{process}} = \sigma_{\text{process}} \int \mathcal{L}\, \mathrm{d}t, \tag{2.1}$$

where σ_{process} is the cross section for that given process. Before the first long shutdown (LS1) in February 2013, the LHC has been able to operate with 1380 bunches per beam and an average of 31.87 interactions per bunch crossing. The LHC is currently in the first long shutdown phase, which will last about 20 months. LS1 is dedicated to the transition of the LHC to the design energy of $\sqrt{s}$ = 13-14 TeV, nominal instantaneous luminosity of $\mathcal{L} = 1 \times 10^{34}$ cm^{-2} s^{-1}, and a shortened bunch spacing of 25 ns between each bunch by 2017.

The proton beams of the LHC are derived from hydrogen atoms that have been stripped of their valence electrons and inserted into a chain of accelerators before the final injection into the LHC. In the last stages of the chain, the Super Proton Synchrotron (SPS) accelerates the protons to 450 GeV before injecting two beams of protons into the LHC, traveling clockwise and counter-clockwise, each in their own beam pipe, except for the interaction regions where the beams share the same pipe for approximately 130 mm [19]. The protons are then accelerated in the LHC by two independent radio frequency (RF) systems, one per beam, each with eight superconducting cavities. Both beam pipes are located in the same magnet system, made up of 1232 superconducting dipole magnets to guide the beams in the ring and 386 quadruple magnets to focus the beams. The magnetic field is designed to reach up to the 8.4 T required to deflect charged particles produced at the design energy of each 7 TeV beam (which means a center-of-mass energy of $\sqrt{s} = 14$ TeV). To reach such strong magnetic fields, the magnets are superconductors and cooled to a temperature of 1.7 K using liquid helium.

2.2 Overview of the ATLAS Detector

The ATLAS detector weighs 7000 tons, is 25 m high, and is 44 m long. The detector was designed with the following goals in mind:

- Determine if the SM Higgs boson is realized in nature.
- Search for new physics beyond the Standard Model that should reveal signatures at the TeV scale.
- Conduct precision SM measurements, e.g., Quantum Chromo-Dynamics (QCD), electro-weak processes, flavor physics, and top-quark physics.

The ATLAS detector was optimized toward the benchmark performance required from the important subdetectors in the search for the Higgs boson and new physics. Therefore, ATLAS is designed to reconstruct, with decent precision, over a wide range of known and hypothesized processes producing such final state particles as photons, electrons, muons, taus, jets,[1] and missing transverse energy from minimally interacting or non-interacting particles. Since the final transverse momentum of all scattered particles, i, must be zero, due to momentum conservation, i.e.,

$$\sum_i p_T^i = 0, \tag{2.2}$$

the missing transverse momentum is given by

$$p_T^{\text{miss}} = -\sum_i p_T^i. \tag{2.3}$$

Figure 2.2 shows a schematic of the components of the detector. From the beam pipe on outward the components are

- The **inner detector**, which records the signatures of charged particles. It is enclosed in a 2 T magnetic field to bend the trajectory of charged particles, from which their transverse momenta are determined. Tracks are matched together to reconstruct the original vertex (and secondary vertex for some long-lived processes) from which an event originated.
- The **electromagnetic calorimeter** (ECAL), which is a sampling calorimeter that instigates electromagnetic showers from photons and electrons and records their energy deposits. Hadrons sometimes start to shower in the ECAL.
- The **hadron calorimeter** (HCAL), which is a sampling calorimeter that measures jets and hadronically decaying taus by initiating showers from nuclear interactions. The HCAL extends enough interaction lengths to contain hadrons and stop them from reaching the muon chambers.

[1] Color-charged particles bind together to form new color-neutral particles. This hadronization, or fragmentation, process results in jets of hadrons seen in the detector.

- The **muon system**, which detects muon. Muon traverse all inner parts of the detector and continue on outward from the detector. The tracks in the muon system are matched to those in the inner detector, and this also helps to veto background from cosmic ray muons, which would not come from an interaction point in the inner detector. The muons in the range center part of the detector are deflected by a large barrel toroidal magnet that gives ATLAS its name, and muon tracks in the two outer ends of the detector are bent by two smaller endcap magnets at the ends of the barrel toroid.
- The **trigger** system is used to select which interesting events should be written to disk, thus reducing the expected data rate. The online trigger has three levels: L1, L2, and the event filter. L1 makes a decision about an event in less than 25 μs using information from a subset of detectors and reduces the data rate to ~75 kHz. L2 is seeded from the region of interest seeded from by L1 and reduces the rate to ~3.5 kHz within a total event processing time of ~40 ms. Finally, the event filter reduces the final rate to ~200 kHz, with an event size of ~1.3 megabytes. Offline trigger is then applied, with an average processing time on the order of 4 s per event.

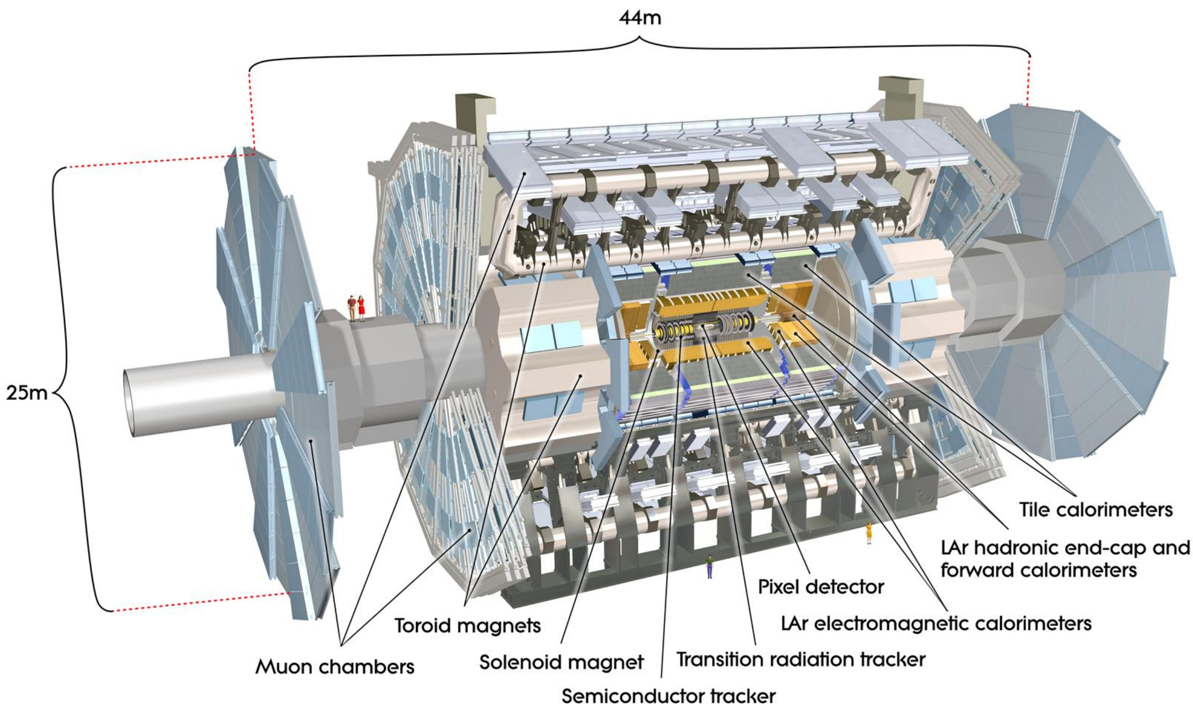

Fig. 2.2: Onion layer schematic of the ATLAS detector showing the principal sub detectors [19].

2.2.1 The Coordinate System

ATLAS is a barrel-shaped detector designed to provide as much coverage as possible to record many different types of final state objects. A right-handed coordinate system is used, and the origin is at the center of the ATLAS detector, or the nominal interaction point.

The z-axis is oriented in the longitudinal direction, parallel to the beam, in the anti-clockwise direction. The x-axis points toward the center of the LHC ring, and the y-axis points up, perpendicular to the plane formed by the x- and z- axes. The azimuthal angle, ϕ, traverses around the beam axis in the xy-plane, with a range of $[-\pi, \pi]$. The polar angle, θ, is the angle with respect to the z-axis. Pseudorapidity, η, defined as a function of the polar angle, θ:

$$\eta = -\ln\left(\tan\left(\frac{\theta}{2}\right)\right). \tag{2.4}$$

The advantages of using η are that particle production is roughly constant vs. η for relativistic particles and differences in η are invariant under boosts along the z axis. Transverse quantities are defined in this xy-plane, e.g., traverse energy ($E_T = E\sin\theta$), transverse momentum ($p_T = |\mathbf{p}|\sin\theta$), missing transverse momentum (p_T^{miss}), which arises from particles like neutrinos that do not interact, or interact minimally with the detector. To describe distances between objects in the ATLAS detector, a cone is defined in the pseudorapidity-azimuthal angle space, given as

$$\Delta R = \sqrt{\Delta\eta^2 + \Delta\phi^2}. \tag{2.5}$$

2.3 The Inner Detector

The inner detector is used to reconstruct the tracks of charged particles. It takes multiple measurements as particles move outward from the beam pipe, at several radii. The physics quantities measured by the inner detector are the charges and lifetimes of particles originating from the interaction point of the colliding proton bunches. The momenta are measured using a charged particle's trajectory that is bent by a 2 T magnetic field. This magnetic field comes from a solenoidal magnetic field generated by a superconducting magnet located inside a cryostat. The inner detector measures the lifetimes of particles by matching tracks to reconstruct their points of origin. The distance between a primary and a subsequent secondary vertex provides information on a particle's mean lifetime, τ. This is relevant for reconstruction of particles that decay before entering the inner detector, such as tau leptons (explained previously in Section 1 and in more detail later in Section 3) and b-quarks. In relation to this thesis, the tracking system can also be used to find photon conversions ($\gamma \to e^{\pm}e^{\mp}$).

In total, the inner detector is a cylinder that is about 7 m long, with a radius of about 1 m. Given that about 1000 particles are created from each bunch crossing every 25 ns within the pseudorapidity range $|\eta| < 2.5$, the inner detector must perform well in a harsh environment of high track density and reconstruct each vertex correctly. During the first collisions at the LHC, the inner detector consisted of three subsystems: the pixel detector, the semiconductor tracker (SCT), and the transition radiation tracker (TRT).

For $0.25 < |\eta| < 0.5$, the inverse transverse momentum resolution obtained with the inner detector for muons is

$$\sigma_{1/p_T} = 0.34\ \mathrm{TeV}^{-1}\left(1 \oplus \frac{44\ \mathrm{GeV}}{p_T}\right), \tag{2.6}$$

where p_T is in GeV and the $\oplus$ symbol means that the terms are added in quadrature and then the square root is taken. The decrease in resolution of the inner detector at higher p_T comes from the fact that higher p_T charged particles experience less of a deflection by the magnetic field. The resolution at low p_T is dominated by multiple scattering. Figure 2.3 shows the energy resolution of single charged pions in the inner detector and also in the calorimeter. After the first long shutdown at the LHC, the inner detector will feature a new addition: an innermost pixel layer, or the insertable B-Layer [21]. The B-layer will bring the proximity of the detector closer to the beam pipe, moving the closest point of the detector to the interaction point from 5.05 cm to 3.27 cm.

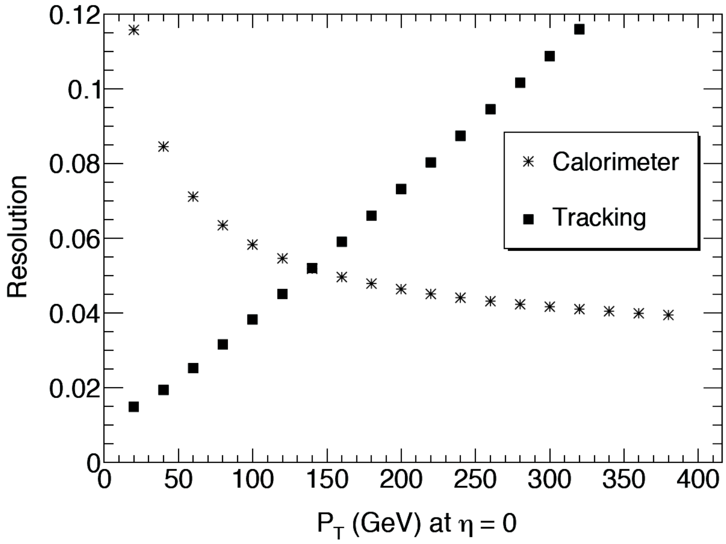

Fig. 2.3: Energy/Transverse momentum resolution of single charged pions in the ATLAS calorimeter and tracking systems at $\eta = 0$ [20].

2.4 The Calorimeter System

ATLAS uses sampling calorimeters to record energy depositions from particles. The calorimeter system at ATLAS measures neutral particles, which are not recorded by tracking system. A sampling material initiates showers from primary particles entering or passing through the calorimeter, thus creating a cascade of secondary particles. Energy from these particles is converted to energy depositions in the calorimeter. In the LAr calorimeter, this conversion occurs mostly via ionization and results a detector response. The LAr acts as an ionization chamber, where electron-ion pairs are created when ionizing particles pass through the LAr active layer. These electrons and ions drift, accelerated by the applied electric field in the LAr barrel, toward the electrodes of the readout board. The electrons have a much shorter drift time than the ions, so the contribution to the ionization signal from ions is negligible. Nevertheless, the drift time of the electrons (on the order of hundreds of ns) is much longer than the time between LHC bunch crossings ($\sim$ 25 ns), so only the beginning of the ionization signal is used in the signal readout.

The transverse profile of an electromagnetic shower in the calorimeter is characterized by the Moliere radius, R_M, which is a constant for a given calorimeter material. The Moliere radius is the radius within which 90% of the energy in the electromagnetic shower is contained. For liquid argon, $R_M = 10.1$ cm.

$$R_M = \frac{21\text{ MeV}}{E_C} X_0 = 0.0265 X_0 \left(Z + \frac{1}{2} \right). \tag{2.7}$$

In the equation for R_M, the radiation length, X_0, is the mean path length after which the energy of a relativistic charged particle is reduced by a factor of $\frac{1}{e} = 0.368$:

$$X_0 = \frac{180A}{Z^2} \frac{\text{g}}{\text{cm}^2}. \tag{2.8}$$

A schematic of the ATLAS calorimeter system is shown in Figure 2.4. The calorimeters of the

ATLAS detector are segmented in depth for the identification of hadronic vs. electromagnetic showers[2] to reconstruct the starting point of a shower. It can help with vertex matching of neutral particles by reconstructing the shower axis, such as in the $H \to \gamma\gamma$ analysis [22]. The calorimeters' energy resolution improves with increasing energy, while the energy resolution of trackers decreases with increasing p_T , due to a larger bending radius (see Figure 2.3). After the inner detector, the next outer layer is the presampler. The presampler is part of the calorimeter. Its function is to correct for the energy lost by particles moving upstream before entering the calorimeter. Since its function is for energy recovery, the original granularity of the presampler was reduced from the size equivalent to that of an ECAL strip cell to $\Delta\eta \times \Delta\phi = 0.025 \times 0.025$ [19].

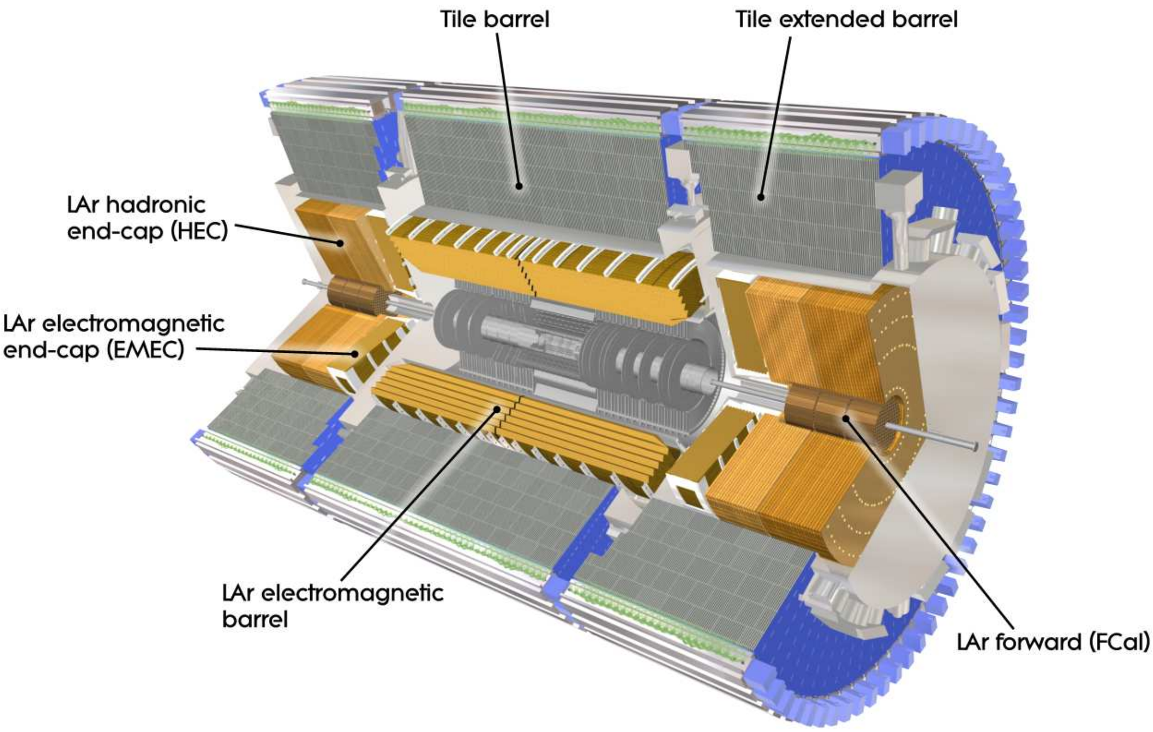

Fig. 2.4: Schematic of the subcomponents of the calorimeter system [19].

2.4.1 The Electromagnetic Calorimeter

The electromagnetic calorimeter of the ATLAS detector is a liquid argon (LAr) sampling calorimeter, with lead-stainless-steel absorbers, that provides excellent energy and spatial resolution. In general, sampling calorimeters have worse energy resolution than homogeneous calorimeters because of sampling fluctuations. However, the advantage of a sampling calorimeter is that they can reach sufficient interaction depths to contain showers, and longitudinal segmentation is staightforward.

The ECAL of the ATLAS detector is shaped like a cylinder, with a barrel part ($|\eta| < 1.3$) and two endcap wheels on each side ($1.5 < |\eta| < 2.5$), as shown in Figure 2.4. The calorimeter is made up of two identical half-barrels, which are separated by a few millimeters at the connection. The "crack" region

[2] Electromagnetic showers develop over shorter lengths than hadronic showers.

in $1.3 < |\eta| < 1.5$ describes the transition from barrel to endcap where precision in energy and spatial resolution are lost. The longitudinal thickness of the ECAL is $\geq 26\ X_0$. These lengths were optimized in order to minimize the degradation of energy resolution from leakage of the electromagnetic showers from particles into the later HCAL layers. Each half-barrel of the ECAL contains 1024 of these lead-stainless-steel converters, with readout boards in between. This dense absorber material means that the calorimeter can be highly compact.

In between these alternating absorbing layers is liquid Argon (LAr), which is used as an active material to measure energy deposits from these secondary particles from the showers. To maintain a liquid state, the calorimeter is enclosed in a cryostat cooled to 89.3 K (one for the barrel, and one for the endcap), which cools the argon and, thus, the LAr flows between the lead plates. The advantage of LAr is that it has stable response over time, intrinsic hardness against radiation, and intrinsic linear behavior. The cells stored in data files are obtained by segmenting and positioning the readout channels. The readout board of the ECAL can be very finely segmented to create a high granularity, or density, of cells, especially in pseudorapidity. Each ECAL cell is defined in η by etchings in the readout board and, for some parts of the ECAL, by grouping together adjacent readout boards in ϕ.

The ECAL is longitudinally segmented into three layers. A module of the ECAL is shown in Figure 2.5. The second layer is the longest and contains the greatest fraction of an electromagnetic shower's energy. The third layer contains tails of electromagnetic showers. The lateral partitioning for each of the three layers is given in Table A.1. The first layer of the ECAL, from here on called ECAL1 or the strip layer, is the most relevant part of the detector for this thesis.

The strip layer is the first sampling layer, or the "front face", of the ECAL and was designed to measure the pointing of photons. The design was based on the criterion for π^0 rejection in the $H \rightarrow \gamma\gamma$ decay channel. The longitudinal depth of these narrow strips was therefore chosen to be $6\ X_0$, which includes the length from dead material and the presampler. The strip layer features extremely fine lateral segmentation, with $\Delta\eta \times \Delta\phi$ cell size of (0.003125×0.098) radians in the barrel region, to reconstruct energy deposits from multiple photons. The cell sizes across other η regions are shown in Table A.1. The granularity becomes coarser toward the endcap.

Performance of the calorimeter

From [19], the energy resolution of the electromagnetic calorimeter after noise subtraction is

$$\frac{\sigma(E)}{E} = \frac{a}{\sqrt{E}} \oplus b, \tag{2.9}$$

where E is in GeV. The parameters of the design energy resolution of the ECAL (barrel and endcap) are $a = 10\%$ and $b = 0.7\%$. From energy resolution studies using electron, muon, and pion beams with energies between 1 GeV and 250 GeV, $a = 10.7\%$, $b = 0.5\%$ [19]. This equation shows that the energy resolution improves as energy increases, as shown in Figure 2.3.

The first term is the stochastic term that comes from fluctuations in shower development. Electromagnetic showers are statistical processes and have an error of $\sqrt{E}$. The most significant cause of shower fluctuations is the variation in depth of the first e^+e^- conversion pair from the photon. The first term also has contributions from sampling fluctuations since the ECAL is a sampling calorimeter. The calorimeter measures the total track length, S, which fluctuates as $\sqrt{S}$, so the measured energy will have an error that scales as $\frac{\sigma}{E} \sim \frac{1}{\sqrt{E}}$ since $E \sim S$. In addition, the resolution scales with the thickness of the sampling layers. The second term is the constant term that comes from calibration errors, loss of energy in dead material, and leakage when the shower is not completely contained.

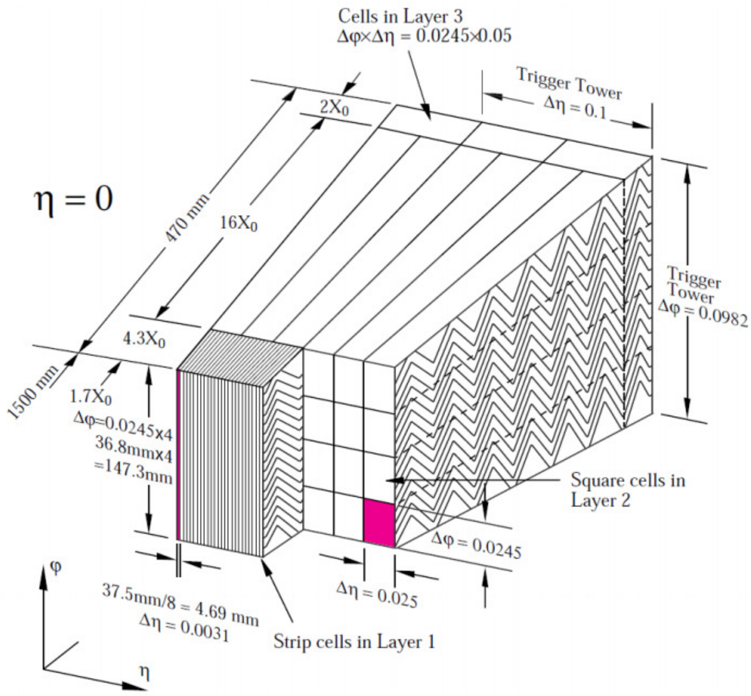

Fig. 2.5: Schematic of a module of the ECAL barrel [19].

2.4.2 The Hadron Calorimeter

The next component moving on outward from the ECAL is the hadron calorimeter, as shown in Figure 2.4. The tile barrel and tile extended barrel components of the HCAL are sampling calorimeters that use steel plates as absorbers and organic scintillating tiles as the active medium. In the tile hadronic calorimeter, the signal formation is different from that described in the previous section for the ECAL because scintillation light from ionizing particles is emitted by the tiles, and this light is then guided by wavelength-shifting fibers toward photo-multiplier tubes. The HCAL endcap is like the sampling endcap of the ECAL, except it uses copper absorbers.

The hadron calorimeter (HCAL) has a design resolution of $a = 50\%\ \sqrt{\mathrm{GeV}}$ and $b = 3.0\%$ for a, b in Equation 2.9. Experimental measurements of the energy resolution in the HCAL endcap using charged pion beams yielded $a = (70.8 \pm 1.5)\%\ \sqrt{\mathrm{GeV}}$ and $b = (5.8 \pm 0.2)\%$. For the tile calorimeter, the energy resolution was measured to be $a = (56.4 \pm 0.4)\%\ \sqrt{\mathrm{GeV}}$ and $b = (5.5 \pm 0.1)\%$ [19].

2.4.3 The Forward Calorimeter

The forward calorimeter is closest to the beam pipe, so it was designed with high particles fluxes and debris from minimum bias events at large η in mind. The forward calorimeter has one EM module, which uses copper as an absorbing material, and two hadron modules, which use tungsten as absorbing material.

2.4.4 Calibration of the Calorimeter System

Calibration is a crucial step for analyses with the ATLAS detector because the energy response is different for different components of the calorimeter. Not all energy is deposited in the sensor material, and different absorber materials, sampling materials, sampling fractions, and readout systems are used. Local Hadron Calibration (LC), described in [23], is the first of two major calibration schemes for the reconstruction of jets and missing energy and is used to calibrate jet energies to the particle level. LC corrects the signal measure by the detector by first classifying energy deposits as hadronic or electromagnetic, to determine which cluster (explained in the next section) needs correction for hadronic activity. Then, it applies weights to the cells of hadronic clusters to determine the correct energy response for hadrons relative to electrons. Finally, LC corrects for leakage and energy lost in inactive material in the detector, and for energy deposited in cells outside of clusters. The second phase of the calibration after LC is the calibration of jet energy on the parton level. The final products after these calibrated jets are physics jets.

2.4.5 Clustering in the Calorimeters

The calorimeter clustering algorithms in ATLAS, described in [24], is used to make sense of the energy deposits in the calorimeters and provides input for particle identification. When particles deposit their energy in the cells of the ATLAS calorimeter, these cells are grouped together into cluster. Then, these three-dimensional clusters are usually associated to particles. The two clustering algorithms in ATLAS are the sliding-window algorithm, used mainly to reconstruct electrons and photons, and the topological clustering algorithm, used mainly to reconstruct jets and missing transverse energy. The clusters used in analyses of this thesis will be clusters from the latter algorithm.

The sliding window algorithm uses a fixed rectangular window, which refer to a block of cells in η-ϕ space, to groups cells together. A precluster is formed if there is a local maximum in the η-ϕ space and the sum p_T in the fixed window is above a certain threshold. The fixed size of the rectangle means that the cluster energy can be very precisely calibrated.

The topological clustering algorithm starts with a seed cell, which is a cell that has an energy significance threshold of $|E| > 4\sigma_{\text{noise}}$. Then, it adds neighboring cells to the cluster if the neighboring cell has $|E| > 2\sigma_{\text{noise}}$. The advantage of topological clustering is noise suppression. The sources of "noise" are readout electronics and pileup that comes from extra interactions in the same beam crossing. Cell-by-cell noise is computed using a calorimeter noise tool [25] and varies with η and also luminosity, as shown in Figure A.3. A feature of topological clustering is the cluster splitter, which searches for local maxima within a cluster to, then, separate the cluster into more than one component, weighting the energy accordingly for each cluster so that cells can share energy between two clusters.

Chapter 3

Tau Leptons in the ATLAS Detector

The topic of this thesis is the reconstruction of hadronically decaying taus in the ATLAS detector. The following section describes the tau reconstruction algorithm at ATLAS. This section also explains an algorithm for the reconstruction of the substructure of hadronically decaying taus, which reconstructs the energy deposits from each individual particle from a tau. From here on and unless otherwise noted, tau reconstruction will refer only to the reconstruction of taus that decay hadronically, and tau decays will refer to taus that decay hadronically. A schematic of a hadronically decaying tau in the ATLAS detector is shown in Figure 3.1.

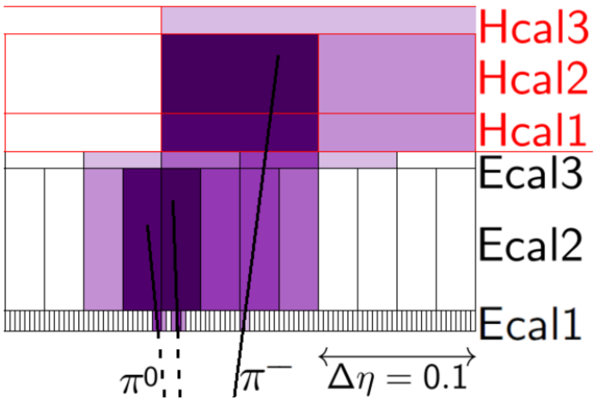

Fig. 3.1: Schematic of the visible decay products of a $\tau^\pm \to \rho^\pm(\to \pi^\pm\pi^0)\nu_\tau$ decay in the ATLAS detector [26].

3.1 Tau Reconstruction in ATLAS

The tau reconstruction algorithm in ATLAS must reconstruct and identify tau decays efficiently while achieving a good jet rejection. The crux of the reconstruction of hadronically decaying taus lies in the fact that jets at ATLAS can fake a hadronically decaying tau. Jets at ATLAS mostly come from multijet production of QCD processes, which have a cross section many orders of magnitude higher than that of weak interactions involving taus. The key distinguishing features between multijet production and hadronically decaying taus are that decay products from taus are more collimated since they experience a boost from the tau and tau decays have a low multiplicity of particles. Figure 3.2 shows a schematic of an a_1 decay in the isolation cone currently used for tau reconstruction in ATLAS.

Another goal of tau reconstruction in ATLAS is a good 4-momentum resolution of the visible tau decay products. This is important, for example, for achieving a good Higgs mass resolution from $H \to \tau\tau$. Tau polarization is also a key property that should be cleanly measured by the tau reconstruction algorithm. Polarization measurements can be used to discriminate $H \to \tau\tau$ from $Z \to \tau\tau$ processes in

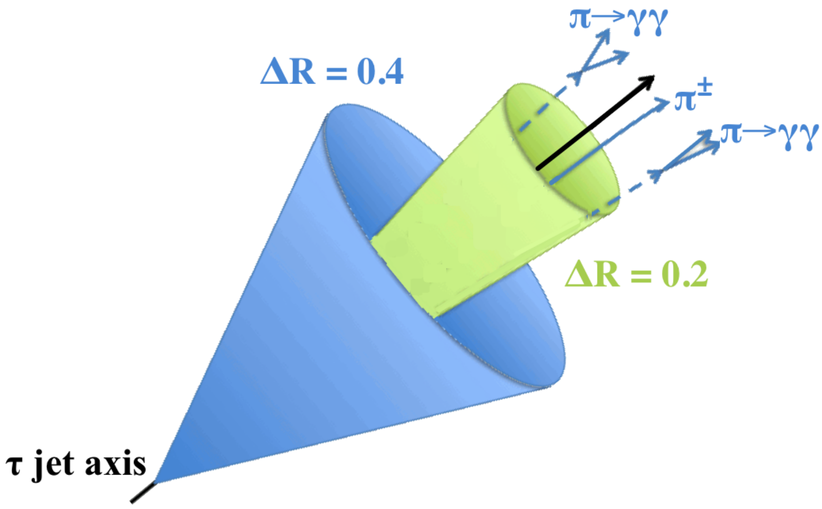

Fig. 3.2: Schematic of the visible decay products of a $\tau^{\pm} \to a_1(\to \pi^{\pm}\pi^{0}\pi^{0})\nu_{\tau}$ decay in the isolation cone currently used at ATLAS. Tau decays are narrow and have a low multiplicity of particles.

Higgs searches, since the Z boson has a different polarization (see Section 1.3). In addition, once the Higgs is found in the di-tau channel, it is pertinent to measure couplings of the Higgs to tau leptons Finally, information from the substructure of the tau decay can be integrated to achieve the main goals listed above, and, in addition, significantly improve decay mode classification. (The benefits of improving the classification of tau decay modes are later explained in Section 4.3.)

A description of the reconstruction algorithm for taus in ATLAS can be found in [27]. This version of the tau reconstruction algorithm was used in the first collision runs of the LHC from 2011-12. It did not use any of the substructure algorithms described later in this section. First, to find tau candidates, the algorithm is seeded by a jet in the calorimeter. These sets of calorimeter jets are reconstructed using the anti-k_t algorithm [28], must pass a p_T threshold of 10 GeV, and must be within the η range of the ATLAS tracking system ($|\eta| < 2.5$). Then, in the anti-k_t algorithm, a list of clusters (see Section 2.4.5 for the description about clusters) in the calorimeter is associated to each seed jet that is considered a tau candidate. After this, tracks that are selected as "good tracks" are associated to these clusters. Good tracks must have a $p_T > 1$ GeV, ≥ 2 pixel hits, and ≥ 7 pixel + silicon tracker hits. Additionally, these good tracks must have a distance of closest approach between the track and the reconstructed primary vertex of $|d_0| < 1.0$ mm in the transverse plane and $z_0 \cdot \sin\theta < 1.5$ mm in the longitudinal direction.

The seeding can pick up many background candidates from multijet background. To discriminate between these candidates and signal tau decays, tau reconstruction relies on the fact that jets from taus have a low multiplicity of charged particles, are narrow, due to the boost from the tau, and have missing energy, from the tau neutrino. In other words, the detector signature is missing transverse energy, an odd number of tracks/prongs, for charge conservation and clusters, all found in a narrow cone. The tau reconstruction algorithm used in ATLAS, described in [29], requires these tracks to be found in a fixed core cone of $\Delta R < 0.2$ around the jet barycenter. Cells found in clusters of calorimeter deposits within a $\Delta R < 0.4$ around the jet barycenter are used for identification variables. Since the last tau reconstruction algorithm at ATLAS [29], a shrinking cone algorithm has been in development where ΔR is parametrized according to the track p_T has been in development.

Hadronically decaying taus are identified using a multivariate discriminator (a Boosted Decision Tree) [30]. Based on the output of this multivariate discriminator, a selection of tau candidates is made for loose, medium, and tight working points, corresponding to identification efficiencies of 60%, 45%, and 30%, respectively. In addition, electron vetoes suppress candidates that can fake a one-prong tau. Bremsstrahlung processes of the electron can even fake three-prong taus because there will be two additional tracks from the daughter electron and photon. An electron veto for three-prong taus was introduced this year, using the same discriminating variables that are used for one-prong taus.

3.2 Tau Substructure Reconstruction

The overall algorithm in ATLAS that will be used for data from the second run of collisions at the LHC starting in 2015 will include the addition of the reconstruction of the substructure of tau decays. The substructure reconstruction algorithm determines the number of neutral pions in a hadronic tau decay, which improves the 4-momentum resolution of the tau reconstructed by the substructure algorithm. That is because this provides the correct neutral and charged components of the decay to work with. Information concerning the charged components can be taken from the tracking system, but the neutral components must be reconstructed from energy deposits in the calorimeter. The three such "energy flow" techniques considered in tau reconstruction, which try to reconstruct individual particles in a jet, are cluster-based [27], cell-based [26], and eflowRec [20]. On top of these algorithms, there is the PanTau algorithm [31], which uses global variables to classify tau decays. This section will discuss the cell-based algorithm because the development of the algorithm presented in this thesis uses input from the cell-based algorithm.

3.2.1 Neutral Pion Reconstruction in the Cell-Based Algorithm

The cell-based algorithm in ATLAS was first developed in 2009 in a diploma thesis by Veit Scharf at the Universität Heidelberg [32] and was extended in a master thesis by Benedict Winter at the Universität Bonn [26]. The ansatz of the algorithm is to first subtract $\pi^{\pm}$ energy deposits from the ECAL using information from the track in the inner detector and energy deposits in the HCAL, which are the detector subcomponents where neutral pions do not leave signatures. Then, the algorithm identifies clusters coming from neutral pions from the remaining energy distribution. This algorithm was first developed on tau decays into one $\pi^{\pm}$, and it has been extended to also reconstruct tau decays into three charged pions in the past year. This section provides a summary of the cell-based algorithm, with focus on features and performance issues related to the the photon identification algorithm developed in this thesis.

Cell-based subtraction of $\pi^{\pm}$

In the first stage, the subtraction of the charged hadron shower found within the tau cone from the presampler, ECAL1, and ECAL2 is done on a cell-by-cell level. The HCAL and the ECAL3 will be grouped together and referred to as the HCAL since it contains mostly hadronic energy. The remainder of the ECAL, which includes the presampler, ECAL1, and ECAL2, is used to reconstruct neutral pions. Since there is a mixture of charged and neutral hadrons in ECAL1/2, the cell-based algorithm uses hadronic shower shapes to estimate the fraction of energy that should be subtracted from each ECAL cell. Only cells found in clusters obtained from the topological clustering algorithm (see Section sec:topoclus) are considered, in order to suppress noise. The hadronic shower shape is estimated from average hadronic shower shapes to minimize inaccuracies in the hadronic subshower removal, since hadronic showers fluctuate a lot. These shapes are modeled with a MC single $\pi^{\pm}$ sample (see Section 4.1.3 for a description of the sample) and are binned according to three categories:

- the track p_T
- the $|\eta|$ position of the track
- the "hadronic fraction," hadF $\equiv \frac{E_{\text{HCAL}}}{p_{\text{track}}}$

First, since we can safely assume that the energy in the HCAL comes from the charged pion but the energy in the ECAL comes from a mixture of charged and neutral pions, the charged hadron's total energy deposit in the ECAL is determined by

$$E^{\pi^\pm}_{\text{ECAL}} = E^{\pi^\pm}_{\text{track}} - E^{\pi^\pm}_{\text{HCAL}}. \tag{3.1}$$

Second, the hadronic energy in each layer of the ECAL is estimated using longitudinal hadronic shower shapes, given by

$$E^{\pi^\pm}_{\text{layer}} = E^{\pi^\pm}_{\text{ECAL}} \left\langle \frac{E^{\pi^\pm}_{\text{layer}}}{E^{\pi^\pm}_{\text{ECAL}}} \right\rangle, \tag{3.2}$$

where $\left\langle \frac{E^{\pi^\pm}_{\text{layer}}}{E^{\pi^\pm}_{\text{ECAL}}} \right\rangle$ is the longitudinal weight calculated for each category mentioned in the list above.

Third, the energy for each layer, estimated by the previous step, is distributed among the cells in that layer by integrating lateral hadronic shower shapes over each cell area. The hadronic energy in each cell of each layer of the ECAL is, therefore, estimated using lateral shower shapes given by

$$E^{\pi^\pm}_{\text{cell}} = E^{\pi^\pm}_{\text{layer}} \int\limits_{\text{cell area}} \left(\sum_{i=1}^{3} a_i \cdot \exp\left(-\sqrt{b_i \Delta\eta^2 + c_i \Delta\phi^2} \right) \right) \mathrm{d}\Delta\eta \, \mathrm{d}\Delta\phi, \tag{3.3}$$

and these shower shapes are categorized according to the same categories for 3-dimensional binning described in the list above. This equation is a parametrization from a fit to a hadronic shower shape allowing the parameters a_i, b_i, and c_i to vary. The precision of the shape parameters relies heavily on the sizes of the cells in the ECAL.

An example of the longitudinal weights from the cell-based algorithm is shown in Figure 3.3a, and an example lateral shower shape is shown in Figure 3.3b. The subtraction is validated using a single charged pion sample, with the reasoning being that the remaining energy in the ECAL should be equal to the energy measured in the ECAL for the single charged pion sample.

Cell-based π^0 reconstruction

In the second stage, the algorithm searches for π^0 candidates in the remaining ECAL energy distribution. The remaining energy is reclustered with the ATLAS topological clustering algorithm [24]. Then, these clusters are either selected or rejected as π^0 clusters. From here on, $\boldsymbol{\pi^0}$ **cluster** refers to clusters after $\pi^\pm$ subtraction by the cell-based algorithm that have passed the π^0 identification. The algorithm must suppress fake π^0 clusters caused by pileup, noise, and imperfect $\pi^\pm$ subtraction due to variations in hadronic shower shapes.

All clusters must pass an energy threshold of 2.5 GeV in order to reduce background. The remaining clusters passing this preselection are identified as either signal π^0 clusters or background clusters by exploiting certain properties. A table of the variables used to exploit the key differentiating properties of signal and background clusters can be found in Table B.1. These variables are used in a BDT [30] to separate the clusters into signal π^0 and background clusters. Some kinematic quantities, such as invariant

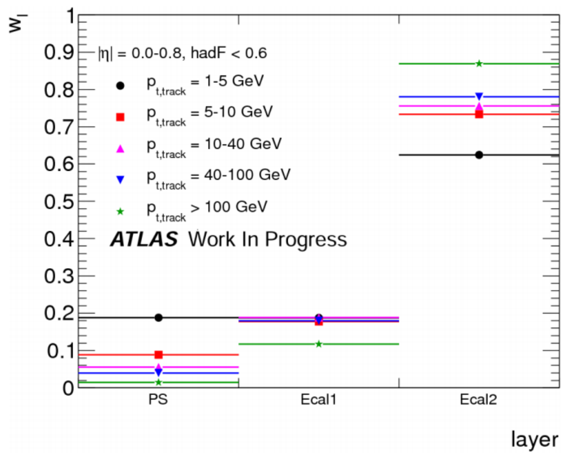

(a) Example of longitudinal weights obtained from a single $\pi^{\pm}$ sample (see Section 4.1.3).

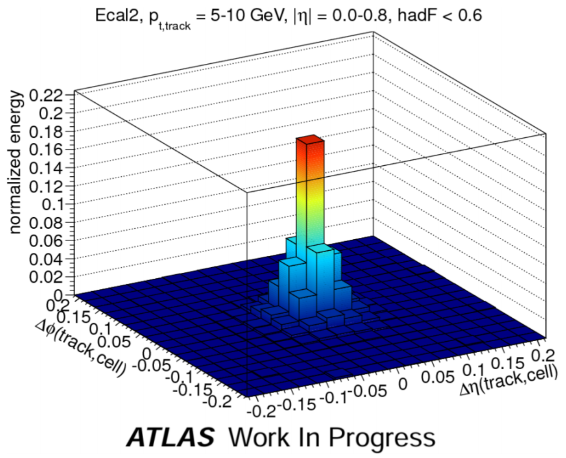

(b) Example of a lateral hadronic shower shape obtained from a single $\pi^{\pm}$ sample (see Section 4.1.3).

Fig. 3.3: Examples of longitudinal and lateral shower shapes used in the cell-based algorithm [26].

mass of the π^0 candidate and the track, are saved for further analyses, such as tau identification and polarization studies. An output BDT score is distribution is given by the BDT. The BDT can be further improved by using strip layer information, as described later in this thesis. The final π^0 clusters are, thus, those that pass the energy preselection the optimized BDT score cut. The optimized p_T threshold and BDT score cut for the selected π^0 clusters from the cell-based algorithm are shown in Table 3.1.

$\lvert\eta\rvert$ range	0.0-0.8	0.8-1.4	1.4-1.5	1.5-1.9	≥1.9
p_T cut for a π^0 cluster	1.5	1.7	1.8	1.5	1.3
BDT score cut for a π^0 cluster	-0.06	-0.14	0.01	-0.1	-0.01

Tab. 3.1: Optimized cluster p_T and BDT score cuts on π^0 clusters from the cell-based algorithm. Each column shows the cut for an η region.

With the identified π^0 clusters, the cell-based algorithm reconstructs the 4-momentum of the visible tau with an energy-flow based method:

$$p_T = \sum_i p_{\text{track}_i} + \sum p_{\pi^0 \text{ clusters}}. \tag{3.4}$$

Thus, the 4-momentum reconstruction relies heavily on the number of reconstructed π^0 clusters, and thus on the tau decay mode classification.

The later sections of this thesis will preface with plots of the cell-based algorithm's performance with tau decay mode classification (Section 4.3), charged pion subtraction (Section 4.4), and 4-momentum resolution (4.5), in order to motivate improvements or alternative approaches to the algorithm.

Chapter 4

Improving Neutral Pion Reconstruction Using Strip Layer Information

The goal of this thesis is to use information from energy depositions in the high-granularity strip layer of the ATLAS ECAL for the improvement of the reconstruction of the substructure of hadronically decaying taus. The tau reconstruction algorithm in ATLAS [27] used for 2011 and 2012 collision data did not fully take advantage of information from the fine segmentation of the cells in the strip layer. Based on the promising results that will be shown in this thesis, the algorithm presented will be incorporated into the tau reconstruction algorithm for the new data from collisions at the LHC in 2015. For the next release of the ATLAS reconstruction algorithm, the new baseline algorithm for tau reconstruction at ATLAS uses photon shots on top of the cell-based algorithm [26] as input into the global tau classifier, PanTau [31].

The following section first presents the data samples used in this thesis. Then, the next section defines the photon shot object and how it is used to reconstruct photons in the strip layer. Section 4.3 will address improvements to tau decay mode classification using these photon shots. Section 4.4 will show the use of shots from charged pions to improve the subtraction of their energy deposits from the strip layer. Section 4.5 will show a study of the feasibility for an alternative approach to predict showers from the π^0 decay products without having to first subtract showers from the $\pi^\pm$.

4.1 Data Samples

Data used in this thesis are from a Monte Carlo generator, called PYTHIA 8.1 [33, 34], of high-energy scattering events from two protons. From here on truth information will refer to the generated data in the Monte Carlo.

4.1.1 Monte Carlo $Z \to \tau\tau$ Sample with Pileup

A Monte Carlo $Z \to \tau\tau$ sample with pileup is used for the developments described in Section 4.2 and the optimization of the tau decay mode classification (Section 4.3). It simulates, as closely as possible, the environment in the ATLAS detector when a Z boson is produced from two colliding protons in the beams under luminosity settings similar to those of the data taken at the LHC in 2012. Figure 4.1 shows the number of reconstructed vertices in the $Z \to \tau\tau$ sample presented in this section. Pileup is added afterward.

The $Z \to \tau\tau$ sample used in this thesis comes from cell-based algorithm that runs as part of the ATLAS tau reconstruction software. The cell-based algorithm requires $E_{\tau\,\mathrm{reco}} > 10$ GeV, ≥ 1 reconstructed hadronically decaying tau that is matched to one true hadronically decaying tau, and $|\eta_{\mathrm{reco}\,\tau}| < 2.5$. Leptonically decaying taus are discarded from the sample. The efficiency of these cuts is approximately

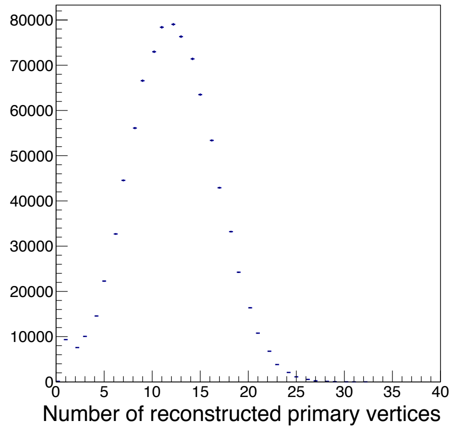

Fig. 4.1: Number of primary vertices in the $Z \to \tau\tau$ sample that have been reconstructed by the tracking algorithm.

50%. Each selection placed on the $Z \to \tau\tau$ sample after the cell-based algorithm and their corresponding efficiencies are shown in Table 4.1. Only events that pass these sections are used in the analyses presented in this thesis. The one-prong selection is applied because the algorithms developed in this thesis are developed on one-prong decays before they can be extended to work on three-prong taus. The tau reconstruction algorithm in [27] reconstructs taus with a p_T greater than 15 GeV, so the analyses in this thesis only use taus above this p_T threshold. The total number events in the sample before selections is $\sim$ 900k. Figure 4.2 shows the p_T and η spectra of all taus in the $Z \to \tau\tau$ samplee that decay hadronically and only uses events that have passed the selections described in Table 4.1. Figure 4.3 shows the p_T spectra of the decay products from the hadronically decaying tau, except for the tau neutrino.

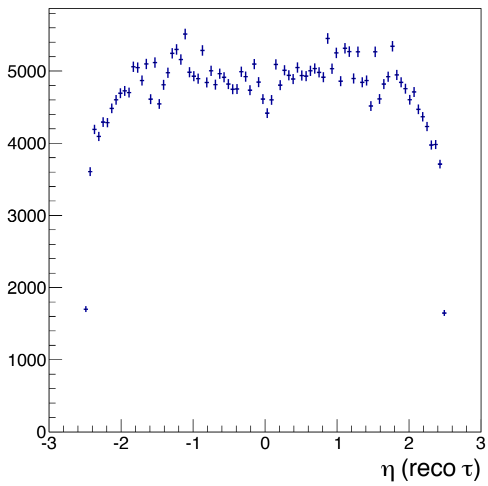

(a) The η spectrum of the reconstructed taus in the $Z \to \tau\tau$ sample.

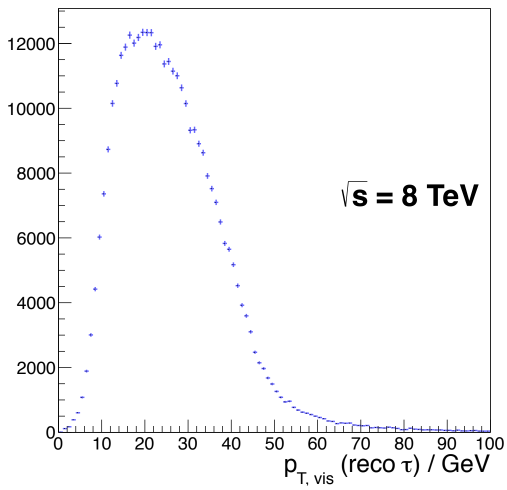

(b) The p_T spectrum of the reconstructed taus in the $Z \to \tau\tau$ sample.

Fig. 4.2: The η and p_T spectra of the reconstructed taus that have decayed hadronically in the $Z \to \tau\tau$ sample with pileup.

Cut Requirement	Efficiency / %
1-prong (in truth and on reconstructed level)	59.0
$p_T^{\text{reco}\,\tau} > 15$ GeV	45.8

Tab. 4.1: Selection efficiencies for the $Z \to \tau\tau$ sample with pileup.

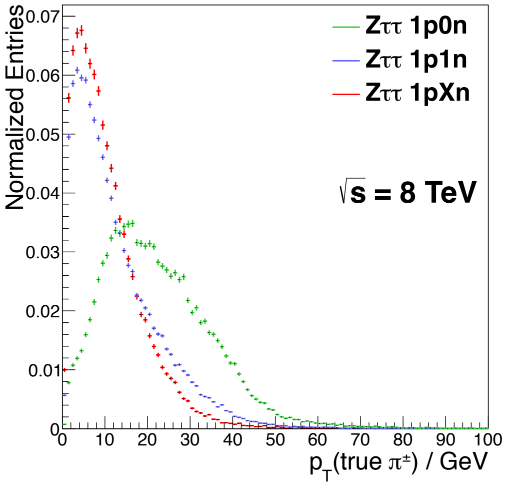

(a) The p_T spectrum of charged pions from hadronically decaying 1-prong taus in the $Z \to \tau\tau$ sample.

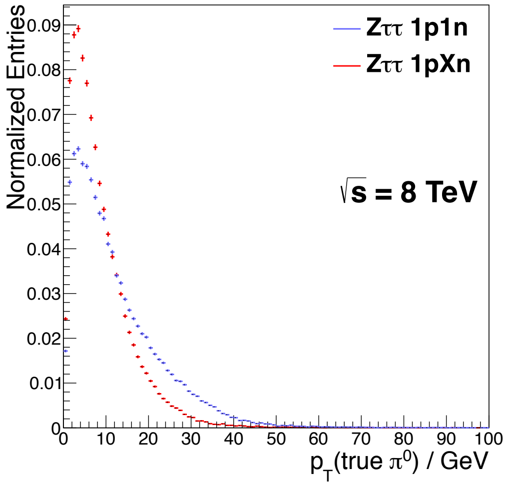

(b) The p_T spectrum of neutral pions from hadronically decaying 1-prong taus in the $Z \to \tau\tau$ sample.

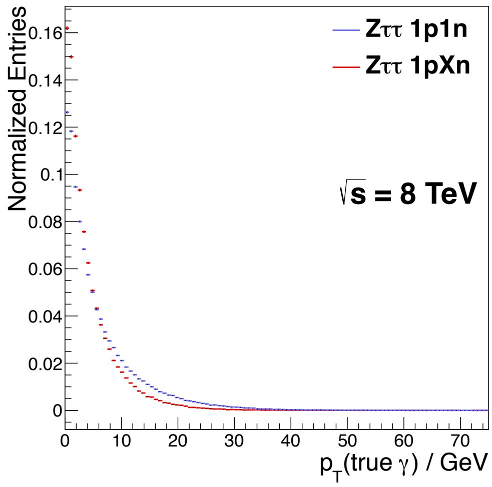

(c) The p_T spectrum of photons from hadronically decaying 1-prong taus in the $Z \to \tau\tau$ sample.

Fig. 4.3: p_T spectra of the visible decay products from a hadronically decaying (excluding ν_τ) in the $Z \to \tau\tau$ sample. Decays of the tau into only one charged hadron are denoted as 1p0n decays of the tau into 1 charged hadron, and 1 (or ≥ 2) neutral pion are denoted as 1p1n (or 1pXn).

4.1.2 Monte Carlo Single π^0 Sample without Pileup

A single particle sample of neutral pions is used for the analysis described in Section 4.2 and some parts of the analysis described in Section 4.3. A topological clustering algorithm was performed on this sample. A single photon sample would have been cleaner and more ideal for the analysis involving the identification of individual photons described later in Section 4.2. However, the only single photon sample available did not have an appropriate p_T spectrum for the study of neutral pions in tau decays since it was produced for studies of the photon reconstruction algorithm in ATLAS that concentrate on high-energy photons [22]. The selections applied on the π^0 sample and their corresponding efficiencies are shown in Table 4.2. The algorithms presented in this thesis are first developed in the barrel region of the ECAL, so a selection of $|\eta| < 1.3$ is applied. Only events where both photons are found within the core isolate cone of $\Delta R < 0.2$ used in the tau reconstruction algorithm are used because measurements of the performance of the algorithms presented in this thesis should not be biased by events where both photons from the π^0 cannot be recovered. Only the events that pass these cuts are used for analyses presented in this thesis. The p_T spectrum of the neutral pions in the single π^0 sample is shown in Figure 4.4.

Cut Requirement	Efficiency / %
$\|\eta\|$<1.3	43.4
Not a Dalitz decay	42.5
Both photons are within ΔR =0.2 cone around the true π^0	32.2

Tab. 4.2: Selection efficiencies for the single π^0 sample without pileup.

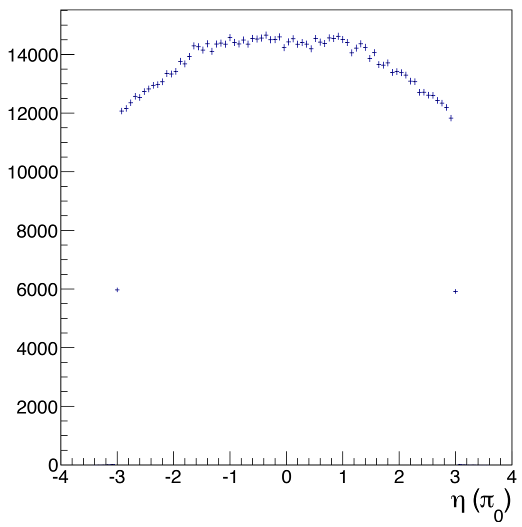

(a) The η spectrum of the true neutral pions in the single π^0 sample.

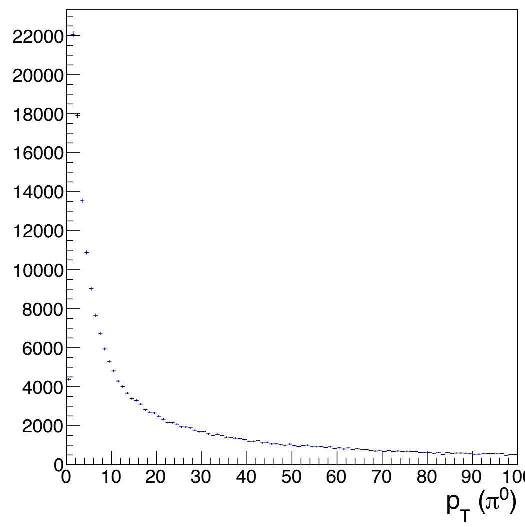

(b) The p_T spectrum of the neutral pions in the single π^0 sample (cf. p_T spectrum of neutral pions in the $Z \to \tau\tau$ sample in Figure 4.3b).

Fig. 4.4: The η and p_T spectra of the true neutral pions in the single π^0 sample.

4.1.3 Monte Carlo Single $\pi^\pm$ Sample without Pileup

A Monte Carlo simulated sample of single charged pions is used for the algorithm described in Section 4.4 for subtracting charged pion energy deposits from the first layer of the ECAL. The number of tracks reconstructed per event is shown in Figure 4.5. The η and p_T spectra of the true charged pions in the sample are shown in Figure 4.6.

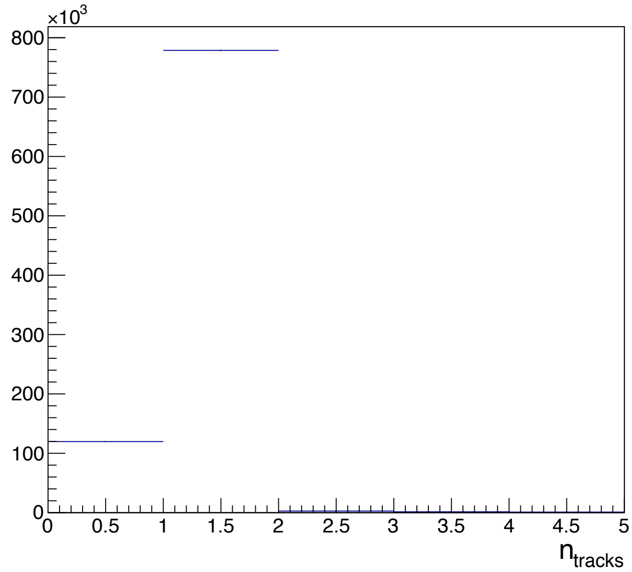

Fig. 4.5: Number of reconstructed tracks per event in the single $\pi^\pm$ sample.

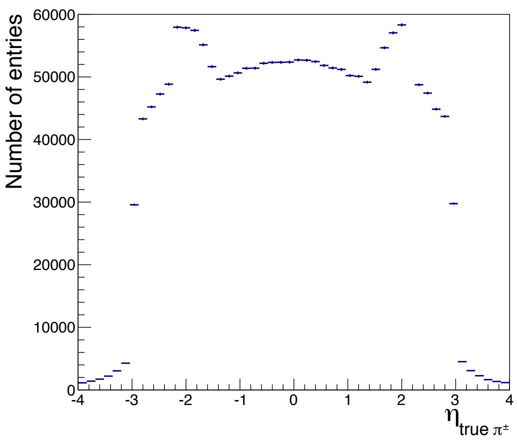

(a) The η spectrum of the true charged pions in the single $\pi^\pm$ sample.

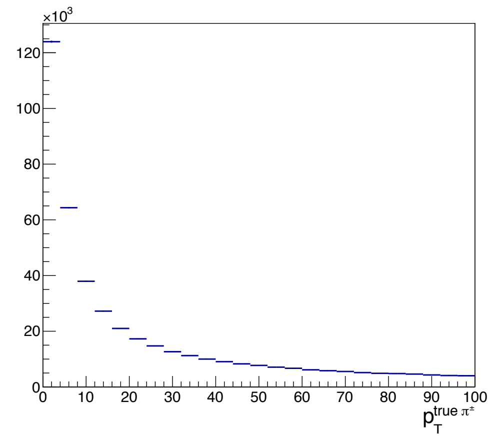

(b) The p_T spectrum of the true charged pions in the single $\pi^\pm$ sample (cf. p_T spectrum of charged pions in the $Z \to \tau\tau$ sample in Figure 4.3a).

Fig. 4.6: The η and p_T spectra of the true charged pions in the single $\pi^\pm$ sample.

4.2 Identifying Photons from Tau Decays in the Strip Layer

The following section presents an algorithm to identify individual photons in ECAL1, or the strip layer, of the ATLAS detector. The analysis uses the single π^0 sample, described previously in Section 4.1.2, unless otherwise noted.

The identification of individual photons from neutral pion(s) in a tau decay requires a calorimeter with good spatial resolution since the the photons in a tau decay can be emitted close together and the start of a photon shower in the strip layer is typically narrow. The average shower shape of an isolated photon showering in the strip layer is shown in Figure 4.7. As can be seen from the RMS values, the photon showers are usually contained within a $\Delta\eta$ of 0.005 and $\Delta\phi$ of 0.09, so the cell dimensions of a strip layer cell in the ECAL barrel of $\Delta\eta \times \Delta\phi = 0.003125 \times 0.098$ mean that the cells are usually thin enough to enable one to identify individual photon showers. Figure 3.1 is an average shower shape showing how

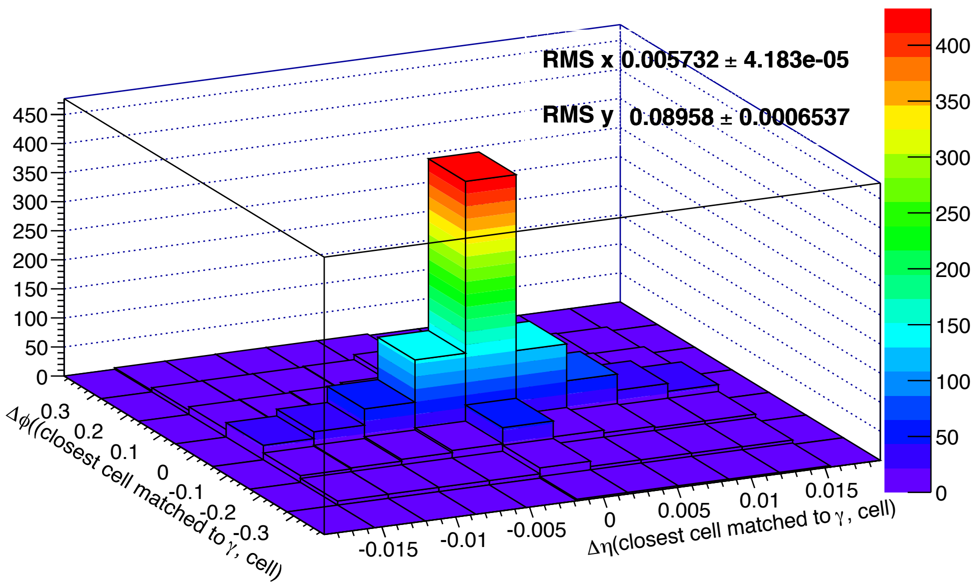

Fig. 4.7: An average photon shape of an isolated photon from a π^0 decay showering in the strip layer. Each bin corresponds to the width of one strip cell in the ECAL barrel region, and the color scale is in GeV. The shower shape was obtained by summing up the p_T found in cells around the position of the photon extrapolated to the strip layer using all the events of the single π^0 sample. A selection is placed that requires the two photons from the π^0 to be isolated.

individual photon showers look in the strip layer. A display of how the cells of the strip layer typically look after energy deposits in the cells found in the tau isolation cone around the reconstructed tau from a $Z \to \tau\tau$ event with pileup is shown in Figure 4.8.

The identification of photons from π^0 decays is unprecedented for tau reconstruction in ATLAS because the tau environment is unique in requiring the identification of photons (as the decay products of one or multiple neutral pions) so close together. For the identification of photons in $H \to \gamma\gamma$, for example, the goal is to reject photons from neutral pions [22]. Figure 4.9 shows the smallest opening angle between the two closest photons in a one prong tau decay with ≥ 0 neutral pions for different p_T categories and how the distance between the photons grows smaller at higher p_T.

Photons from the π^0 in a tau decay begin to shower $\geq 95\%$ of the time in the strip layer. Figure 4.10

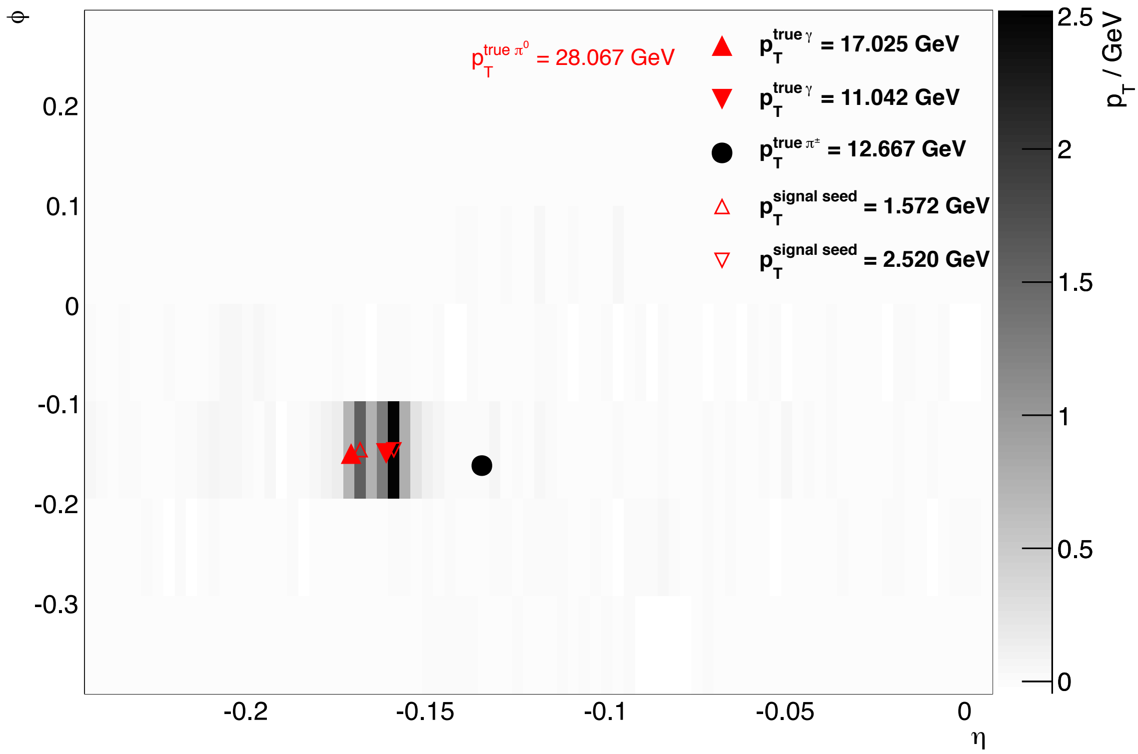

Fig. 4.8: 2-D display of an MC $Z \to \tau\tau$ event in the strip layer. Each bin corresponds to one strip cell. The generated positions of the final state particles are overlaid on top of the cells, with their corresponding p_T values shown in the legend. The position of the true photons are the filled red triangles, and the black circle is the true position of the $\pi^{\pm}$.

shows the fraction of energy deposited on average in the first two layers of the ECAL from a π^0. Neutral pions deposit about 30% of their energy on average in the strip layer, as shown in Figure 4.10a. The majority of the p_T from both photons of the π^0 is deposited in ECAL2, as shown in Figure 4.10b. Photon showers in the strip layer are almost free of leakage from other tau-related particles. The $\pi^{\pm}$ is a minimum ionizing particle in the strip layer and thus starts to shower about 30% of the time in the strip layer and about 50% of the time in ECAL2. Figure 4.11 shows the average amount of energy deposited by the charged pion on average in each layer of the calorimeters. In the second and third ECAL layers, there are major energy deposits from the charged pion, so π^0 identification using information from these latter layers relies heavily on the cell-based subtraction of charged pions.

Photons can be reconstructed as narrow energy deposits in the strip layer. To search for these, this thesis defines a new reconstruction object called a shot. A shot is a local maximum in the energy distribution in the strip layer. This section concentrates on shots used for reconstructing photons in the strip layer. The shot object will later be applied to improving the classification of τ decay modes in Section 4.3. Additional applications of the shot were investigated at the end of this thesis. They include the improvement of the cell-based algorithm's subtraction of energy deposits from the $\pi^{\pm}$ from the strip layer (Section 4.4) and the development of a method completely independent of the $\pi^{\pm}$ subtraction to reconstruct neutral pions using only the strip layer (Section 4.5).

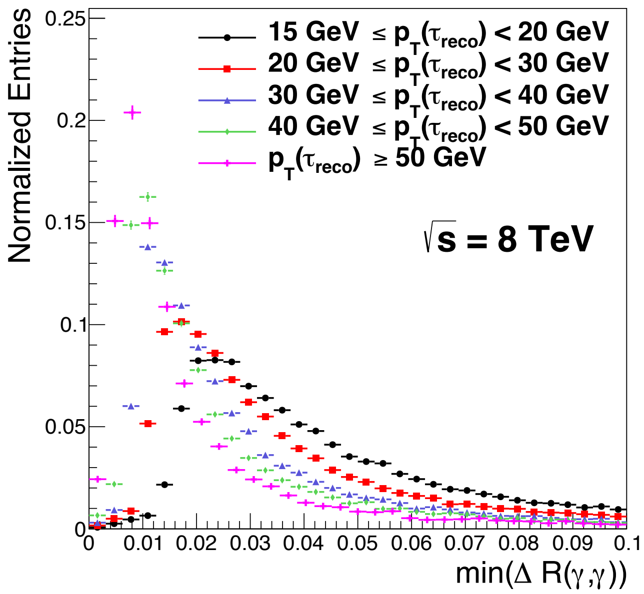

Fig. 4.9: Opening angle, ΔR, between the two photons that are closest to each other in a one prong tau decay with ≥ 0 neutral pions in the $Z \rightarrow \tau\tau$ sample.

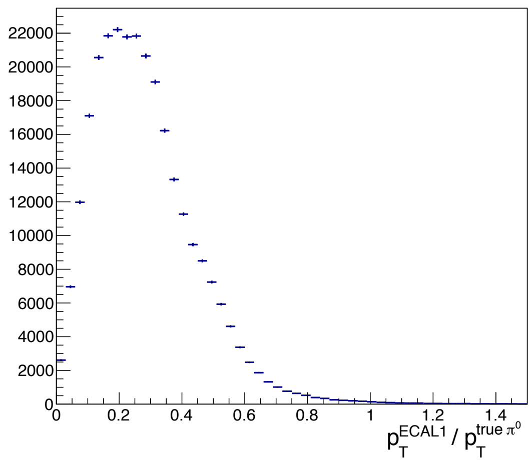

(a) Fraction of π^0 p_T deposited on average in ECAL1.

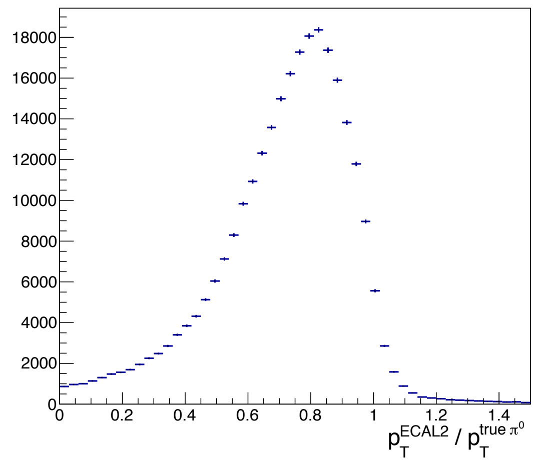

(b) Fraction of π^0 p_T deposited on average in ECAL2.

Fig. 4.10: Fraction of photon p_T deposited on average in ECAL1/2 measured using the single π^0 sample. $p_T^{\mathrm{ECAL1/2}}$ are the sum of the p_T in all cells of the ECAL1 and ECAL2 layer, respectively, found within a $\Delta R < 0.2$ cone around the true position of the π^0.

4.2.1 Photon Showers in the Strip Layer from a Hadronically Decaying Tau

Photons transfer their energy via electromagnetic showers in the calorimeter, and the basic principle of calorimetry in measuring these showers is to record a signal that is proportional to the energy generated by the energy deposition from this electromagnetic avalanche. Local maxima in the distribution of these

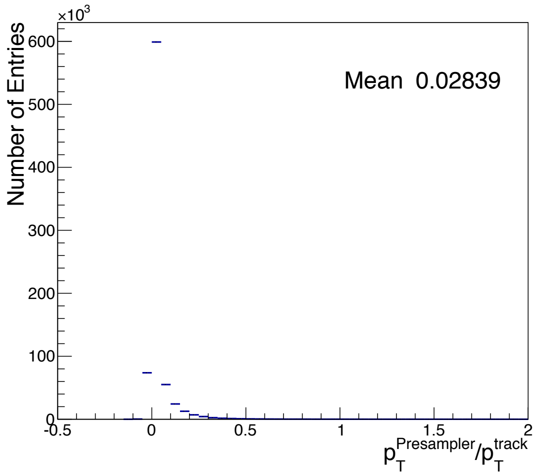

(a) Fraction of $\pi^{\pm}$ p_T deposited on average in the Presampler

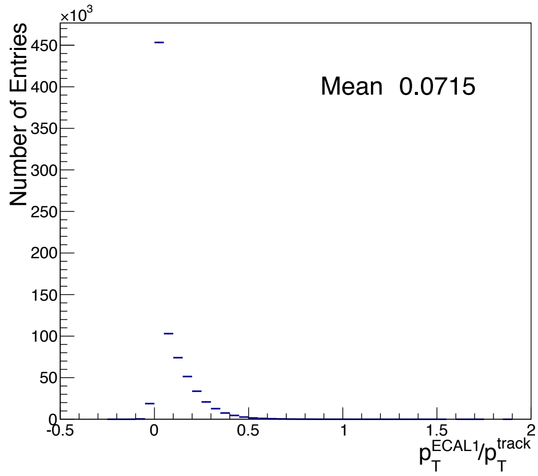

(b) Fraction of $\pi^{\pm}$ p_T deposited on average in ECAL1.

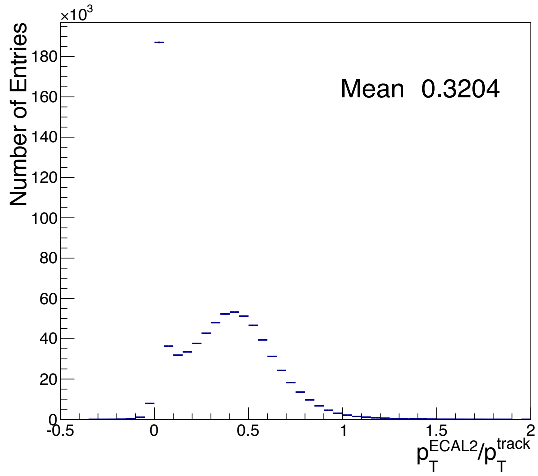

(c) Fraction of $\pi^{\pm}$ p_T deposited on average in ECAL2.

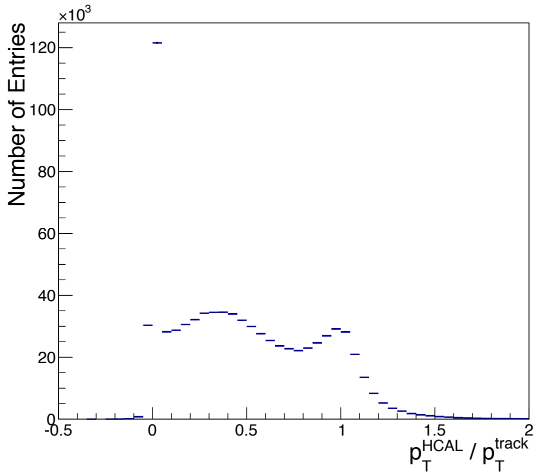

(d) Fraction of $\pi^{\pm}$ p_T deposited on average in the HCAL.

Fig. 4.11: Fraction of $\pi^{\pm}$ p_T deposited on average in each layer of the calorimeters, measured using the single $\pi^{\pm}$ sample. The transverse momenta are the sum of the p_T in all cells of a layer that are contained in a cluster. The HCAL also includes ECAL3, as explained in Section 3.2.1.

energy deposits will be the basis for finding a photon shot in the strip layer.

Photons are highly likely to shower in the strip layer. An upper bound on the probability of a photon to make a shot can be predicted by the probability of a photon to convert in the strip layer. The probability of a photon to convert in the strip layer is given by

$$P(\text{photon converts in strip layer}) = 1 - e^{-\frac{7}{9}N_{\text{rad}}}, \tag{4.1}$$

where $N_{\text{rad}} \approx 4.3$ is the number of radiation lengths of the strip layer for the barrel and end-cap, as shown in Figure A.2a and Figure A.2b. The radiation length is the mean path length after which the energy of a relativistic charged particle is reduced by a factor of $\frac{1}{e} = 0.368$. By $\frac{9}{7}$ radiation lengths, 63% of the incident photons have converted to $e^{+}e^{-}$ pairs. Considering the material in the strip layer, the probability would be approximately 96.5%.

4.2.2 Local Maximum Finder to Identify Seed Cells for Candidate Photon Shots

As mentioned above, shots are local maxima in energy deposits in the strip layer. An example display of two local maxima created by the photon daughters of a π^0 decay in a $Z \rightarrow \tau\tau$ event is shown in Figure 4.8. The strip cells are usually narrow enough so that the two photons from the π^0 create their own local maxima.

The seeding, or shot-finding, algorithm identifies candidate shots by searching for local maxima in the strip layer. The legitimacy of identifying a deposit from a photon as one local maximum will be explained when quantifying the p_T threshold for a local maximum. There are three tunable setups for the local maximum finder:

1. The p_T threshold that the center cell, or seed cell, of a local maximum must pass in order to be considered a candidate shot. This seed cell is the cell whose p_T is compared to the neighboring cells to check if the neighboring cells have lower p_T than the seed cell.

2. The number of neighboring cells around the seed cell in η checked to see if they have lower p_T than that of the seed cell.

3. The association of another local maxima created across ϕ to the candidate shot.

First, to determine a threshold on the cell's p_T to consider it as a seed cell, the lowest threshold possible is determined that will not discard too many signal photon shots, while allowing the algorithm to reduce background photon shots caused by electronic noise or fluctuations in the electromagnetic shower. A preliminary threshold for a candidate photon shot is investigated in this section, and a final p_T threshold is optimized in Section 4.3. Figure 4.12a shows local maximum cases in which the algorithm would pick up more than one seed cell per isolated photon. This occurs from, for example, fluctuations in the electromagnetic shower and from electronic noise.

To quantify the local maximum case shown in Figure 4.12a at a certain p_T threshold, the following variable is defined:

$$\Delta p_T = p_T^{\text{second neighbor to seed cell}} - p_T^{\text{first neighbor to seed cell}}, \tag{4.2}$$

where $\Delta p_T < 0$ would mean the photon shower has fluctuations that would cause the algorithm to pick up more than one local maximum for that photon. This variable is akin to the strip layer variable ΔE used for electron and photon identification in ATLAS [22], so it is reasonably safe to assume that Monte Carlo simulation agrees with data. Figure 4.13 shows Δp_T from Equation 4.2 vs. the p_T of the second neighbor in η to the seed cell. A threshold of 100 MeV on the second neighboring cell will limit these fluctuation cases shown in 4.12a to a $\leq$1% of the time. Therefore, a preliminary p_T threshold of 100 MeV is placed on candidate shots.

The algorithm only checks if one neighboring cell on either side of a cell in η has lower energy than the seed cell. It is important that the fewest number of neighboring cells possible is checked to verify if there is a local maximum in the energy distribution. This is because, at higher p_T, the photons from the π^0 are emitted closer together, as shown previously in Figure 4.9. Also, the neutral pions in tau decays into multiple neutral pions are emitted closer together at higher p_T.

The algorithm does not check if neighboring cells in ϕ have lower p_T than the seed cell, so it is possible to have two candidate seed cells at the same η position and in juxtaposing ϕ layers. The seeding algorithm can pick up extra seed cells across ϕ when

- A photon lands on the border between two cells across ϕ, as shown in Figure 4.14.

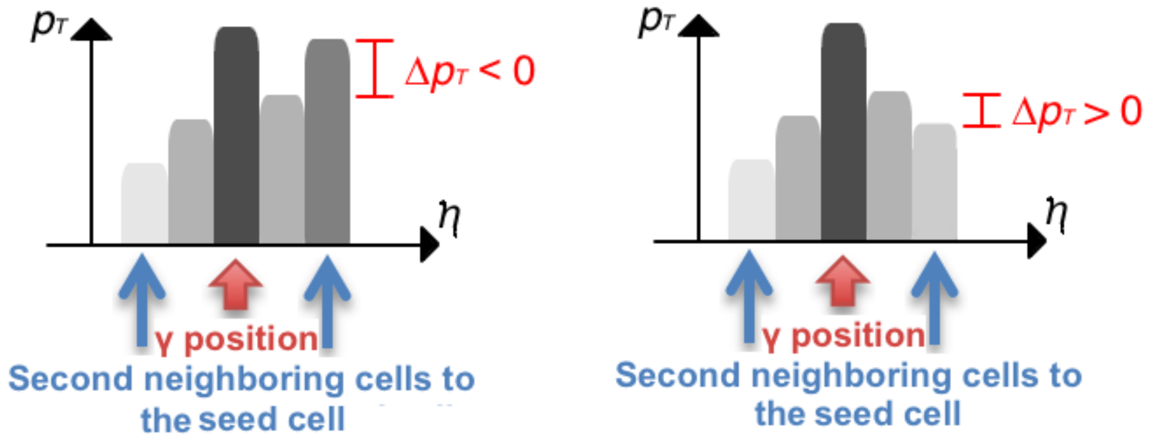

(a) Case where fluctuation causes the algorithm to pick up two local maxima created by one photon

(b) Case where there is no fluctuation, so the algorithm picks up one local maximum created by one photon

Fig. 4.12: Schematic of local maximum cases.

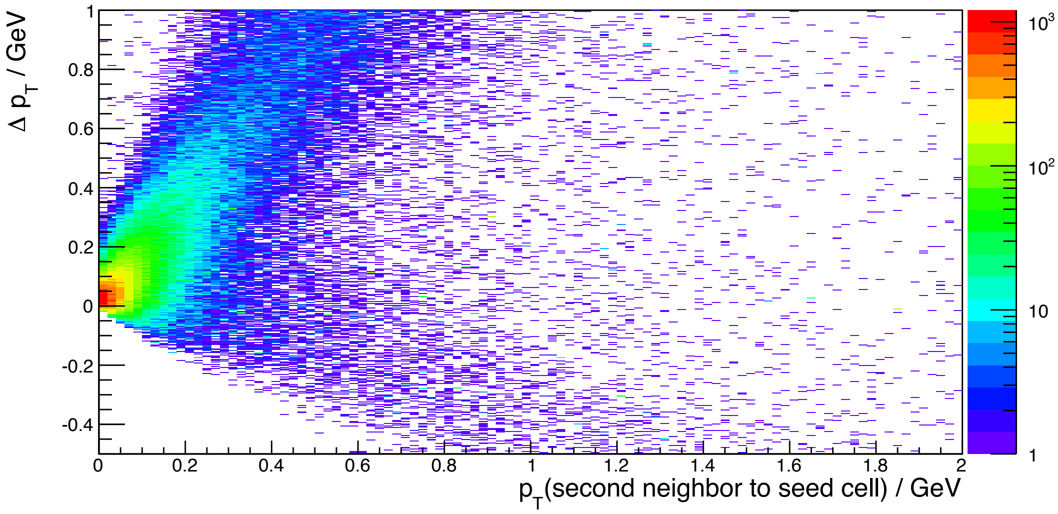

Fig. 4.13: The Δp_T variable defined in Equation 4.2 vs. p_T of the second neighboring cell to the seed cell for isolated photons in the single π^0 sample.

- A photon converts and the e^+e^- pair creates two local maxima across ϕ, since the bending of charged particles in ATLAS is in ϕ.

To choose the area in which two shots must fall in order to be matched together, a measurement is performed to check how much is gained by matching across different $\Delta\eta \times \Delta\phi$ areas. The gain in performance should be larger than the performance lost by erroneously matching two signal shots from the two distinct photons. Table 4.3 shows that two shots are created directly across ϕ by one photon about 9% of the time and only 4% of the time by two photons. If the ϕ-matching area criterion is increased to a cell area of 3×1 cells up/down with respect to the seed cell of the shot (see Figure 4.15b), the algorithm would gain about 3% of the shots created diagonal to each other by one photon, but, for about 6% of the time, these two shots are created legitimately by two photons. There should not

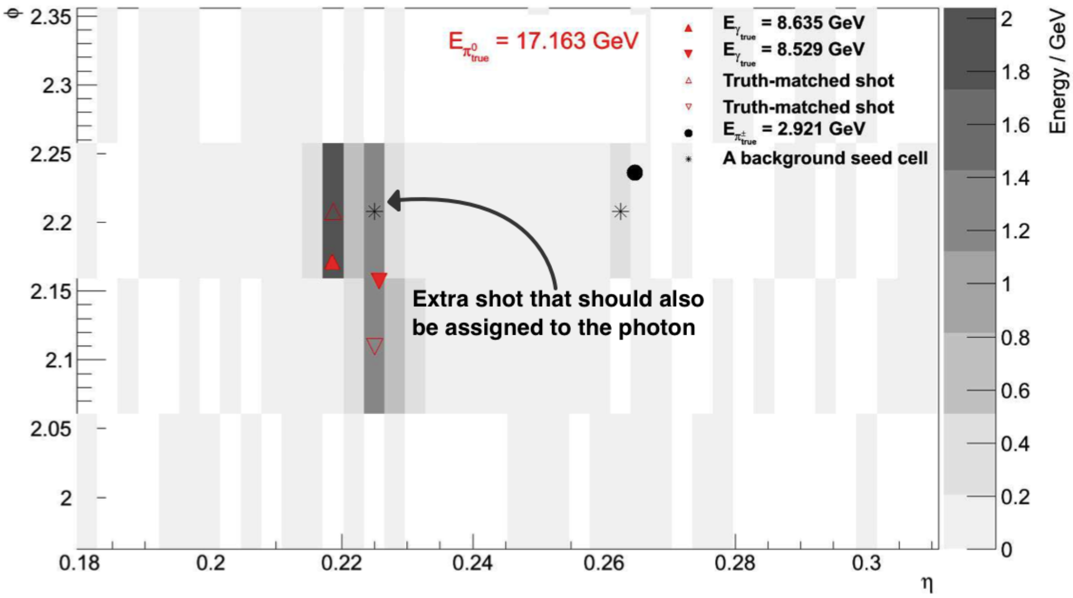

Fig. 4.14: Display of an event in the $Z \to \tau\tau$ sample where a photon creates two shots across ϕ. In this event, $E \approx p_T$ since $\eta \approx 0$.

be a greater loss of photons than there are shots gained by the ϕ-matching. Therefore, the ϕ-matching window is chosen to be 1×1 cells, i.e., the algorithm must find two shots next to each other in ϕ, in the same η layer (see Figure 4.15a).

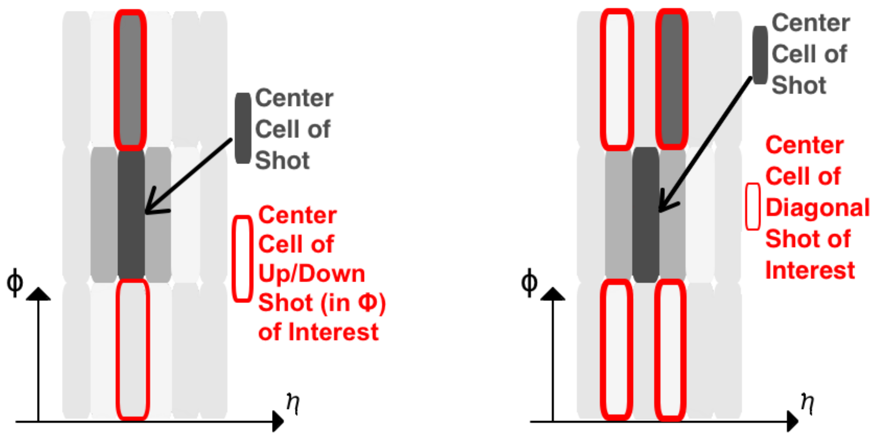

(a) Extra shot up/down in ϕ.

(b) Extra shot diagonal in ϕ.

Fig. 4.15: Schematics of the ϕ-matching setups considered.

Therefore, if two shots, shot a and shot b, lie immediately to each other in ϕ, a linear interpolation of both shots is performed to determine the new ϕ value. The new quantities of the shot, shot', are

$$\phi' = \frac{(p_{T,a} \cdot \phi_a) + (p_{T,b} \cdot \phi_b)}{p_{T,a} + p_{T,b}} \tag{4.3}$$

$$p'_T = p_{T,a} + p_{T,b}. \tag{4.4}$$

	Percentage of total shots
No shot is found in a $\Delta\eta \times \Delta\phi$ area of 3×1 strip cells up/down wrt (with respect to the) signal shot	87.8%
A shot is found immediately up/down in ϕ wrt signal shot (see Figure 4.15a)	8.8%
A shot is found in diagonals in ϕ wrt signal shot (see Figure 4.15b)	3.3%

Tab. 4.3: ϕ-matching: Percent gain for different $\Delta\eta \times \Delta\phi$ setups.

	Percentage of total shots
The two truth-matched photon shots are not found in a $\Delta\eta \times \Delta\phi$ area of 3×1 strip cells with respect to each other	90.7%
The two truth-matched photon shots found in adjoining ϕ cells	3.8%
The two truth-matched photon shots are found in diagonal ϕ cells	5.4%

Tab. 4.4: ϕ-matching: Percent loss for different window sizes

4.2.3 Truth-Matching of Candidate Shots to True Photons

The seeding algorithm will pick up any shot found in the $\Delta R \leq 0.2$ cone around the reconstructed tau, but the shots of interest, i.e. signal shots, are those corresponding to a true photon from the MC data (see Section 4.1.2). To identify these signal shots for further studies, a so-called truth-matching of each true photon to the closest shot is performed. The truth-matching procedure assigns the closest shot to the extrapolated position of the true photon in the strip layer. To determine the truth-matching area in which a shot must fall with respect to the true photon, an $\eta \times \phi$ area is defined so that as many true photons are matched to a shot as possible without mistakenly matching a background shot to a true photon. Separate area sizes for η and ϕ are defined, instead of a ΔR cone, because of the asymmetry in the widths of the cells in the strip layer in η and ϕ coordinates (see Table A.1). Figure 4.16 shows $\Delta\eta$ and $\Delta\phi$ between the true photon and the shot truth-matched to this photon, vs. $p_T^{\text{true}\,\gamma}$. The reasoning behind Figure 4.16 is that higher p_T photons are more likely to be matched to a true signal shot. The entries in each category of the p_T of the true photon are normalized to one so that the fraction of cases that fall within a certain $\Delta\eta$ can be clearly seen for each p_T.

From these distributions for the ECAL barrel region, a reasonable truth-matching threshold to apply for the barrel region, is $\eta \times \phi = (0.003125 \cdot 1.5) \times (0.098 \cdot 0.6)$. For the extension to the end cap, where cell sizes vary, the algorithm uses $1.5 \cdot \text{cell width}_\eta \times 0.6 \cdot \text{cell width}_\phi$. An example display of a $Z \to \tau\tau$ event after a truth-matching of shots to photons is shown in Figure 4.17. The truth-matching efficiency is $\sim 95\%$, and it is determined by requiring isolated photons in the single π^0 sample (at least 5 strip cell widths in η apart and 2 strip cell widths in ϕ apart) and checking if a shot is found within an area around the true position of the photon of $2.5 \cdot \text{strip cell width}_\eta \times 1 \cdot \text{strip cell width}_\phi$.

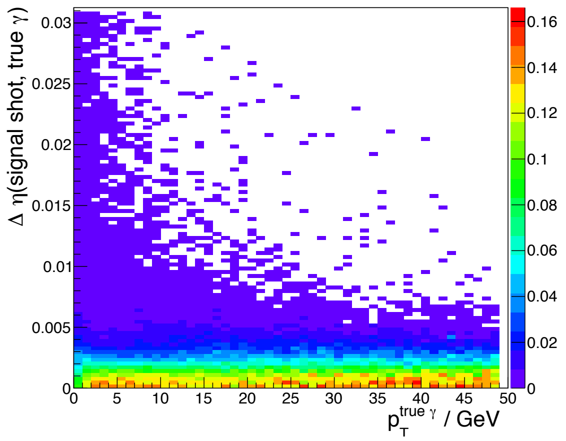

(a) $\Delta\eta$ between true photon and closest photon shot to that photon, with entries normalized to unity for each p_T category.

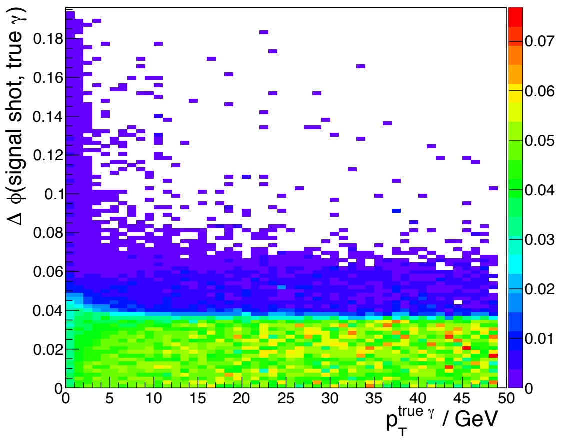

(b) $\Delta\phi$ between true photon and closest photon shot to that photon, with entries normalized to unity for each p_T category.

Fig. 4.16: Distance between an isolated true photon in the single π^0 sample and the closest shot to that photon.

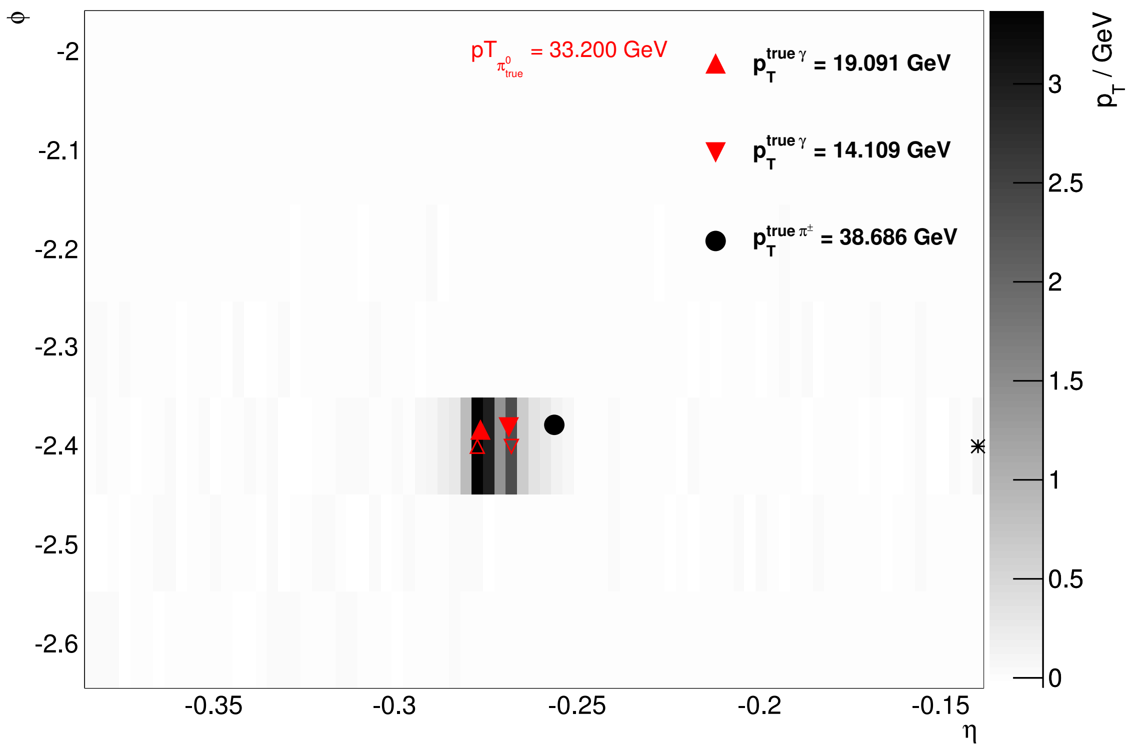

Fig. 4.17: Display of the cells found in the isolation cone around the tau from the $Z \to \tau\tau$ sample after truth-matching of shots to photons. The hollow red triangles mark the center of the seed-cell that has been matched to the generated photon (filled red triangle). The position of the π^0 is not shown to avoid an overlap of symbols.

4.2.4 Performance of Shot Seeding

Before progressing on to the applications of the photon shots, the performance of the photon shot seeding in the single π^0 sample is first measured. The more realistic case of using the local maximum finder to identify photons in the $Z \to \tau\tau$ sample with pileup will be addressed in Section 4.3. The performance is quantified by efficiency, defined in the next section, and purity, defined in the section following the next section.

Efficiency of shot-finding

A true photon in the single π^0 sample can fall into one of the following categories:

- The true photon is truth-matched to the same shot as the other photon from the parent π^0 .
- The true photon is truth-matched to its own shot.
- The true photon is not truth-matched to any shot.

In addition, a true π^0 in the single π^0 sample falls into one of the following cases:

- Both photons from the π^0 are truth-matched to the same shot.
- Both photons from the π^0 are truth-matched to their own shot.
- One photon is truth-matched to a shot while the other from the π^0 is not.
- Both photons from the π^0 are not truth-matched to any shot.

The efficiency for each of these cases is

$$\text{Efficiency} = \frac{\text{Total number of photons categorized to a certain case}}{\text{Total number of photons considered in the truth-matching procedure}}. \tag{4.5}$$

Figure 4.18a shows the probability for a truth-matched shot to fall into one of the above categories on an individual photon level (Figure 4.18a) and on an individual π^0 level (Figure 4.18b). These figures can be interpreted as the probability of a shot to be of a certain type vs. the p_T of the photon (Figure 4.18a) and the π^0 (Figure 4.18b). By definition, a photon or a π^0 fits into only one of the cases, so the efficiency at each p_T category necessarily adds up to one. At higher p_T, the probability for a shot to be created by two photons begins to dominate over the probability of a shot to be created by one photon. This occurs because the two photons from the π^0 will be produced with a larger boost, thus ending up in the same shot. The region in the π^0 level plot where only one photon is recovered is caused by cases where a photon is so low p_T that it either does not deposit energy or is neglected by the 100 MeV threshold. This happens for a significant percentage of cases because the p_T shared between the two photons from the π^0 tends to be asymmetric. Figure 4.19 shows the p_T asymmetry, binned by the p_T of the π^0. The p_T asymmetry between the two photons is defined as

$$p_T^{\text{asymmetry}} = \frac{p_T^{\text{leading } p_T\ \gamma} - p_T^{\text{subleading } p_T\ \gamma}}{p_T^{\text{leading } p_T\ \gamma}}, \tag{4.6}$$

where "leading" denotes the photon with the higher p_T. This p_T asymmetry does not depend on the boost from the neutral pion. Another possible case is when a legitimate shot fails the truth-matching requirement (cf. truth-matching efficiency of ~ 95% from Section 4.2.3). It is important to note that a large percentage of cases where only one photon is missing will not necessarily degrade the performance of photon shots used for tau decay mode classification, later described in Section 4.3.

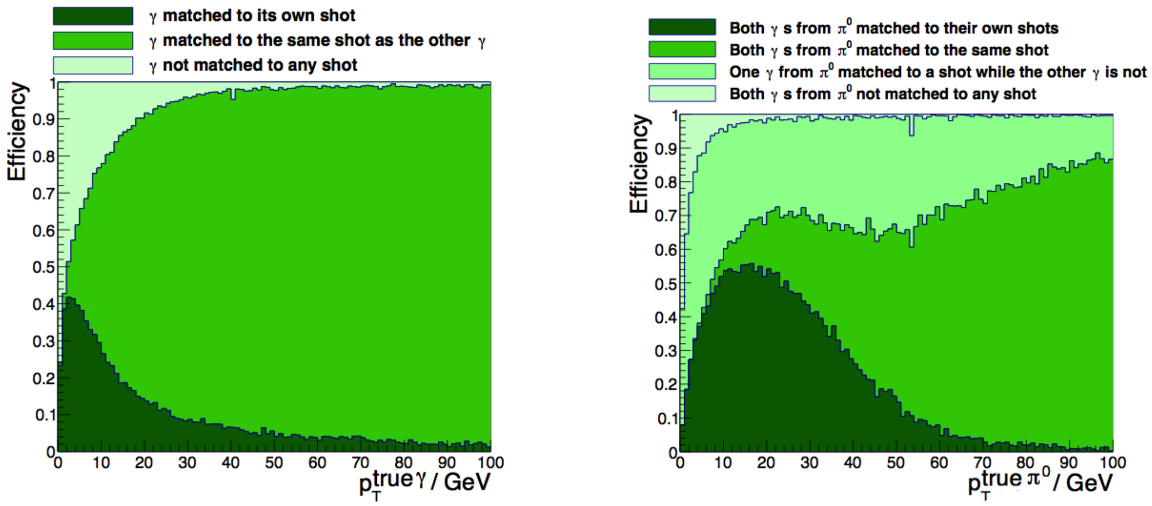

(a) Efficiency of the seeding algorithm to pick up a shot from a photon in the single π^0 sample, on an individual photon level. (No selection was applied for whether or not a photon converts.)

(b) Efficiency of the seeding algorithm to pick up a shot from a photon in the single π^0 sample, on an individual π^0 level. (No selection was applied for whether or not a photon converts.)

Fig. 4.18: Efficiency of the seeding algorithm to pick up a shot from a photon in the single π^0 sample.

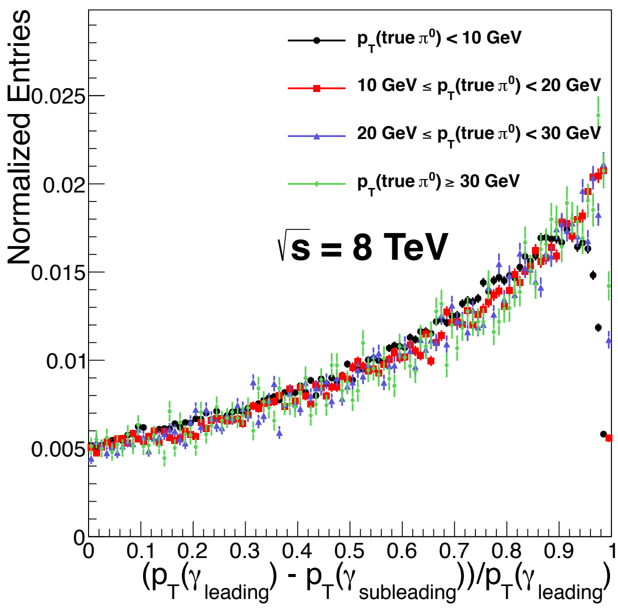

Fig. 4.19: Asymmetry in p_T between the lower p_T photon and the higher p_T photon from a π^0 decay in the $Z \to \tau\tau$ sample.

Purity of shot-finding

The purity of the shot-finding is

$$\text{Purity} = \frac{\text{Total number of shots truth-matched to a } \gamma}{\text{Total number of shots picked up by the seeding algorithm}}. \tag{4.7}$$

Figure 4.20 shows the purity of the shot-seeding vs. the p_T of the seed cell before ϕ-matching. This plot tells us the probability that a seed picked up by the algorithm is a truth-matched signal photon shot vs. the seed cell's p_T. As expected, the probability is higher at high p_T. The purity was calculated by dividing the number of signal events in a p_T category by the total number of events in a p_T category. Recalling from Table 4.3, the cases of interest for the ϕ-matching occur about 9% of the time. Given

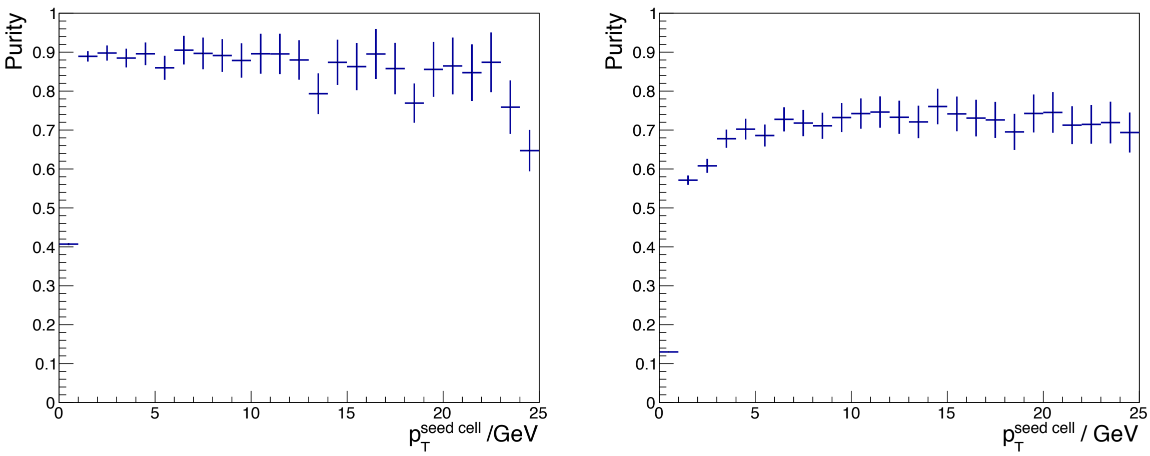

(a) Purity for the case where the photon has not converted. (b) Purity for the case where the photon has converted.

Fig. 4.20: Purity obtained by the shot-finding algorithm before ϕ-matching.

that the purity of photon shots in the single π^0 sample plateaus at 90%, it can be seen, as expected, that the purity after interpolation across ϕ layers reaches close to 100%. Figure 4.21 shows the purity after the ϕ-matching of shots for converted and uncovered photons. The ϕ-matching helps more in the cases where the photon has converted, since the bending of the products from a converted photon is in ϕ. It can also be see that the improvement is higher for lower energy photons after the ϕ-matching. This is expected because lower energy photons will produce the e^+e^- pair further apart from each other, since there is a smaller boost.

4.2.5 Photon Conversions

Photons convert in the strip layer $\sim$50% of the time. To determine if they are a problem for shot finding, even after the ϕ-matching, the average distance between the e^+e^- daughters in the strip layer from a photon conversion is measured. This can be predicted by

$$R_{\text{conv}}^{\text{approx}} = \sqrt{\frac{d_0 \cdot p_T}{0.15 \cdot B}}, \tag{4.8}$$

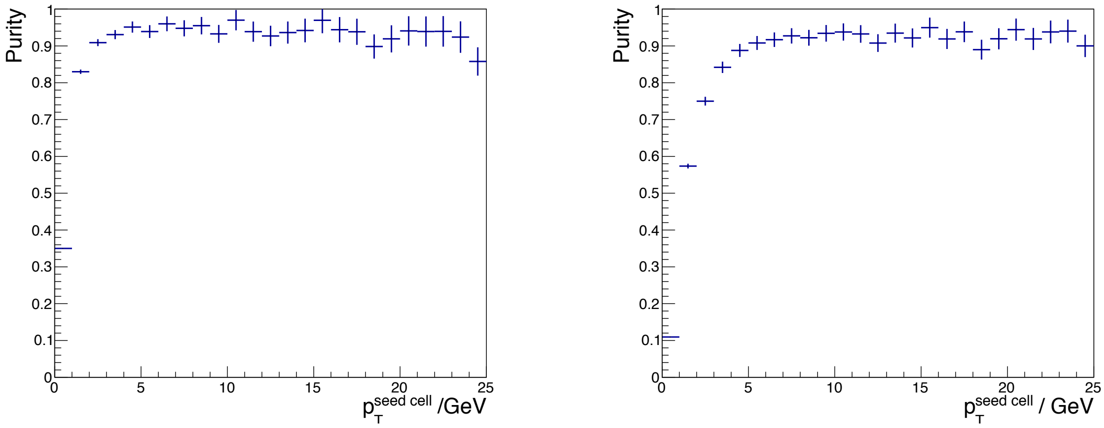

(a) Purity for the case where the photon has not converted after ϕ-matching.

(b) Purity for the case where the photon has converted after ϕ-matching.

Fig. 4.21: Purity obtained by the shot-finding algorithm after ϕ-matching

where d_0 is the impact parameter and B is the strength of the magnetic field. Figure 4.22 shows the distance in the strip layer, in units of η and ϕ, between the e^+e^- pair from a photon conversion in the single π^0 sample. Each bin corresponds to the width for one strip cell in the barrel region of the ECAL. For these distributions, selections have been placed requiring that the photon has been flagged as having converted before entering the strip layer and also that the π^0 is found in the barrel of the ECAL ($|\eta| < 1.3$). The daughters of a photon conversion are found within an area of $\Delta\eta \times \Delta\phi = (0.003125 \cdot 2) \times (0.098 \cdot 2)$ about 60% of the time. Since the dimensions of an ECAL1 barrel cell are $\Delta\eta \times \Delta\phi = (0.003125 \times 0.098)$, photon conversions should not be too much of a problem for the shot seeding, especially with the matching across ϕ.

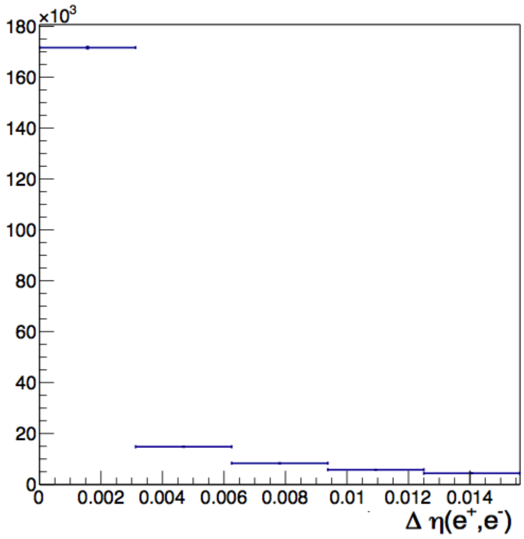

(a) $\Delta\eta$ between the e^+e^- pair from a photon conversion.

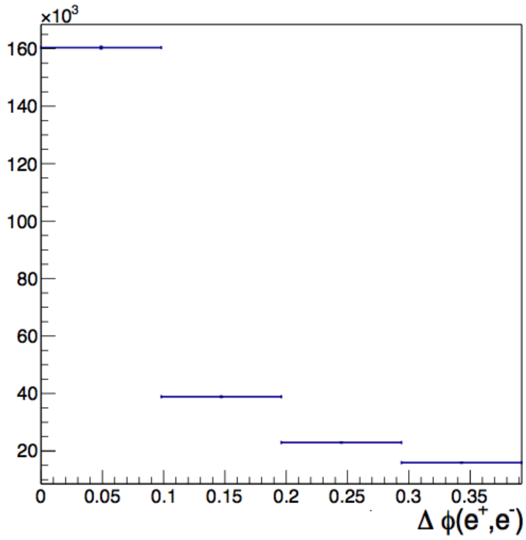

(b) $\Delta\phi$ between the e^+e^- pair from a photon conversion.

Fig. 4.22: Distance in the strip layer between the photon conversion products for photons found in the barrel (π^0 sample). Each bin corresponds to one cell width in η (left) and ϕ (right).

4.3 Improving the Classification of τ Decay Modes by Counting Photons

This section delineates the use of photon shots to improve the τ decay mode classification for the one-prong case. Improving the cell-based algorithm's counting of the number of neutral pions from a one-prong τs is important because it will

- Improve the percentage of correctly classified ρ decays (purity for ρ decays) for polarization studies.
- Improve 4-momentum resolution of reconstructed taus. The energy-flow based 4-momentum reconstruction in the cell-based algorithm needs to be provided the right clusters to work with, as described in Equation 3.4. The degradation in energy and directional resolution from the current cell-based algorithm have a strong contribution from falsely classified taus.
- Better discriminate between hadronically decaying τs and multi-jet background. This helps the τ identification algorithm in ATLAS [27], since more background is expected, for example, in an a_1 decay than in a ρ decay.

The figure of merit used to measure the performance of tau decay mode classification is the percentage of correctly classified τ decay modes:

$$\text{Figure of merit} = \frac{\text{Total number of } \tau\text{s whose decay mode has been correctly reconstructed}}{\text{Total number of } \tau\text{s reconstructed}}. \tag{4.9}$$

The figure of merit weights each decay mode according to the relative branching fractions of the sample used. For the cell-based algorithm without shots, the decay modes of a hadronically decaying tau are correctly reconstructed 66.6% of the time, for taus found in the barrel region of the ECAL. The quality of the classification of tau decay modes is judged using the migration matrix. In the migration matrix, the rows are the decay mode of the tau in truth, and the columns are the reconstructed decay mode of the tau. The diagonal entries correspond to taus with correctly reconstructed decay modes. For the purposes of this thesis, this is a 3×3 matrix. For the development of the algorithm, only one-prong candidates, or taus with only one charged hadron as a decay product, are first considered, and these one-prong candidates can fall into one of three categories: zero neutral pions (1p0n), one π^0 (1p1n), or more than one π^0 (1pXn). Taus decaying into more than one π^0 are grouped together into one entry since the branching fractions are negligible and distinguishing decays with more than two π^0s is not relevant for the purposes of polarization studies.

The purity matrix shows the entries in the migration matrix normalized to unity by row, and the efficiency matrix shows the entries in the migration matrix normalized to unity by column. Figure 4.23a shows the purity matrix and Figure 4.23b shows the efficiency matrix for the cell-based algorithm in the barrel region before further improvement of the decay mode classification from shot-finding. The efficiency for $\tau \to \rho(\to \pi^{\pm}\pi^0)\nu_\tau$ decays is 70.8% and the efficiency for $\tau \to a_1(\to \pi^{\pm}\pi^0\pi^0)\nu_\tau$ decays is 45.9%. The purity for ρ decays is 70.1% for the cell-based algorithm without shots. To improve the performance, the off-diagonal entries should be migrated to the correct diagonal entries.

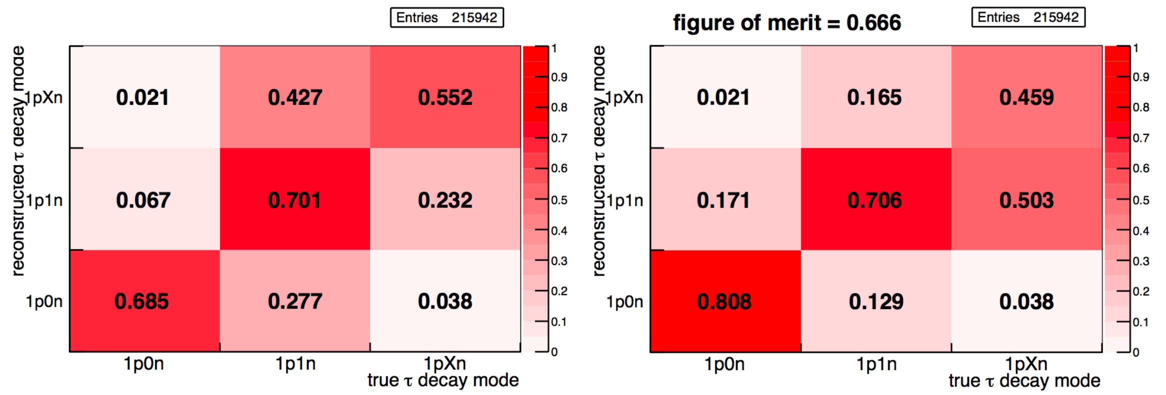

(a) Purity matrix for cell-based algorithm for barrel region ($|\eta| < 1.3$).

(b) Efficiency matrix for cell-based algorithm for barrel region ($|\eta| < 1.3$) before applying shots.

Fig. 4.23: Efficiency and purity matrices for cell-based algorithm for reconstructed taus found in the barrel region before the application of photon shot counting. Only one-prong tau decays are shown.

4.3.1 Counting Neutral Pions Using Shots

This section focuses mainly on the migration of 1pXn taus wrongly classified as 1p1n back to the 1pXn diagonal entry in the migrationn matrix. The decay mode of these taus is wrongly classified for several reasons. One reason is when more than one photon from the neutral pion(s) are found in the same π^0 cluster. An example event display of this case is shown in Figure 4.24. The other reason is when the cell-based algorithm discards a legitimate cluster from a π^0 because it, for example, fails the p_T threshold or does not pass the BDT score threshold (cf. Section 3.2.1). Figure 4.25 shows the number of true photons matched to a π^0 cluster for true 1pXn decays that have been incorrectly reconstructed as 1p1n decays. It shows that the former case happens 50% of the time. This is the case where the counting of individual photons using photon shots is needed.

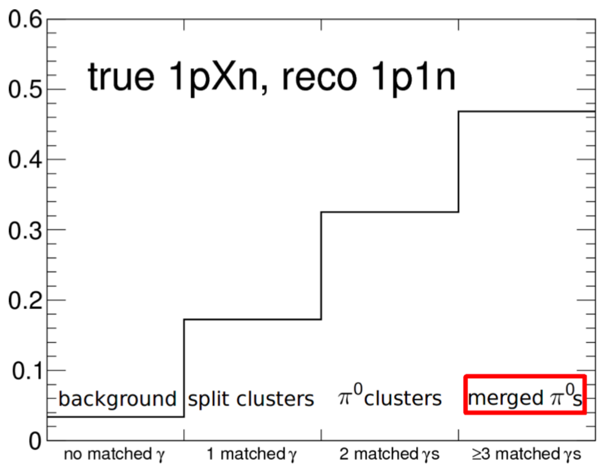

Fig. 4.25: Number of photons matched to a selected cluster for taus decaying to 1pXn that have been wrongly reconstructed as 1p1n in a $Z \to \tau\tau$ sample [26].

In the algorithm developed, if >2 photons are counted using shots, then the one-prong τ is classified as

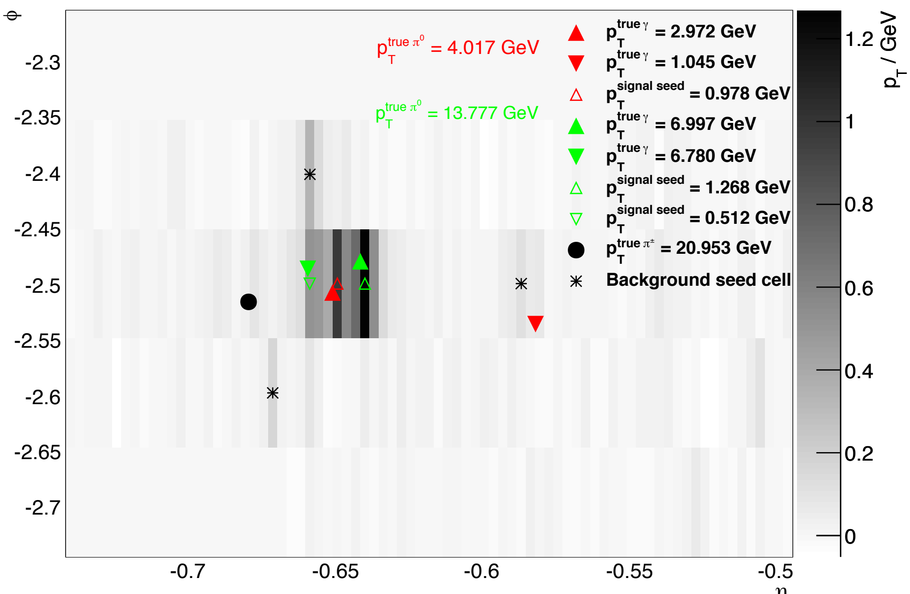

Fig. 4.24: A display of the energy deposits in cells in the isolation cone around the tau from the $Z \to \tau\tau$ sample where ≥ 3 γs from two neutral pions (red, green) in an a_1 decay are found in the same cluster, causing the algorithm to count only one π^0. Here the shot counting algorithm picks up ≥ 3 photons found in the same cluster.

decaying into 1pXn. In Section 4.2, the shot-finding algorithm was shown to recover at least one photon from a π^0 in more than 90% of the time (see Figure 4.18b). This section summarizes the algorithm developed in this thesis to to handle these candidates and differentiate the decays of intermediate a_1 and ρ mesons in tau decays. The procedure is first developed on candidates in the barrel region and then is extended to the endcap. The algorithm is only used if the cell-based algorithm has reconstructed only one π^0 cluster, since the goal is to migrate decays that have been wrongly reconstructed as 1p1n decays, due to the fact that ≥ 3 photons are found in the same cluster, to the 1pXn decay entry in the migration matrix.

1. First, the algorithm searches shot seeds in order to identify photons, as described in Section 4.2.
2. Then, it counts photons by only counting the number of shots whose seed cell belongs to a π^0 cluster that has been identified by the cell-based algorithm.
3. Shots that are within an area of $\Delta\eta \times \Delta\phi$ = (cell width$_\eta \cdot 1.5$) $\times$ (cell width$_\phi \cdot 0.6$) are discarded in order to avoid counting a shot created by a $\pi^{\pm}$. This cell area is taken from the truth-matching thresholds described in Section 4.2.
4. Then, with the identified shots, the algorithm performs the ϕ-matching described in Section 4.2 to minimize cases where an extra shot across ϕ is created from conversion or photons landing on a border between two cells.
5. Next, a p_T threshold is placed on the shots to discard background shots and increase purity.

Figure 4.26 shows the number of photons counted after each step that has just been described vs. the p_T of the true π^0 in order to validate the performance after each step. The algorithm would ideally count two photons in the single π^0 sample. The one step that Figure 4.26 does not show is the track veto step, since there is no track in the single π^0 sample. From Figure 4.26b showing number of photons counted after the ϕ-matching step to Figure 4.26c showing the number of photons after an optimized p_T threshold is placed on the seed cell of the shots, the probability of counting more than two photons in the single π^0 sample is reduced from $\sim$ 80% to more than 95%. However, the caveat is that the p_T threshold causes the algorithm to discard shots, so the probability of counting zero photons in the single π^0 sample also increases. Since the branching ratio of taus decaying via the ρ resonance is 2.5 times larger than that of taus decaying via the a_1 resonance, it is better for the algorithm to undercount photons, hence damaging the fraction of correctly classified 1p1n decays, than to overcount photons, which would increase the fraction of correctly classified 1pXn decays.

The same type of distributions is shown for the realistic case of shot counting in the $Z \to \tau\tau$ sample with pileup for 1p1n decays in Figure 4.27 (and 1pXn decays in Figure 4.28) in distributions for the efficiency of counting a certain number of photons.

- Figures 4.27a and 4.28a show the distributions for the efficiency of counting a certain number of photons by searching for shots whose center cell is found in a π^0 cluster in 1p1n and 1pXn decays, respectively.
- Figures 4.27b and 4.28b show the distributions for the efficiency of counting a certain number of photons after vetoing shots found near the track from the $\pi^\pm$ in 1p1n and 1pXn decays, respectively.
- Figures 4.27c and 4.28c show the distributions for the efficiency of counting a certain number of photons after vetoing shots found near the track from the $\pi^\pm$ in 1p1n and 1pXn decays, respectively.
- Figures 4.27d and 4.28d show the distributions for the efficiency of counting a certain number of photons after placing an optimized p_T threshold on the center cell of the shot in 1p1n and 1pXn decays, respectively. It is important to note that the figure of merit improves when the number of photons shots is undercounted rather than overcounted because the branching ratio for 1p1n decays is 2.5 larger than that of 1pXn decays.

These figures also include an additional track veto step to discard a shot that is too close to the track, and thus may have been created by a charged pion rather than a photon. Only reconstructed taus with a p_T greater than 15 GeV are shown because the tau reconstruction algorithm only reconstructs taus above this p_T (cf. Section 3).

As shown in Figure 4.21, the seeding algorithm picks up many low p_T background shots. For the p_T threshold placed on the center cell of a shot, the threshold has been optimized so that the algorithm correctly classifies the tau decay mode as often as possible. The optimization finds the p_T thresholds in three different η regions for which the figure of merit value from Equation 4.9 is highest. It is performed using the $Z \to \tau\tau$ sample with pileup.

The η binning used for the optimization of the p_T thresholds on the center cell of the shots is determined according to the amount of detector material before the strip layer and the varying cell sizes. The photon shot counting is not used in the transition regions between the barrel and the endcap, so the $1.3 \leq |\eta| < 1.5$ region is discarded. The optimized p_T thresholds for each η bin after optimization are shown in Table 4.5. The optimized p_T threshold has the lowest value for the $|\eta| \geq 1.8$ bin, since there are fewer readout channels in the endcap and thus less noise. The highest optimized p_T threshold is found in the $1.5 \leq |\eta| < 1.8$ bin since it is the region with the longest longitudinal depth of the ECAL and the region with the most material before the calorimeter. The photons are more likely to have showered before entering the strip layer in this region and deposit more energy.

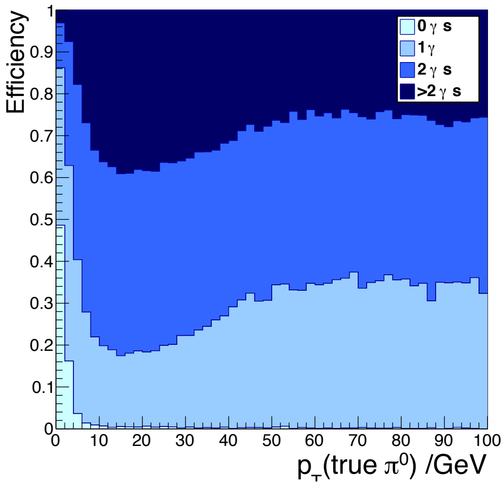

(a) Distribution of the efficiency for counting a certain number of photons after shot seeding with a 100 MeV threshold vs. the p_T of the true π^0.

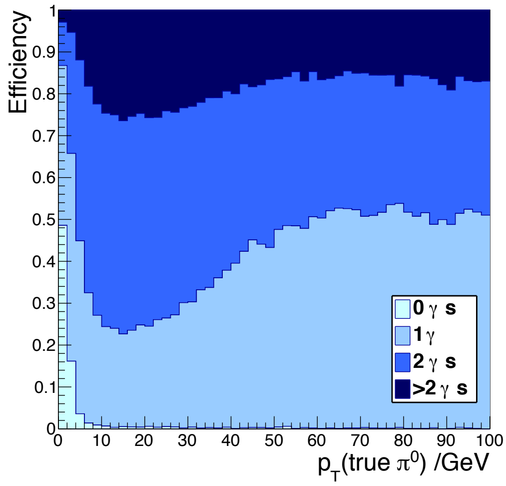

(b) Distribution of the efficiency for counting a certain number of photons after ϕ matching vs. the p_T of the true π^0.

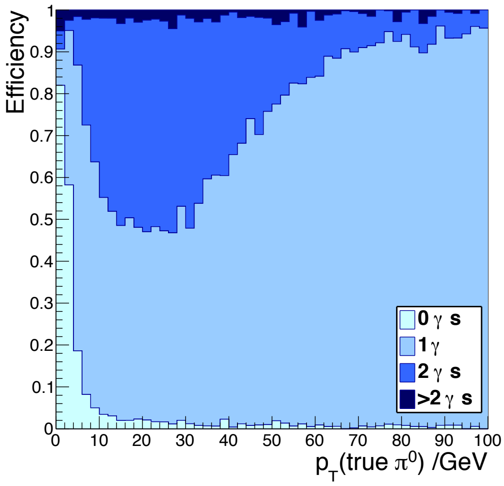

(c) Distribution of the efficiency for counting a certain number of photons after optimized p_T threshold vs. the p_T of the true π^0.

Fig. 4.26: Distribution of the efficiency for counting a certain number of photons after each step of the algorithm. The distributions show the performance of the photon shot counting algorithm for the single π^0 sample without pileup where the π^0 is found in the barrel region, $|\eta| < 1.3$.

η bin	p_T threshold
$|\eta| < 1.3$	$p_T > 420$ MeV
$1.5 \leq |\eta| < 1.8$	$p_T > 600$ MeV
$|\eta| \geq 1.8$	$p_T > 350$ MeV

Tab. 4.5: Thresholds on the p_T of the center cell of a shot for different η regions.

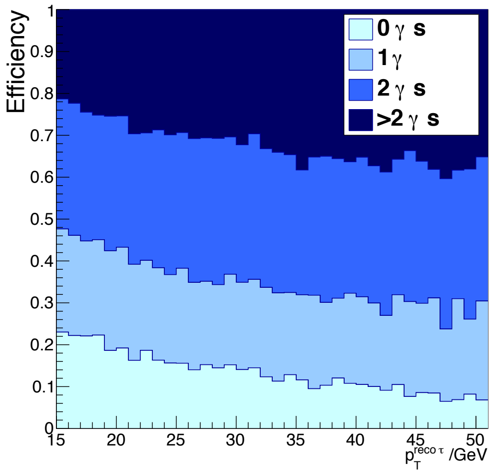

(a) Distribution of the efficiency for counting a certain number of photons after shot seeding with a 100 MeV threshold vs. the p_T of the reco τ for 1p1n decays.

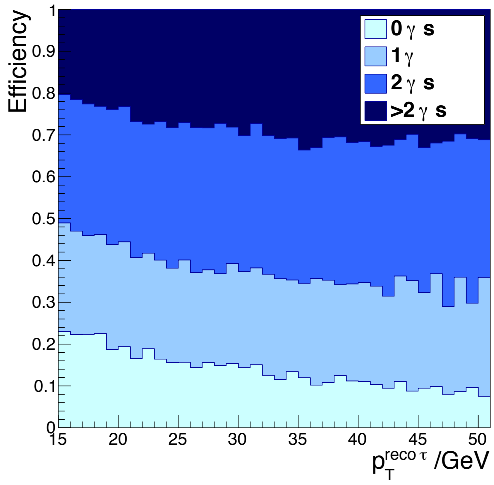

(b) Distribution of the efficiency for counting a certain number of photons after vetoing shots near the $\pi^{\pm}$ track vs. the p_T of the reco τ for 1p1n decays.

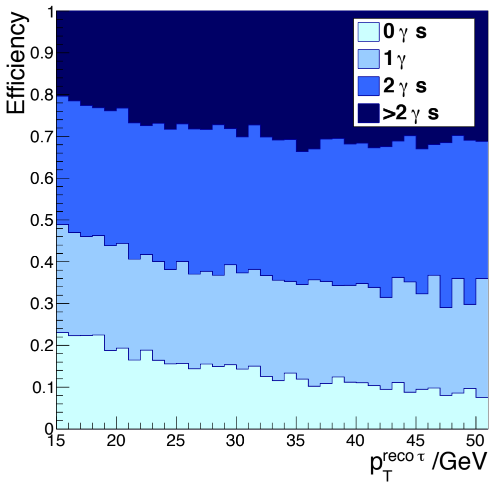

(c) Distribution of the efficiency for counting a certain number of photons after ϕ matching vs. the p_T of the reco τ for 1p1n decays.

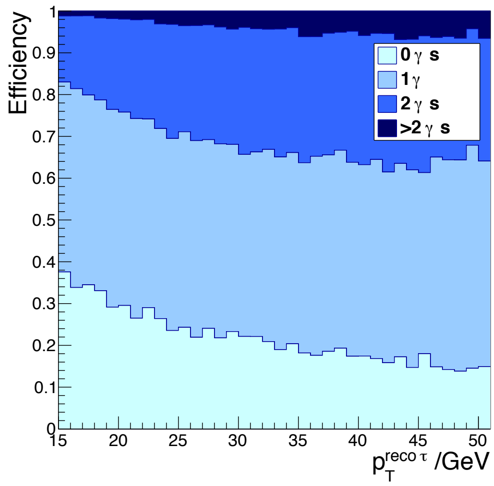

(d) Distribution of the efficiency for counting a certain number of photons after optimized p_T threshold of 420 MeV vs. the p_T of the reco τ for 1p1n decays.

Fig. 4.27: Distribution of the efficiency for counting a certain number of photons after each step of the algorithm. The plots in this figure show the performance for 1p1n decays in the $Z \rightarrow \tau\tau$ sample with pileup where the reconstructed tau is found in the barrel region $|\eta| < 1.3$.

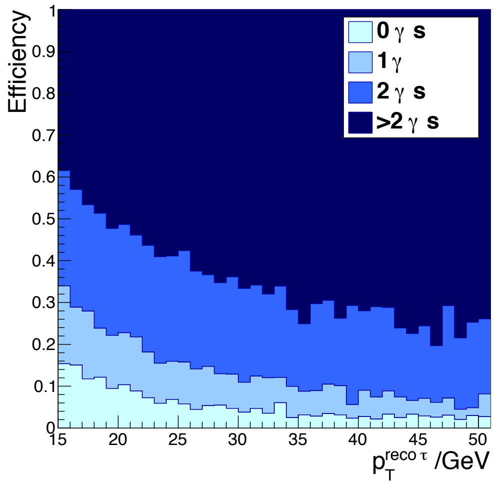

(a) Distribution of the efficiency for counting a certain number of photons after shot seeding with a 100 MeV threshold vs. the p_T of the reco τ for 1pXn decays.

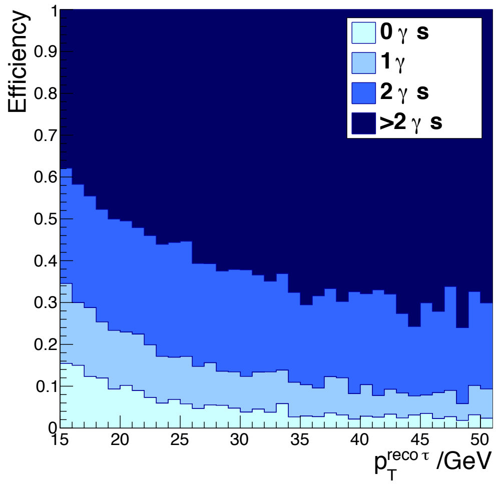

(b) Distribution of the efficiency for counting a certain number of photons after vetoing shots near the $\pi^{\pm}$ track vs. the p_T of the reco τ for 1pXn decays.

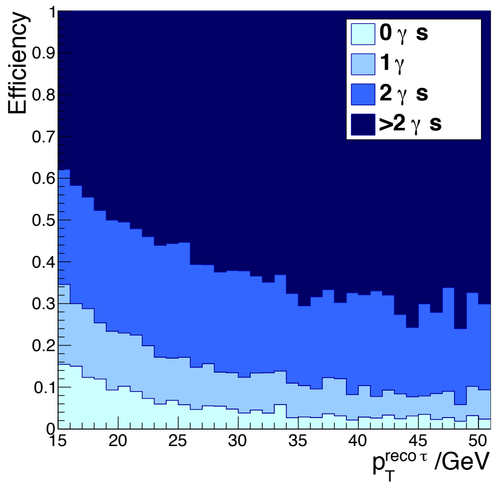

(c) Distribution of the efficiency for counting a certain number of photons after ϕ matching vs. the p_T of the reco τ for 1pXn decays.

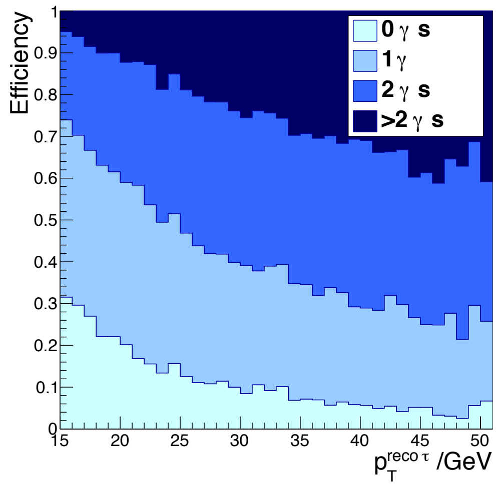

(d) Distribution of the efficiency for counting a certain number of photons after optimized p_T threshold of 420 MeV vs. the p_T of the reco τ for 1pXn decays.

Fig. 4.28: Distribution of the efficiency for counting a certain number of photons after each step of the algorithm. The plots in this figure show the performance for 1pXn decays in the $Z \to \tau\tau$ sample with pileup where the reconstructed tau is found in the barrel region, $|\eta| < 1.3$.

Figure 4.29 shows the performance in the purity and efficiency matrices for the barrel region after applying shots using the method described above with the cell-based algorithm. The purity and efficiency matrices for the two endcap η categories are shown in Figure 4.30 and Figure 4.31. For comparison, Figures 4.30 and 4.31 also show the performance of the cell-based algorithm before photon shot counting. The shot-finding algorithm still improves decay mode classification in the endcap region, even though the larger cell sizes in this region mean the photons are more likely to be found in the same cell. The percent point gains by running shot-finding on top of the cell-based algorithm are shown in Table 4.6.

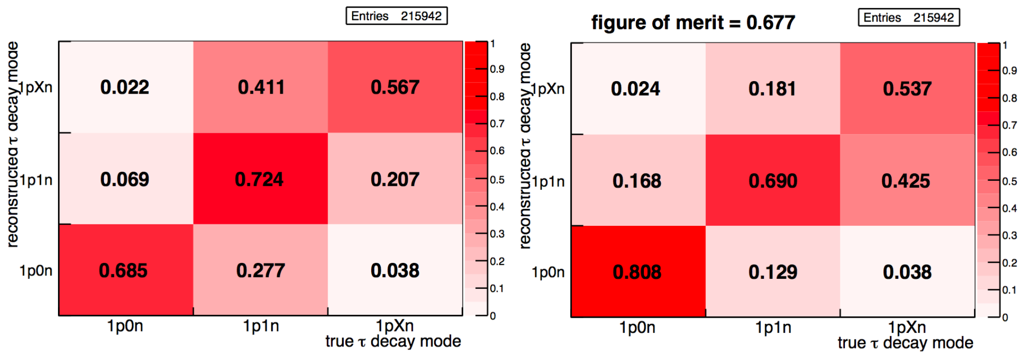

Fig. 4.29: Purity (left) and efficiency (right) matrices for cell-based algorithm with the application of photon shot counting for the barrel region, $|\eta| < 1.3$.

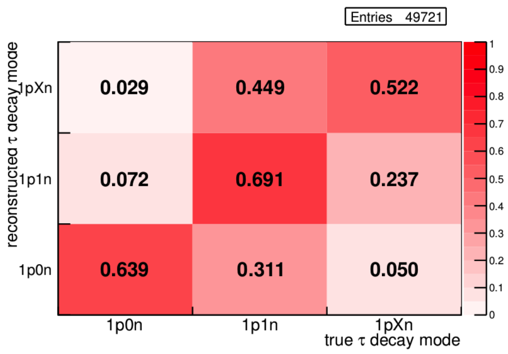

(a) Purity matrix before the application of photon shot counting.

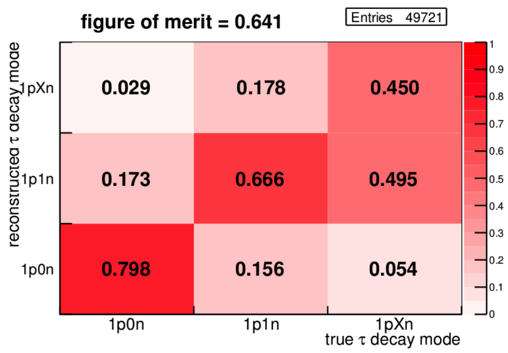

(b) Efficiency matrix before the application of photon shot counting.

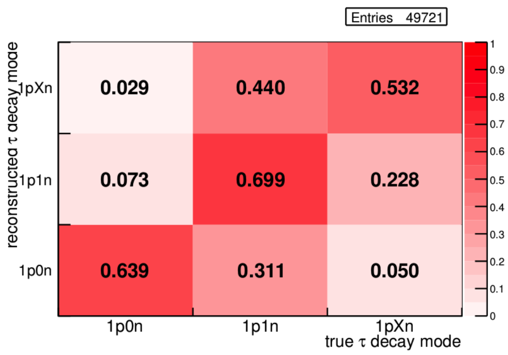

(c) Purity matrix after the application of photon shot counting.

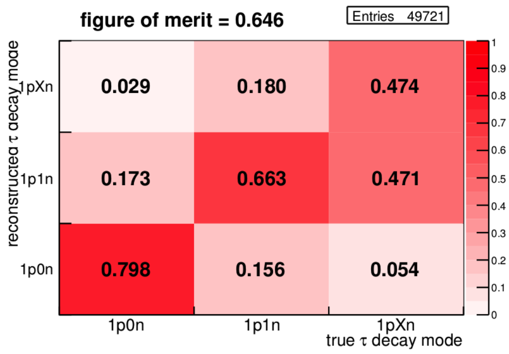

(d) Efficiency matrix after the application of photon shot counting.

Fig. 4.30: Efficiency and purity matrices for cell-based algorithm before (top row) and after (bottom row) the application of photon shot counting ($1.5 \leq |\eta| < 1.8$).

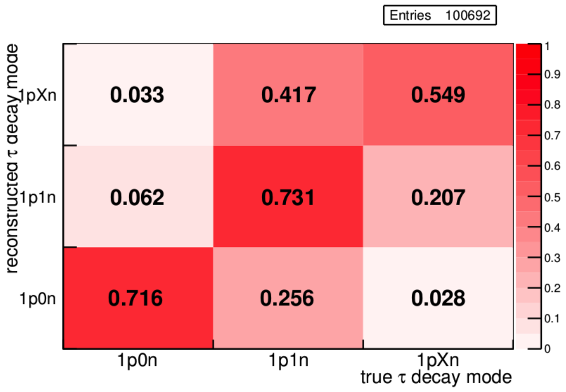

(a) Purity matrix before the application of the shot counting algorithm.

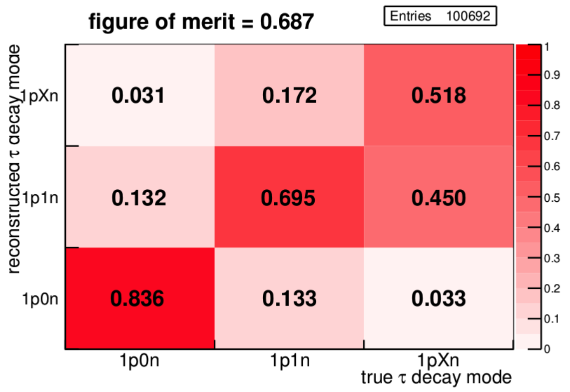

(b) Efficiency matrix before the application of the shot counting algorithm.

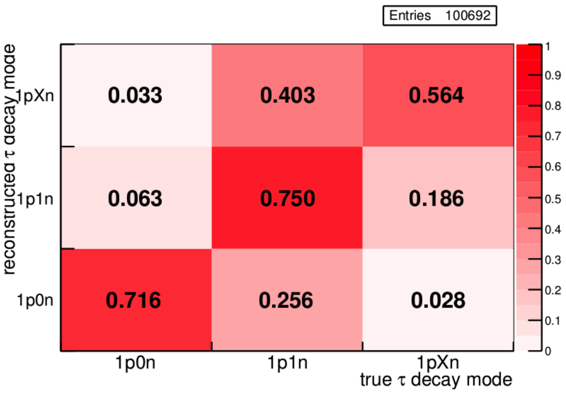

(c) Purity matrix after the application of the shot counting algorithm.

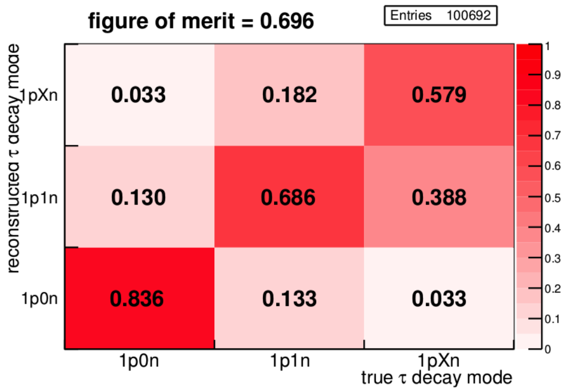

(d) Efficiency matrix after the application of the shot counting algorithm.

Fig. 4.31: Efficiency and purity matrices for cell-based algorithm before (top row) and after (bottom row) the application of photon shot counting ($|\eta| \geq 1.8$).

$\|\eta\|$ bin	Gain in purity for ρ decays	Decrease in ρ background	Gain in a_1 efficiency
$\|\eta\| < 1.3$	3.28	7.69	17.00
$1.5 \leq \|\eta\| < 1.8$	1.16	2.59	5.33
$\|\eta\| \geq 1.8$	2.60	7.06	11.78

Tab. 4.6: Results of the improvement of τ decay mode classification in units of percentage points.

4.3.2 Further Improvements

The photon shot counting algorithm can be further improved by distinguishing between shots created by one photon and more than one photon. As shown previously in Section 4.2, both photons from the π^0 can deposit their energy into the same strip cell. This would cause the photon shot counting algorithm using shots to count only one photon when it should count two. Figure 4.33a shows the probability of a shot to be created by one or two photons vs. the p_T of the seed cell of a shot. Each p_T category is normalized to unity. At high values, for example, a shot is more likely to have been created by two photons. Figure 4.32 shows a schematic of a double-shot, which is a case where two shots are created and separated by only one cell in η but in the same row of cells in ϕ. For these cases, each shot is more likely to have been created by only one photon.

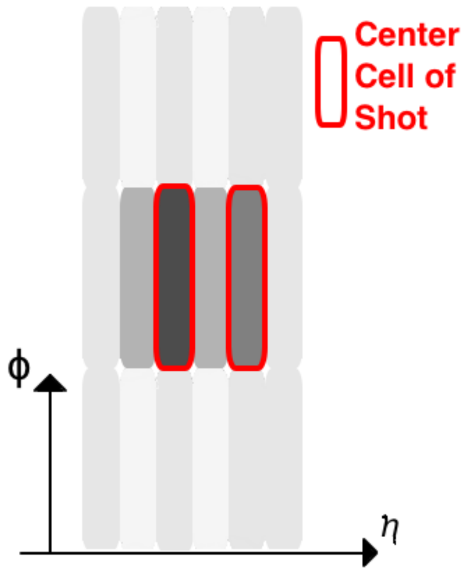

Fig. 4.32: Schematic of a double-shot, which is a case where two shots are created in the same row of cells in ϕ and separated by only one cell in η.

To distinguish between these three cases, the shots are separated into there different categories according to the probability of a shot to be of a certain type in Figure 4.33a. A shot that falls into the low p_T category will be counted as only one photon. A shot that falls into the high p_T category, preliminarily set to $p_T \geq 10$ GeV based on Figure 4.33a, will be automatically counted as two photons. Shots that fall into a medium p_T category have a mixed probability of having been created by one or two photons. The method developed in this thesis is to first categorize shots in the medium p_T category as a double-shot if there is another shot next to it in η that is separated by one cell.

Lateral shower shape variables can be used to distinguish between shots created by 1 or two photons. Table 4.7 shows three of the selected variables. The min(Δp_T) variable is the minimum of the difference in p_T between the second neighboring cell of the center cell of the shot and the first neighboring cell on either side in η of the shot (cf. Equation 4.2, Figures 4.12a and 4.12b). The F_{side} variable is the fraction of p_T that is not in the center of the shot. The $w_{s,5}$ variable is the standard deviation in η of the p_T in the shot and its neighboring two cells in η. A BDT for determining if a shot was created by one or two photons is trained with these variables. The variables were selected so that there is minimal correlation between the variables (see Figure 4.35 for variable correlations). These variables are akin to the strip layer variables used to reconstruct electrons and photons in ATLAS [22]. Figure 4.34 shows the distributions of these variables for shots created by one photon (used as the signal in the training of the BDT) and shots created by two photons (background). The performance of the BDT is shown in Figure 4.36. This figure shows the output score distribution of the BDT and the background rejection vs. signal efficiency for different selection criteria on the BDT. The ideal performance for the BDT is if the BDT score distribution were to show minimal overlap between shots created by one photon (red) and shots created by two photons (blue) and the Kolmogorov-Smirnov test for signal and background close to one, meaning the BDT is not overtrained.

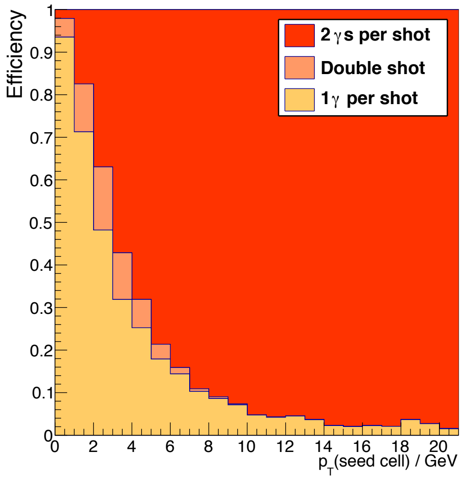

(a) Efficiency of a certain shot type (1 or 2 photons per shot or a double shot), vs. the p_T of the center cell (cf. the p_T spectrum of signal and background shots shown on the right).

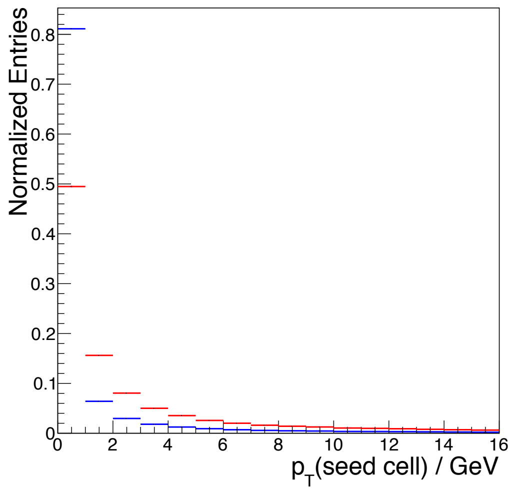

(b) p_T spectrum of truth-matched signal photon shots (red) and background shots (blue).

Fig. 4.33: The p_T spectrum of shot types in the $Z \rightarrow \tau\tau$ sample.

Variable used in the BDT training	Variable used for photon reconstruction at ATLAS [22]
$\min\left(p_T^{\text{1st neighbor}} - p_T^{\text{2nd neighbor}}\right)$	$\Delta E = \left[E^{S1}_{\text{2nd max}} - E^{S1}_{\text{min}}\right]$
$\mathrm{F}_{\text{side}} = \frac{p_T(\pm 2) - p_T(\pm 1)}{p_T(\pm 2)}$	$\mathrm{F}_{\text{side}} = \frac{p_T(\pm 3) - p_T(\pm 1)}{p_T(\pm 1)}$
$w_{s,5} = \sqrt{\frac{\sum p_{T,i}(i - i_\mu)^2}{\sum p_{T,i}}}$	$w_{s,3} = \sqrt{\frac{\sum E_i (i - i_{\text{max}})^2}{\sum E_i}}$

Tab. 4.7: Variables to separate shots created by 1 or 2 photons. The first column shows the variables used in the BDT of this thesis, and the second column shows the related variable from variables used for photon reconstruction at ATLAS [22].

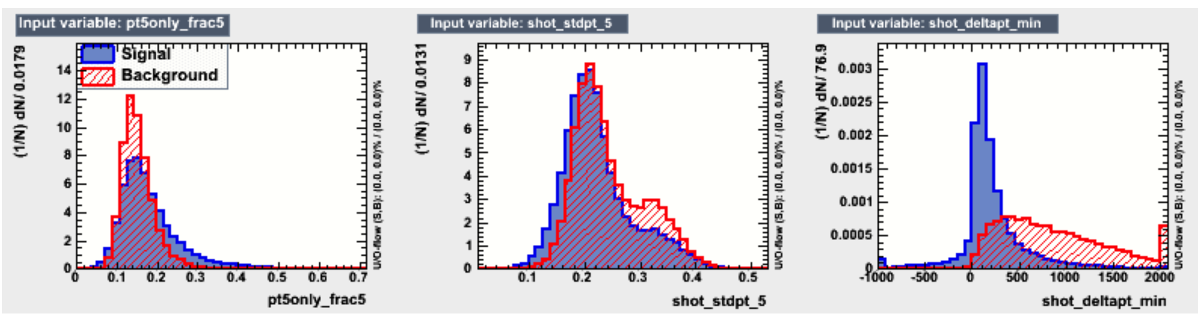

Fig. 4.34: Input variable distributions for the BDT to discriminate between shots created by 1 or 2 photons. Signal is a shot created by one photon, and background is a shot created by two photons. The variables from left to right correspond to the variables shown in Table 4.7 from top to bottom.

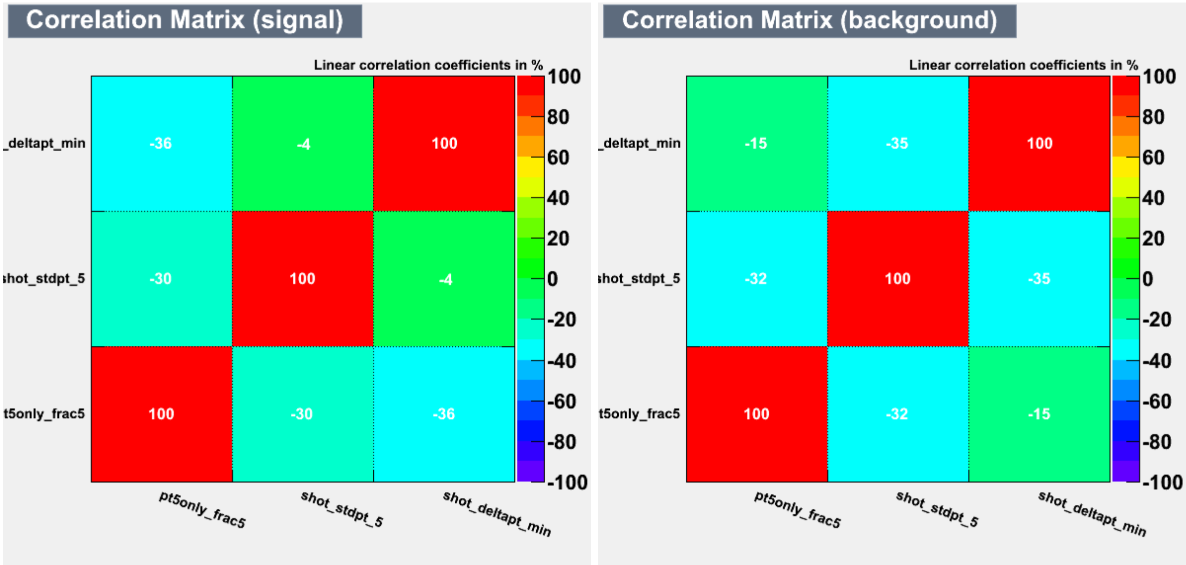

Fig. 4.35: Correlation Matrices of the input variables for signal (left, shot created by one photon) and for background (right, shot created by two photons) used in the BDT to discriminate between shots created by 1 vs. 2 photons.

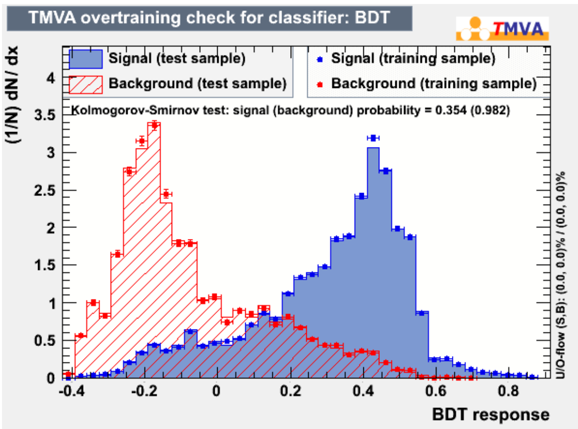

(a) Output score distribution for BDT to discriminate between shots created by 1 vs. 2 photons.

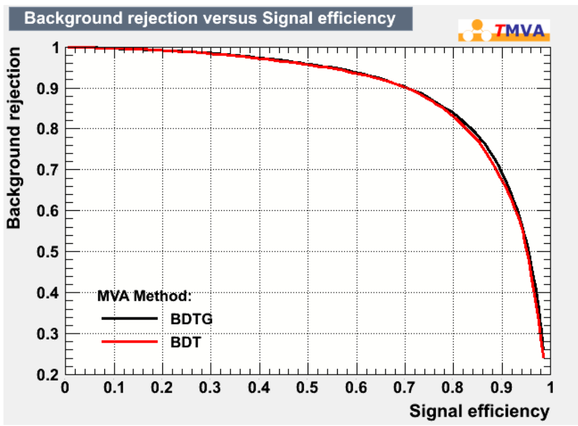

(b) ROC curve showing the signal efficiency vs. background rejection.

Fig. 4.36: Performance of the BDT for discriminating between shots created by 1 vs. 2 photons.

Next, an optimization is performed allowing the p_T threshold, the p_T range for the medium p_T category, and the cut on the BDT score to vary. The optimization varies the parameters to achieve the highest fraction of correctly classified tau decays, i.e., the highest value for the figure of merit described in Equation 4.9. A preliminary look at the performance of the shot categorization by p_T and the BDT is performed on the single π^0 sample. Figure 4.37a shows the efficiency distribution of counting a certain number of photons after categorizing shots with a center cell of p_T above 10 GeV as two photons. Figure 4.37b shows this efficiency distribution for different numbers of photons counted after each shot that makes up a double-shot as one photon, and Figure 4.37c shows this efficiency after applying the BDT discriminator on shots that are not double shots below this region. These figures show that the

BDT is helpful for high p_T neutral pions. However, an optimization of the three steps presented in Figure 4.37 shows that the BDT does not improve the overall figure of merit. This is because the BDT counts too many photons and damages the classification of ρ decays. Given that the ρ decay has the highest branching fraction, it is better to count fewer photons. A preliminary look at the usefulness of the medium p_T threshold in a high mass $Z' \to \tau\tau$, which should contain more cases where one shot is created by two photons, showed that the BDT was also not helpful. Further analyses can be performed to improve the counting of photons using a BDT and p_T categories.

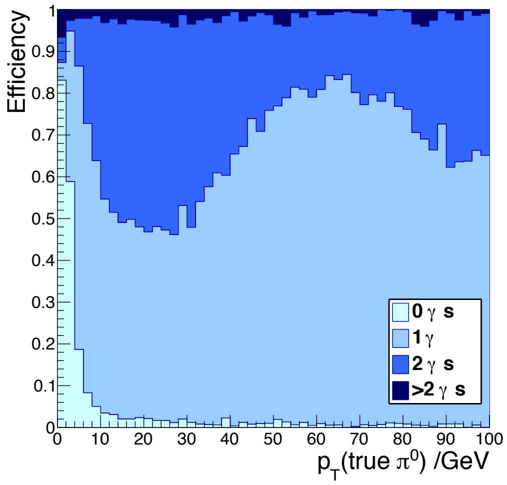

(a) Distribution of the efficiency for counting a certain number of photons after binning in low and high p_T shots vs. the p_T of the true π^0.

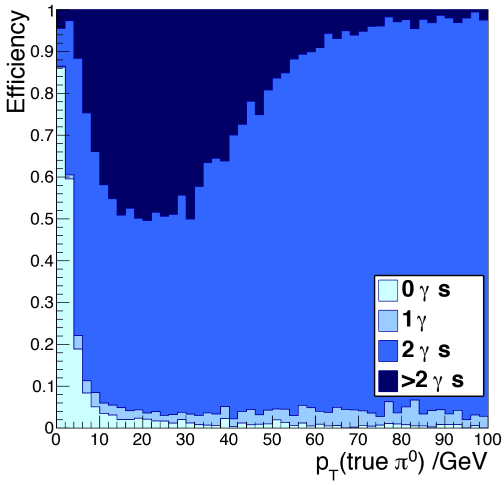

(b) Distribution of the efficiency for counting a certain number of photons after double-shot classification.

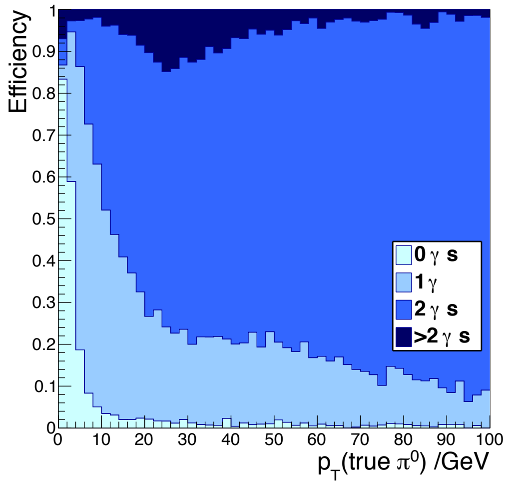

(c) Distribution of the efficiency for counting a certain number of photons after double-shot and BDT classification vs. the p_T of the true π^0.

Fig. 4.37: Distribution of the efficiency for counting a certain number of photons in the single π^0 sample after developments to distinguish between shots created by 1 or 2 photons. The distributions show the performance of the photon shot counting algorithm for the single π^0 sample without pileup where the π^0 is found in the barrel region, $|\eta| < 1.3$.

4.4 Development of a New Approach to the Subtraction of $\pi^{\pm}$ Subshowers Using the Strip Layer

In this section, a new approach to the subtraction of $\pi^{\pm}$ showers is presented. In this approach, showers in the strip layer from the charged pion are identified in the the energy distribution and directly subtracted. The approach is prefaced by the limitations of the cell-based algorithm's subtraction of the charged pion subshower in the strip layer and is followed by ideas for the improvement of the new approach to $\pi^{\pm}$ subshower subtraction developed in this thesis. The analysis in this section uses the $Z \to \tau\tau$ and single $\pi^{\pm}$ samples described in Sections 4.1.1 and 4.1.3, respectively.

As described in Section 3.2.1, the cell-based algorithm uses average hadronic shower shapes to determine how much energy should be subtracted from the cells in ECAL1 and ECAL2 near the track from the $\pi^{\pm}$. These shower shape estimates, however, are not perfect due to the fluctuations in hadronic showers. Figure 4.38 shows the fraction of hadronic energy deposited by a $\pi^{\pm}$ in the strip layer (black line) and the fraction of energy subtracted by the cell-based algorithm (red line). As can be seen, the fraction of energy deposited by a $\pi^{\pm}$ in ECAL1 over the fraction deposited in all layers of the ECAL has many variations, so the cell-based algorithm is limited in subtracting the correct fraction of energy. Moreover, the calculation of the shower shapes in the cell-based algorithm is time-consuming because it integrates over the areas of cells of varying sizes in order to determine the average hadronic shower shape, as shown previously in Equation 3.3. The developments of the new approach will not rely on a time-consuming integration. This will allow the calculation of cell-based variables to run quickly enough to, for instance, assist the tau trigger with making better decisions about which events to write to disk.

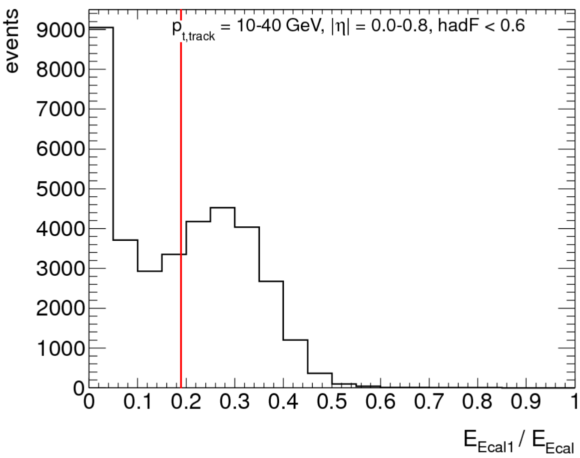

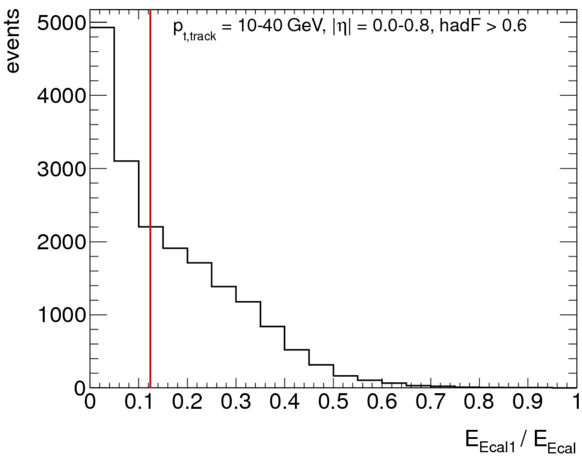

Fig. 4.38: Fluctuations in the fraction of hadronic energy deposited in ECAL1 over the total energy deposited in all layers of the ECAL. The red line indicates the averaged lateral weight from the cell-based algorithm for taus with low hadronic fraction (left) and high hadronic fraction (right). [26]

The cell-based algorithm documented in [26] did not use strip layer information in the subtraction of $\pi^{\pm}$ showers from the strip layer due to the contamination from photon showers. Now, with the advent of shot identification, it is possible to redevelop the cell-based algorithm to identify energy deposits in the strip layer from the $\pi^{\pm}$ using the shot-finding algorithm presented earlier in Section 4.2. Searching for shots created by a $\pi^{\pm}$ is possible since $\pi^{\pm}$ showers in the strip layer are narrow (Figure 4.39 shows an average shower shape of $\pi^{\pm}$ showers in the strip layer), and the distance between a $\pi^{\pm}$ and the closest photon to that $\pi^{\pm}$ is usually larger than the width of a $\pi^{\pm}$ shower in the strip layer. Therefore, the fine granularity of the strip layer means that the energy depositions from the $\pi^{\pm}$ and the photons from a π^0 decay are less likely to overlap in the same cells.

Figure 4.40 shows the ΔR distance between the $\pi^{\pm}$ and the closest γ to that $\pi^{\pm}$. Given the asymmetry between the cell sizes of the strip layer in η and ϕ, a more precise quantification of how often the true $\pi^{\pm}$ and the closest γ to that $\pi^{\pm}$ would be to check the $\Delta\eta$ and $\Delta\phi$ distances. The true $\pi^{\pm}$ and the closest true γ to that $\pi^{\pm}$ are found within a distance of one ϕ cell width and 5 η cell widths about 25% of the time. However, it is important to note that this percentage is an overestimation since the charged pion does not always shower in the strip layer. From Figure 4.11b, the lower bound on the probability of a charged pion to shower in the strip layer is one third because the charged pion deposits $\geq$ 10% of its energy in ECAL1 one third of the time.

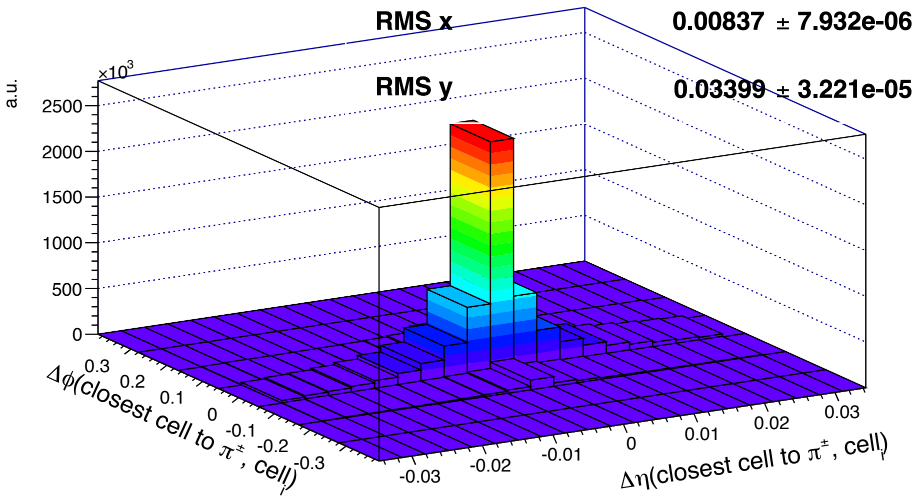

Fig. 4.39: Average shower shape of a $\pi^{\pm}$ in the single $\pi^{\pm}$ sample showering in the strip layer, for tracks found in $|\eta| < 1.3$ only. Each bin corresponds to one strip cell in the barrel region of the ECAL.

Searching for shots from the $\pi^{\pm}$ can help the algorithm determine whether or not the charged pion showered in the strip layer. If the charged pion did not shower in the strip layer, the algorithm should not subtract any energy from the strip layer. However, if the charged pion did shower in the strip layer, then a certain number of cells around the track from the charged pion can be subtracted. The $\pi^{\pm}$ can also leave energy as a minimum ionizing particle through ionization in the strip layer, so not every energy deposition in the strip layer means that the charged pion has started to shower in the strip layer.

The procedure is to find a local maximum in the energy distributions of the strip layer coming from the $\pi^{\pm}$ and then to determine the optimal subtraction setup. The tunable parameters for the subtraction of the $\pi^{\pm}$ from the strip layer are how far apart the extrapolated position of the track to the strip layer and the closest shot to this extrapolated track position can be in order to classify the $\pi^{\pm}$ as having showered in the strip layer and how many cells around the center cell of the shot should be subtracted before experiencing significant contamination from a photon shower.

The first step is to check if the charged pion showered in the strip layer. This is done by checking if there is a shot matched to the track from the charged pion. The furthest distance possible between the track and the closest shot to that track in order to classify the charged pion as having showered in the strip layer is determined using Figure 4.41. This figure shows the distance in η and ϕ between the extrapolated position of the track in the strip layer and the closest shot to that track that is picked up by

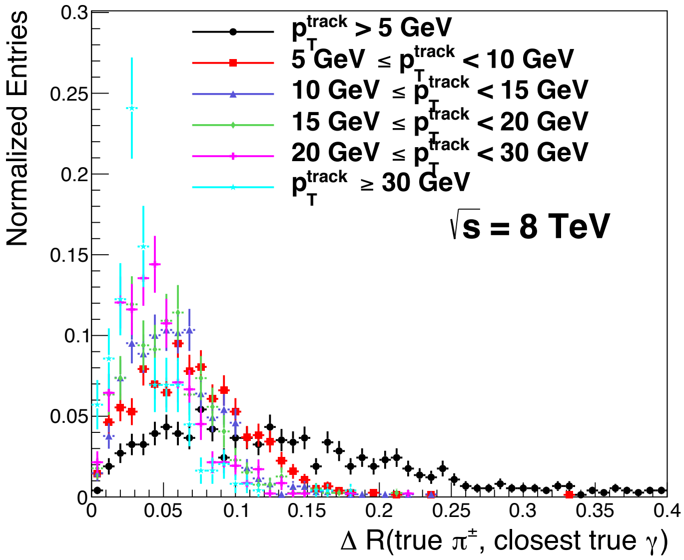

Fig. 4.40: ΔR between the true $\pi^{\pm}$ and the closest γ to that $\pi^{\pm}$ in the $Z \to \tau\tau$ sample for 1-prong decays with at least one neutral pion.

the shot seeding algorithm. For each bin of the track p_T, the entries are normalized to unity, so that the fraction of events where the distance is a certain $\Delta\eta$ for a certain track p_T can be clearly seen. From this figure, a shot in the barrel region of the ECAL should fall within half of a strip cell width and 1.5 times a strip cell width in η.

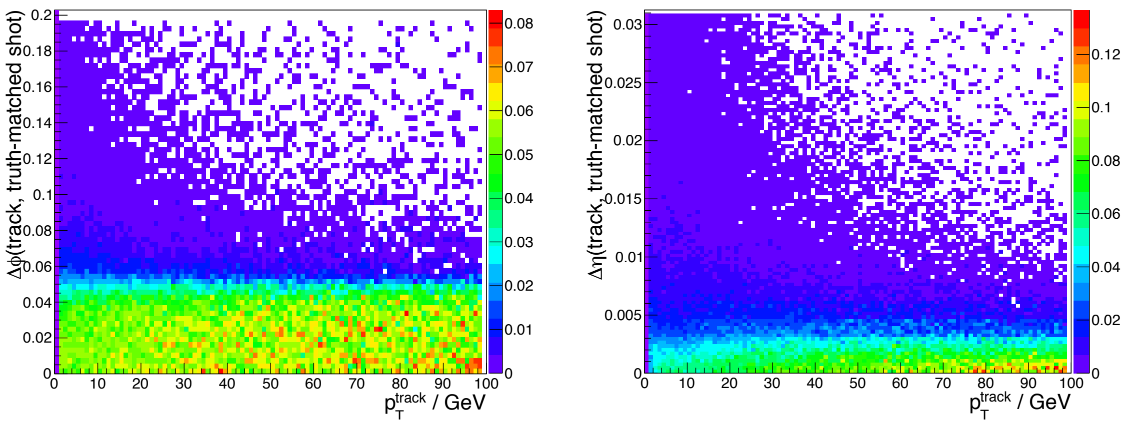

(a) $\Delta\phi$ between track from the $\pi^{\pm}$ and the closest shot to that track, with entries normalized to unity for each track p_T bin.

(b) $\Delta\eta$ between track from the $\pi^{\pm}$ and the closest shot to that track, with entries normalized to unity for each track p_T bin.

Fig. 4.41: Distance between the track from the $\pi^{\pm}$ and the closest shot to that track.

Figure 4.42 shows the probability of a track to be matched to a charged pion using the shot-to-track-matching requirements explained previously.

The cell-based algorithm can already be significantly improved by being apprised of whether or not

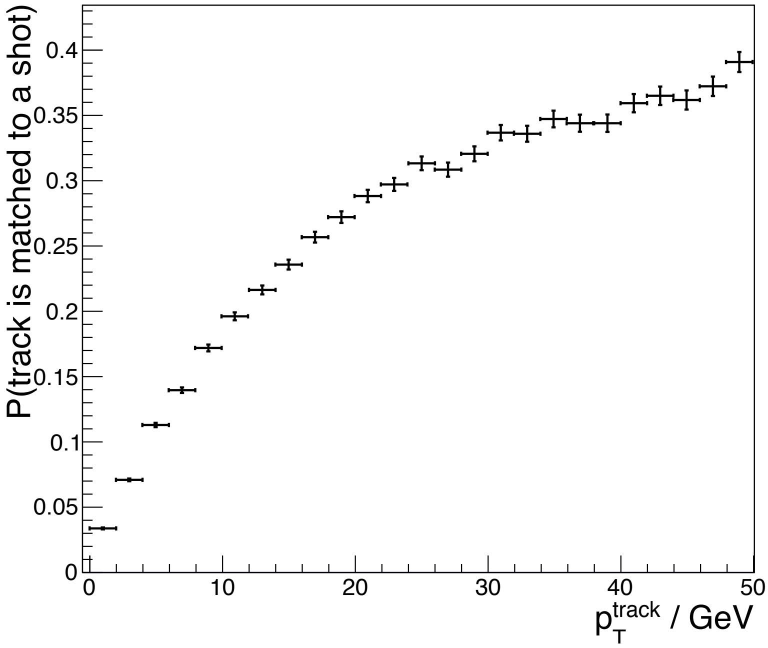

Fig. 4.42: Probability of a track from the $\pi^{\pm}$ to be matched to a shot in the strip layer in the single $\pi^{\pm}$ sample, for tracks found in $|\eta| < 1.3$ only. A threshold of 100 MeV used for the shot seeding (cf. Section 4.2) was placed on the shot.

the $\pi^{\pm}$ has showered in the strip layer. This reduces the running time of the algorithm, since calculating shower shapes in ECAL1 take the longest time, due to the high density of cells. Also, it keeps the algorithm from subtracting too much energy from the strip layer if the charged pion has not even showered there.

For the cases where the $\pi^{\pm}$ does create a shot in the strip layer, the next step is to determine the number of cells associated to this shot whose energy should be subtracted from the strip layer. Although hadronic showers are typically wide, the start of a $\pi^{\pm}$ shower in the first layer of the ECAL is narrow. The hadrons created in the hadronic shower have not yet passed enough interaction lengths in the detector to deposit a significant amount of energy in the strip layer.

The goal is to determine the number of cells needed to contain the $\pi^{\pm}$ shower, on average, without subtracting energy deposits from the photons. The setup for the number of cells to subtract can be determined by associating an incremental number of cells to the shot and comparing the p_T contained by these cells for different one prong decay modes of the taus in the $Z \to \tau\tau$ sample. If the p_T contained in an incrementally larger cell area is similar to that for tau decays with $\geq$0 neutral pions and tau decays with no neutrals, it means that cell area did not contain energy contributions from the π^0. Then, it would be safe to associate these to the $\pi^{\pm}$. Figure 4.43 shows the p_T contained by the cells moving progressively away from the center cell of the shot in η for the single $\pi^{\pm}$ sample and the different one prong decay modes of the $Z \to \tau\tau$ sample. If additional p_T is not measured for the decay modes with neutral pion(s) than for those without s dπ^0, it means this cell area did not experience leakage from a photon showerIt shows that the additional p_T measured when including neighboring cells in η, comparing decay modes with and without neutral pions, is on the order of MeV. In addition, the additional p_T does not increase when increasing the cell area from associating one neighboring cell on either side of the center seed cell in η to two neighboring cells.

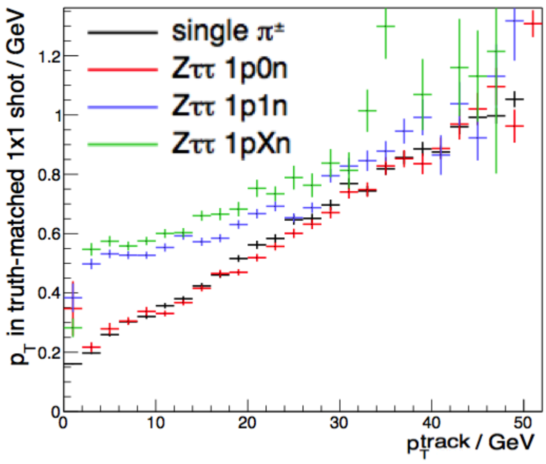

(a) Transverse momentum contained by the center cell of the $\pi^\pm$ shot for the $\pi^\pm$ sample and the different decay modes in the $Z \to \tau\tau$ sample, where the true charged pion is found in the barrel region of the ECAL.

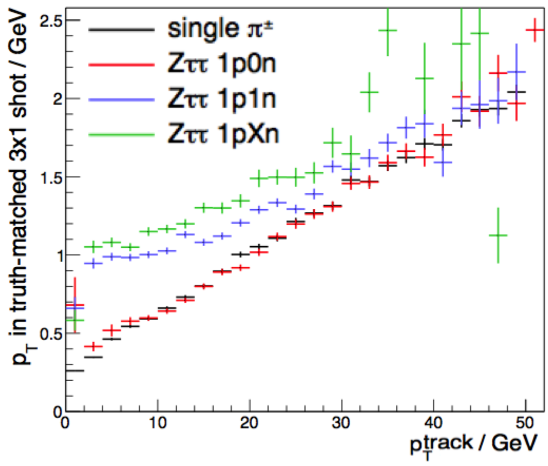

(b) Transverse momentum contained by the seed cell of a $\pi^\pm$ shot and its neighboring cells on either side in η (3×1 shot). Shown for the $\pi^\pm$ sample and the different decay modes in the $Z \to \tau\tau$ sample, where the true charged pion is found in the barrel region of the ECAL.

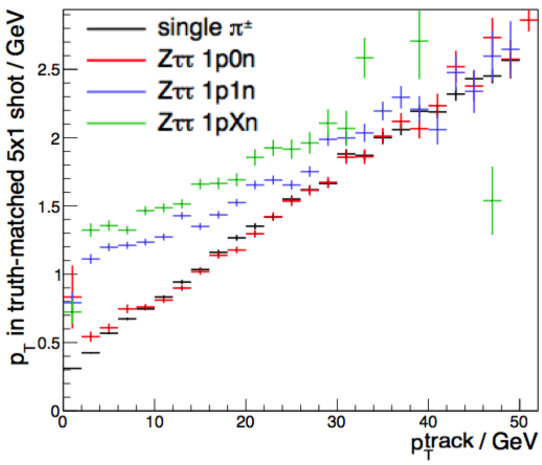

(c) Transverse momentum contained by the seed cell of a $\pi^\pm$ shot and its two neighboring cells either side in η (5×1 shot). Shown for the $\pi^\pm$ sample and the different decay modes in the $Z \to \tau\tau$ sample, where the true charged pion is found in the barrel region of the ECAL.

Fig. 4.43: Transverse momentum contained by $\pi^\pm$ shot for the $\pi^\pm$ sample and the different decay modes in the $Z \to \tau\tau$ sample.

However, Figure 4.43 suggests that the $\pi^\pm$ shots contain leakage from neutral pions. The p_T contained in even the center cell of a shot is larger for tau decays with neutral pions in the $Z \to \tau\tau$ sample. To verify this, Figure 4.44 shows the efficiency to find a $\pi^\pm$ shot for the different decay modes of the tau. If the efficiency of a $\pi^\pm$ to make a shot is higher for tau decays with neutral pions than it is for tau decays without neutral pions, then the algorithm is picking up shots with contamination from photon showers.

Because the photon showers can be mistakenly identified as a $\pi^\pm$ shot, the feasibility for constraining

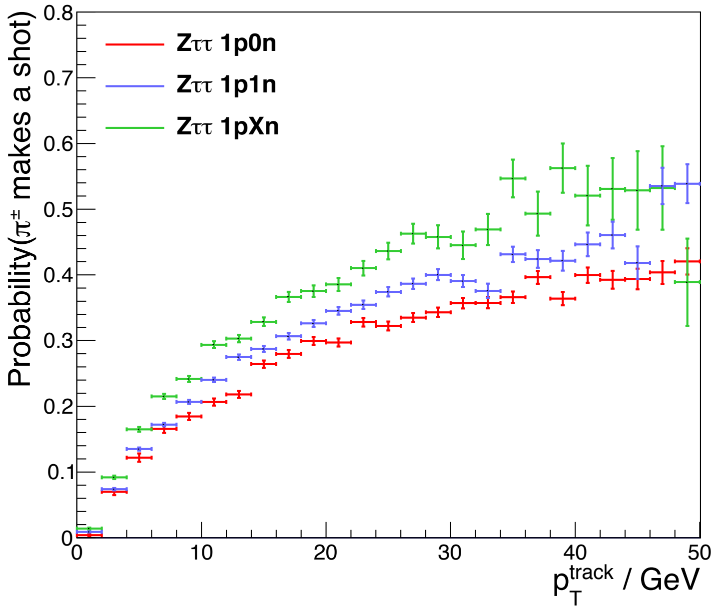

Fig. 4.44: Probability of a $\pi^{\pm}$ to make a shot for different tau decay modes in the $Z \to \tau\tau$ sample, for tracks found in $|\eta| < 1.3$ only.

the method of $\pi^{\pm}$ shot finding using several variables is investigated. First, the probability of a charged pion to make a shot can be predicted by the fraction of energy found in the HCAL, which includes the ECAL (see Section 3.2.1), over the p_T of the track. Figure 4.45 shows the hadronic fraction binned by the p_T of the track. Figure 4.46 shows the p_T contained in the center cell and its first neighbor cells in η over the p_T of the track. The variables show discriminating power. For example, if a tau has a large fraction of p_T in the HCAL over the track p_T, it is likely to not have showered in the strip layer. Therefore, placing a threshold on this fraction, above which the $\pi^{\pm}$ should not have showered in the strip layer since a larger fraction of energy in the HCAL means the $\pi^{\pm}$ showered later in the calorimeter, constrains the $\pi^{\pm}$ shot. Likewise, if the fraction of the shot p_T over the p_T of the track is above a certain threshold, it is likely to contain contamination from a photon shower, so discarding $\pi^{\pm}$ shots with a fraction above this threshold further constrains the $\pi^{\pm}$ shot. The optimization of these thresholds and additional variables will be investigated in future improvements planned for the algorithm. Also, the threshold placed on, for example, the center cell of the shot should also be optimized according to the p_T of the track.

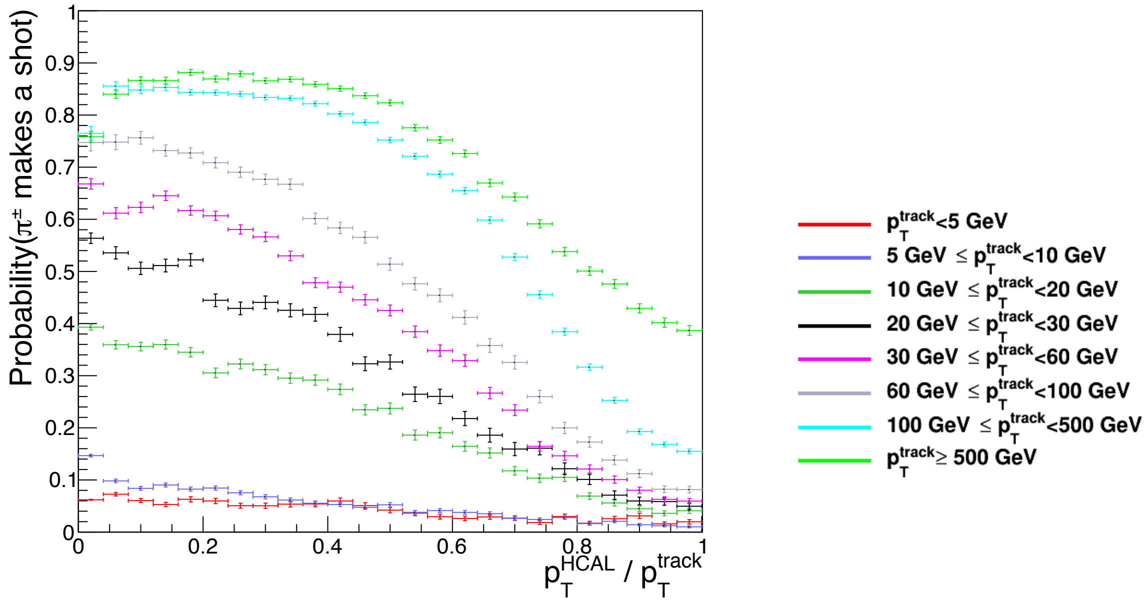

Fig. 4.45: Probability of a $\pi^{\pm}$ to make a shot for different bins of hadronic fraction in the single $\pi^{\pm}$ sample, for tracks found in $|\eta| < 1.3$ only. A threshold of 100 MeV used for the shot seeding (cf. Section 4.2) was placed on the shot.

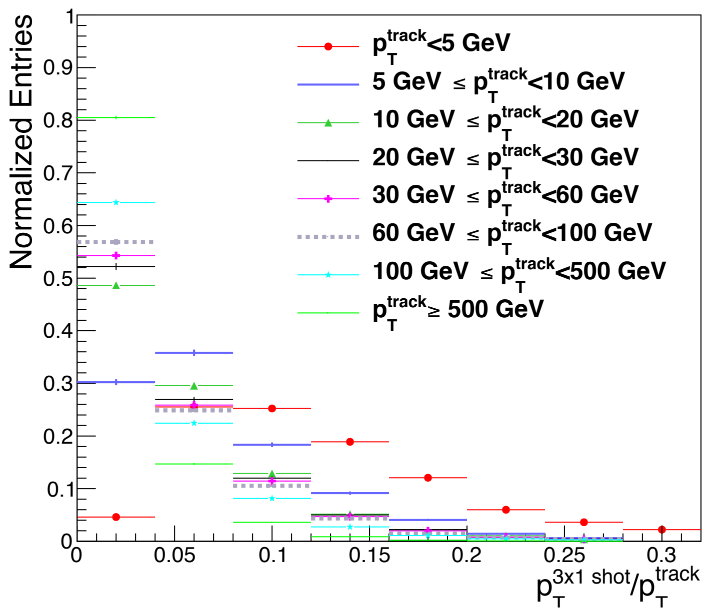

Fig. 4.46: Fraction of p_T found in a 3×1 shot over p_T of the track in the single $\pi^{\pm}$ sample, for tracks found in $|\eta| < 1.3$ only. A threshold of 100 MeV used for the shot seeding (cf. Section 4.2) was placed on the shot.

4.5 Feasibility of an Alternative Approach to π^0 Reconstruction in τ Decays

The current approach to tau substructure reconstruction is to first subtract deposits in the calorimeters from a charged pion and then to identify neutral pions in the remaining energy distribution. In this section, the feasibility of an alternative approach wherein showers from a π^0 decay would be predicted from strip layer information without subtracting showers from the $\pi^\pm$ is studied. The advantage of this approach is twofold. First, electromagnetic showers from π^0 decays fluctuate less than hadronic showers since they only involve one process (electromagnetic). Second, this would evade the problem of subtraction of $\pi^\pm$ showers since the subtraction is performed in order to reconstruct showers from the π^0 shower. On the other hand, the advantage of the cell-based ansatz is that this method can use information from the entire ECAL (after subtraction of the $\pi^\pm$ shower from the ECAL), whereas the alternative approach would not use information from ECAL2, which suffers from large contamination from $\pi^\pm$ showers.

This section uses the single π^0 sample to measure an upper bound on the resolution of the p_T of the π^0 that can be obtained by predicting showers from a π^0 decay. The p_T in the strip layer is calibrated with the p_T of the true π^0 using half of the single π^0 sample (the second half is used to test the resolution obtained by this calibration). The most ideal setup is used to contain the electromagnetic shower in order to calibrate the p_T in the strip layer. Therefore, the p_T of all cells found in a $\Delta R = 0.2$ cone around the true π^0 is summed up. Noise should not be a problem in summing up the cells because the total noise in the ECAL is on the order of a few hundred MeV (see Figure A.3 in the Appendix). This approach is done as a preliminary check of the feasibility of predicting the p_T of the π^0 from only ECAL1 information. A more realistic setup would need to be developed to quantify ECAL1 information in the form of a shot if an upper bound on the resolution of the p_T of the π^0 obtained in an ideal setup is comparable to the resolution obtained by current tau reconstruction algorithms described in [20, 26]. Figure 4.47a shows the p_T of the true π^0 vs. the corresponding sum of p_T found in all the cells in the strip layer in a ΔR<0.2 cone around the true π^0, denoted as p_T^{ECAL1}.

To obtain a calibration curve from Figure 4.47a, the average value in each p_T bin is taken. Figure 4.47b shows the average value at each p_T bin. The errors shown are the error on the mean and not the spread of distribution. A third-order polynomial is fit to this curve, allowing parameter values, p_i, to vary:

$$p_T^{\text{predicted for }\pi^0} = p_0 + p_1 \cdot p_T^{\text{ECAL1}} + p_2 \cdot \left(p_T^{\text{ECAL1}}\right)^2 + p_2 \cdot \left(p_T^{\text{ECAL1}}\right)^3 . \tag{4.10}$$

Figure 4.47b shows the fit and the best fit parameters. The fit has a $\frac{\chi^2}{\text{ndf}}$, where ndf is the number of degrees of freedom, value of 3.8. A good fit would have a $\frac{\chi^2}{\text{ndf}}$ value of close to 1, but, in this case, it is the error in the resolution from fluctuations in the electromagnetic shower, and not the statistical errors, that dominate the smearing of the energy resolution. Further studies have to be performed to extend the fit to higher p_T regions.

4.5.1 Energy and p_T Resolution

To measure the resolution of the predicted p_T of the π^0, the second half of the sample is used to measure the resolution obtained after this calibration. This means there is no bias caused by using the same data from calibration to measure the resolution resolution obtained from that calibration. The p_T resolution

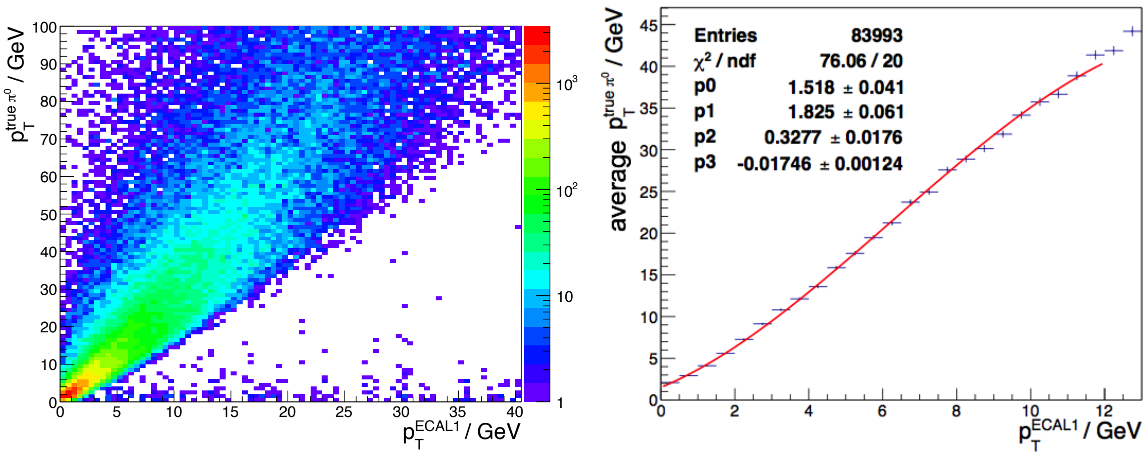

(a) p_T in strip layer vs. p_T of the true π^0. p_T^{ECAL1} denotes the sum of the p_T found in all the cells in the strip layer in a ΔR<0.2 cone around the true π^0.

(b) Calibration curve of p_T in the strip layer to the p_T of the true π^0.

Fig. 4.47: Prediction of the p_T of the π^0 using solely strip layer information

is defined as

$$\delta p_T = \frac{p_T^{\text{true}\,\pi^0} - p_T^{\text{predicted}}}{p_T^{\text{true}\,\pi^0}}, \tag{4.11}$$

where $p_T^{\text{predicted}}$ comes from Equation 4.10, and the input is the p_T found in all cells in a $\Delta R = 0.2$ cone around the generated position of the neutral pion. Figure 4.48a shows the p_T resolution. For now, this thesis concentrates on the p_T region expected for neutral pions from taus from a $Z \to \tau\tau$ decay, so the resolution shown in Figure 4.48a is measured for events where the p_T in the strip layer is less than 10 GeV. For comparison, the performance of current algorithms that first subtract the charged pion, is shown in Figure 4.48b [20, 26]. Possible improvements to the p_T resolution using presampler information are discussed next.

The relative energy resolution is also measured to verify whether the degradation in the p_T resolution is dominated by the energy resolution of the calorimeter (see Section 2.4.1). If the resolution shows a $\sqrt{E}$ dependence, then the degradation depends on the resolution of the sampling calorimeter. To verify this, Figure 4.49 shows the RMS value of $E^{\text{predicted}} - E^{\text{true}\,\pi^0}$ in 2 GeV wide bins of $E^{\text{true}\,\pi^0}$. $E^{\text{predicted}}$ is determined using the 4-vector of the π^0. The p_T component of this 4-vector if the calibrated p_T, and the η and ϕ of this 4-vector for the π^0 are the η and ϕ of the closest cluster to the generated position of the true π^0. The difference between the predicted energy and the energy of the true π^0 is divided by $\sqrt{E^{\text{true}\,\pi^0}}$ to check for a dependence on the calorimeter resolution. If this dependence is dominant, the relative resolution should be uniform and not show a dependence on $\frac{1}{\sqrt{E}}$.

Figure 4.49 shows the relative energy resolution obtained using only strip layer information. The relative energy resolution fluctuates around a horizontal line. These fluctuations are hypothesized to come from differences in the longitudinal containment of the shower from the neutral pion. To investigate this effect, information from the presampler can be used.

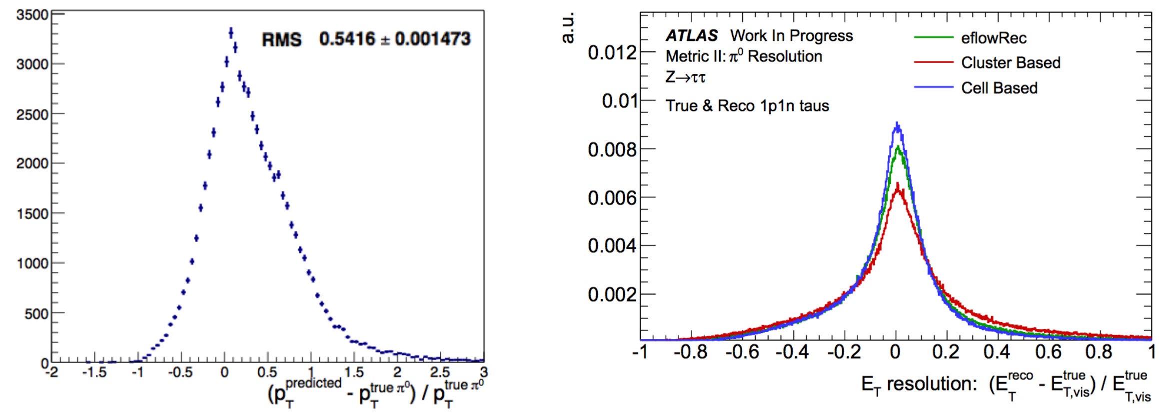

(a) Resolution of the p_T of the π^0 obtained using strip layer information to predict showers from a π^0 decay in the single π^0 sample.

(b) p_T resolution of current tau reconstruction algorithms [20, 26, 27, 31].

Fig. 4.48: Resolution for the prediction of the p_T of the π^0 using solely strip layer information.

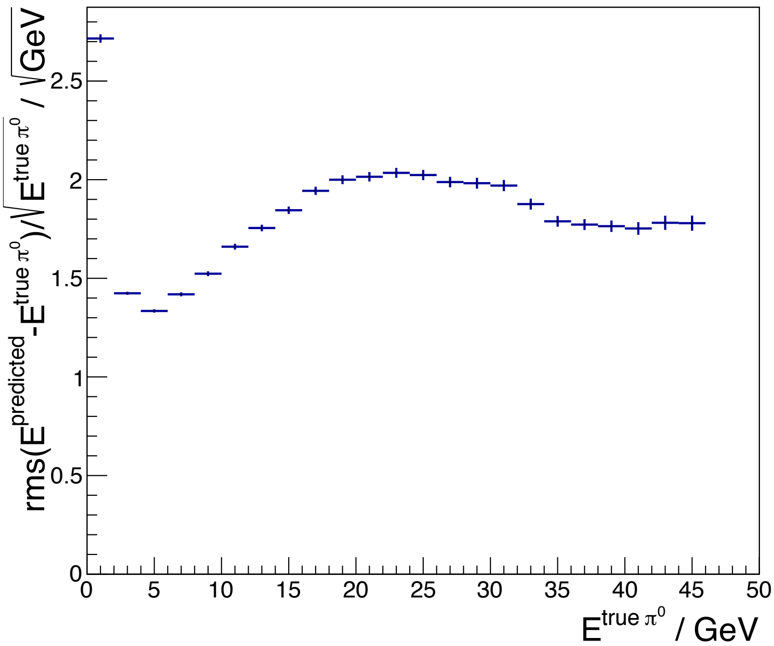

Fig. 4.49: The relative π^0 energy resolution obtained using strip layer information to predict showers from a π^0 decay in the single π^0 sample.

4.5.2 Outlook of the Alternative Approach

The resolution obtained by predicting π^0 showers from strip layer information can be further improved with a combined fit where information from the cell-based algorithm is also used. It can also be improved by using presampler information to determine whether the photon started to shower before hitting the strip layer. The presampler can range from 3 to 5 interaction lengths, depending on η, so there is a probability that the photons from the π^0 decay begin to shower in the presampler. Thus, two categories could be defined to further constrain the calibration: events with and without a presampler hit. Thorough investigations of how a presampler hit should be defined would need to be performed if presampler information is used for the alternative approach.

The measurement presented in this section of an upper bound of the π^0 p_T resolution that can be obtained from strip layer information shows more work would have to be done in order for the alternative approach to perform on par with current substructure algorithms. In the future, more time could be invested into a combined fit. This would involve using information from the current cell-based method, where $\pi^\pm$ showers are subtracted first, in addition to strip layer information. Also, a precise quantification of a presampler hit could be investigated to better constrain the calibration of the p_T in the strip layer. The performance of the algorithms using the ansatz of first subtracting the $\pi^\pm$ [20, 26] have the advantage of being able to use information from the entire ECAL after subtraction of the $\pi^\pm$ shower from the ECAL, whereas the alternative approach proposed in this section is limited to using information from the earliest layers of the ECAL since it cannot use ECAL2, which contains contamination from the $\pi^\pm$.

Chapter 5

Outlook

This section presents future plans for the work presented in this thesis. The new reconstruction object called the "shot" is still in its infancy and can be further honed to improve tau reconstruction and help in analyses related to taus. In addition, since the analyses were performed entirely on Monte Carlo simulated samples, the algorithms developed in this thesis need to be validated with real data.

5.1 Validation between Monte Carlo and Data

A comparison of the photon shot seeding algorithm (presented in Section 4.2) with data is currently in preparation. Systematic errors will be evaluated using samples simulated with different shower models and different detector geometries. They can be used to checked if the algorithm, for example, counts a consistent number of shots in the different data samples. Also, the tag-and probe method [27] can be used to select $Z \rightarrow \tau\tau$ events in data from the LHC. This method selects $Z \rightarrow \tau\tau$ events where one tau decays to muons (tag) and the other decays hadronically (probe). Since muons leave a clean, identifiable signature in the ATLAS detector, the method can search for a nicely reconstructed muon. With the tag-and-probe method, an unbiased sample of hadronically decaying taus to study properties such as energy scale and tau identification.

5.2 Ideas for Further Improvement of the Algorithms Presented in This Thesis

The algorithms developed already show promising performance. Ideas for further improvements are:

- Split the first η bin of $|\eta| < 1.3$ into two η bins according to the amount of detector material shown in Figure A.1a. A more suitable η binning would be $|\eta| < 0.8$ and $0.8 \leq |\eta| < 1.5$. For the endcap region, preliminary extension of the shot finding algorithm and the tau decay mode classification using shots was performed in this thesis. However, the extension to the endcap can be improved by using a seeding algorithm optimized for the sizes of the cells in the endcap.

- Using the decay kinematics of the tau to discriminate between signal and background photon shots. For example, a shrinking cone (a cone size that is predicted by the track p_T) can be used to veto π^0 clusters outside the shrinking cone, so shots found within these clusters will not be identified.

- Investigate categorization of shots by p_T further to more accurately count shots that come from two photons vs. shots that come from on photon. It may still be possible to count photons more accurately in order to improve tau decay mode classification.

- Test the shot-counting algorithm for different number of vertices to measure the effect of pileup.

- Continue analysis of the new subtraction method. First, investigate the optimal track to shot-matching criteria to improve the subtraction of charged pions in the strip layer using shots. Second, optimize the best setup for the subtraction of charged pions in the strip layer with shots using variables such as the hadronic fraction and the ratio between the p_T of the shot matched to the track and the p_T of the track.

- Measure feasibility of alternative approach at high p_T since calorimeter resolution improves with increasing p_T. Check if presampler information can improve the resolution of π^0 p_T obtained by predicting π^0 showers from strip layer information in the alternative approach (see Section 4.5). It is necessary to precisely define what a presampler hit is to check whether a photon has showered in the presampler. This could minimize the fluctuations in longitudinal developments of the photon showers from the π^0 that degrade the resolution of the energy predicted by using only strip layer information.

- Optimize the usage of shots in PanTau. Currently, PanTau uses the number of shots as a discriminating variable, and the decay mode of the tau is automatically set to 1pXn if the tau was migrated by the photon shot counting algorithm presented in this thesis.

- Although photon conversions should not be a major problem for the shot-seeding algorithm, the fraction of cases where the e^+e^- products of a photon conversion that would create two photon shots could be handled using a photon conversion finder. This would allow the algorithm to better count the number of photons using photon shots.

5.3 Ideas for Future Uses of the Photon Shot

The photon shot is still in its infancy and can be further exploited for other tau reconstruction goals.

- Photon shots can improve the identification of clusters created by a π^0. For example, π^0 showers have a characteristic p_T fraction in the strip layer, and using longitudinal information can improve the identification of clusters from π^0.

- Photon shots can be extended for use in jet reconstruction algorithms in ATLAS, such as eflowRec [20].

- Photon shots can be used to improve tau identification. For example, the number of high p_T photon shots counted outside of the tau cone can be used to discriminate against multijet background, since a hadronically decaying tau should have decay products contained in an isolation cone.

Chapter 6

Conclusions

Tau leptons are important signatures in searches for new physics at the LHC and studies of the SM Higgs boson. Algorithms for the reconstruction and identification of tau leptons that decay hadronically have been in development in the past few years and can be further improved before use for Run 2 data at the LHC. The reconstruction of neutral pions from a hadronically decaying tau is integral to these algorithms. It can be used to better classify the different hadronic tau decay modes. Neutral pion reconstruction can also benefit analyses that use measurements of the tau polarization since these measurements at the LHC rely on the $\tau \to \rho\nu_\tau$ decay, and this requires a reliable decay mode classification. In addition, it can improve the four-momentum resolution of reconstructed taus by separating hadronic clusters from electromagnetic cluster, the latter stemming from $\pi^0 \to \gamma\gamma$ decays. Lastly, neutral pion reconstruction can improve tau identification by helping the algorithm to better predict backgrounds for the different tau decay modes.

The cell-based algorithm used in this thesis reconstruct subshowers from neutral pions by searching in the energy distributions leftover in the electromagnetic calorimeter after the removal of energy depositions from charged pions. This thesis proposes an algorithm to improve the cell-based algorithm's reconstruction of neutral pions in hadronic 1-prong tau decays. The algorithm identifies individual photons from neutral pions in hadronic 1-prong tau decays by searching for local maxima in the energy distributions of the strip layer, or photon shots. This algorithm is applicable in the cell-based algorithm for 50% of the cases where a tau has been incorrectly reconstructed as having had only one neutral pion in its decay when it actually had more than one neutral pion. If there are greater than two shots found, then the tau is classified as a 1-prong decay with more than two neutral pions. Otherwise, it is classified as a tau decay involving one neutral pion. For 1-prong tau decays in the barrel region of the electromagnetic calorimeter, the number of neutral pions with the application of the shot-finding algorithm can be counted correctly for about 69% of the $\tau^\pm \to \pi^\pm\pi^0\nu_\tau$ decays and about 55% of the $\tau^\pm \to \pi^\pm(\geq 2\pi^0)\nu_\tau$ decays. This is an improvement from 70% and 46%, respectively, from the cell-based algorithm before the application of the shots. Further improvements to the shot-counting method were investigated to distinguish between cases where shots are created by one vs. two photons, and these improvements may be useful in a sample with high p_T taus, such as a Z' sample.

Additional applications of strip layer information were investigated toward the end of this thesis. This thesis presents an analysis of the redevelopment of the subtraction of the cell-based $\pi^\pm$ energy subtraction in the strip layer to rely on shots created by the charged pion, instead of using average hadronic shower shapes to estimate the longitudinal shower development. The advantages of this approach include an improvement in algorithm runtime and a better estimate of whether or not the charged pion has showered in the strip layer. A preliminary setup using charged pion shots is now being prepared for implementation into the tau reconstruction software in ATLAS, and its performance will be evaluated. Finally, the feasibility of another application of the photon shot to predict π^0 showers in second layer of the electromagnetic calorimeter instead of searching for neutral pions after subtracting energy deposits from the charged pion. An upper bound on the p_T resolution that can be obtained with this new approach is measured and can be further improved using a combined fit with information provided by the cell-based subtraction of the $\pi^{\pm}$ and by using information from the presampler.

Plans for the first validation of the analyses presented in this thesis in a comparison between Monte Carlo and data are in preparation. The work presented in this thesis contains versatile promise. Its applications in downstream algorithms, such as tau identification and PanTau, are currently under study and optimization. Strip layer information in the form of a shot will be incorporated into π^0 algorithms for use in Run 2 at the LHC.

Appendix A

Relevant Properties of the ATLAS Detector

A.1 Segmentation of the Calorimeters at ATLAS

	Longitudinal Segementation	Coverage in $\|\eta\|$	Lateral Segmentation: Granularity ($\Delta\eta \times \Delta\phi$)
Electromagnetic Calorimeter (Barrel)	Presampler	$\|\eta\|<1.52$	0.025×0.1
	1st layer (strip layer)	$\|\eta\|<1.40$	$0.025/8 \times 0.1$
		$1.40<\|\eta\|<1.475$	0.025×0.025
	2nd layer	$\|\eta\|<1.40$	0.025×0.025
		$1.40<\|\eta\|<1.475$	0.075×0.025
	3rd layer	$\|\eta\|<1.35$	0.050×0.025
Electromagnetic Calorimeter (Endcap)	Presampler	$1.5 < \|\eta\| < 1.8$	0.025×0.1
	1st layer (strip layer)	$1.375 <\|\eta\| < 1.425$	0.025×0.1
		$1.5 < \|\eta\| < 1.8$	$0.025/8 \times 0.1$
		$1.8 < \|\eta\| < 2.0$	0.004×0.1
		$2.0 < \|\eta\| < 2.5$	0.006×0.1
		$2.5 < \|\eta\| < 3.2$	0.1×0.1
	2nd layer	$1.375 < \|\eta\| < 2.5$	0.025×0.025
		$2.5 < \|\eta\| < 3.2$	0.1×0.1
	3rd layer	$1.5 < \|\eta\| < 2.5$	0.5×0.025

Tab. A.1: Segementation of the ATLAS Calorimeters. The strip layer is shown in red, except for the crack region, which is shown in gray. [19].

A.2 Amount of Material in the ATLAS Detector

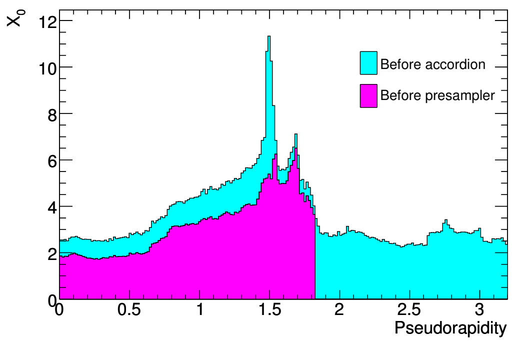

(a) Amount of material, before the presampler and the ECAL accordion vs. Pseudorapidity [19].

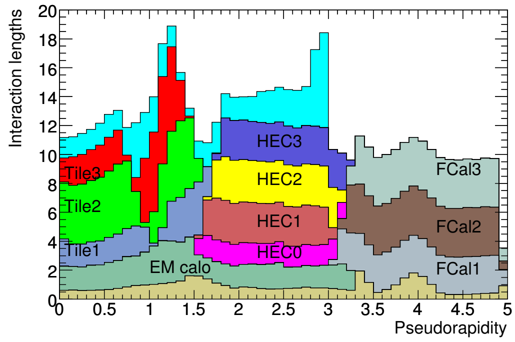

(b) Amount of material in front of each subcomponent of the detector from the ECAL outward vs. Pseudorapidity[19].

Fig. A.1: Amount of material before each subcomponent of the detector.

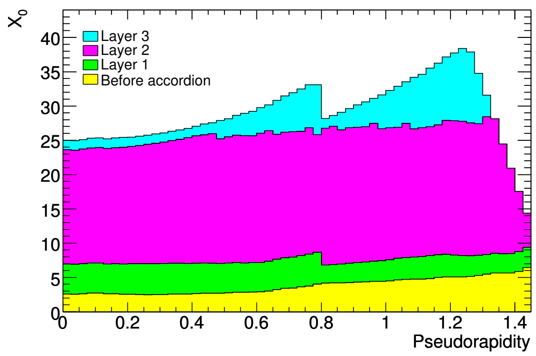

(a) Amount of material of each layer of the ECAL (barrel) vs. Pseudorapidity [19].

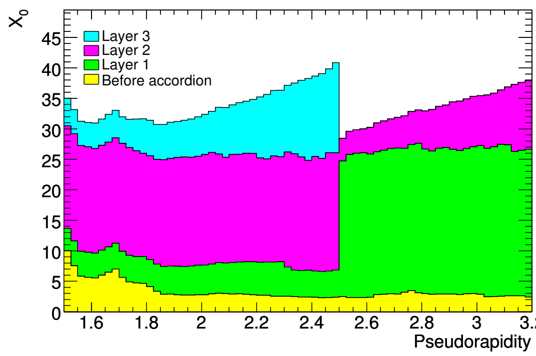

(b) Amount of material, in units of radiation length, of each layer of the ECAL (end cap) vs. Pseudorapidity [19].

Fig. A.2: Length of each layer of the electromagnetic calorimeter.

A.3 Noise in the ATLAS Detector

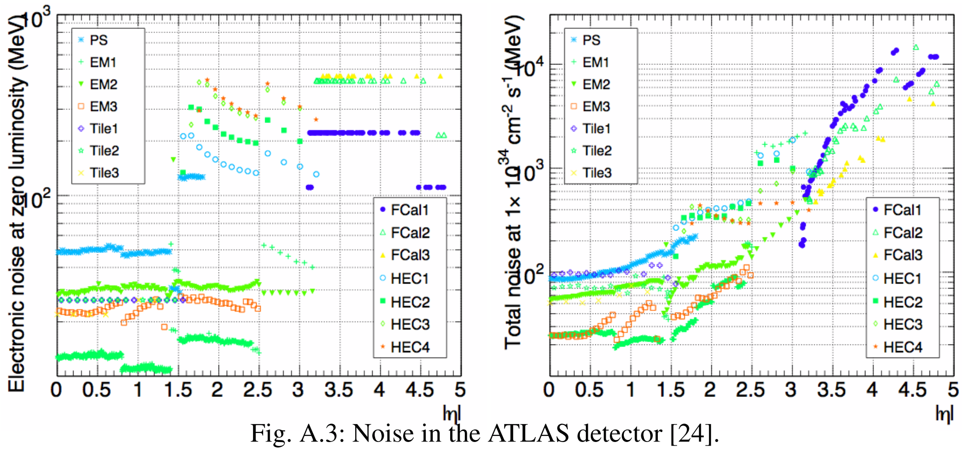

Fig. A.3: Noise in the ATLAS detector [24].

Appendix B

Variables Used for π^0 cluster Identification in the Cell-Based Algorithm

Symbol	Description
ETA_CLUSTER	Pseudorapidity of the cluster
SECOND_R	Second moment in distance to the shower axis*
SECOND_LAMBDA	Second moment in distance to the shower center along the shower axis*
Abs_DELTA_PHI	ϕ difference of the shower axis and the vector pointing from the Reconstructed primary vertex (PW) to the shower center*
Abs_DELTA_THETA	θ difference of the shower axis and the vector pointing from the PW to the shower center*
CENTER_LAMBDA_helped	Distance of the shower center from the calorimeter front face measured along the shower axis*
LATERAL	Normalized second lateral moment*
LONGITUDINAL	Normalized second longitudinal moment*
ENG_FRAC_EM	Fraction of energy in EM calorimeter accordion* (for this case: Ecal1 and Ecal2)
ENG_FRAC_MAX	Energy fraction in the most energetic cell*
ENG_FRAC_CORE	Sum of the energy fractions in the most energetic cells per sampling*
$\log\left\langle (E/V)^2 \right\rangle$	Logarithm of the second moment in energy density*
$\frac{E_{\mathrm{core}}}{E_{\mathrm{Ecal1}}}$	Energy in three innermost Ecal1 cells normalized to total energy in Ecal1
AsymmetryWRTTrack	Asymmetry of energy distribution in Ecal1 with respect to the Extrapolated track position
NPosCells_EM1	Number of cells with positive energy in Ecal1
NPosCells_EM2	Number of cells with positive energy in Ecal2
$\lvert\langle\eta\rangle\rvert_{\mathrm{Ecal1}}$	First moment in pseudorapidity in Ecal1
$\lvert\langle\eta\rangle\rvert_{\mathrm{Ecal2}}$	First moment in pseudorapidity in Ecal2
$\left\langle\eta^2\right\rangle_{\mathrm{Ecal1}}$	Second moment in pseudorapidity in Ecal1
$\left\langle\eta^2\right\rangle_{\mathrm{Ecal2}}$	Second moment in pseudorapidity in Ecal2

Tab. B.1: Variables used to identify neutral pion clusters [26]. The formulas of the variables marked with an asterisk are defined in [35].

List of Figures

1.1 The Higgs Potential 5
1.2 Example Feynman diagram of the τ^- decaying via the weak interaction. 8
1.3 The preferred decay kinematics in the $\tau \to \pi\nu_\tau$ decay 9
1.4 The preferred decay kinematics in the $\tau^- \to \rho^-\overline{\nu}_\tau$ decay 10
1.5 The preferred decay kinematics in the $Z \to \tau\tau$ decay 10
1.6 The preferred decay kinematics in the $H \to \tau\tau$ decay 10

2.1 Schematic of the LHC accelerator complex 14
2.2 Onion layer schematic of the ATLAS detector showing the principal sub detectors. . . 16
2.3 Transverse momentum resolution of single charged pions in the ATLAS calorimeter and tracking systems 18
2.4 Schematic of the subcomponents of the calorimeter system 19
2.5 Schematic of a module of the ECAL barrel 21

3.1 Schematic of a hadronically decaying tau in the ATLAS detector 23
3.2 Schematic of the tau isolation cone. 24
3.3 Examples of longitudinal and lateral shower shapes used in the cell-based algorithm . . 27

4.1 Number of primary vertices in the $Z \to \tau\tau$ sample with pileup 30
4.2 The η and p_T spectra of reconstructed taus in the $Z \to \tau\tau$ sample 30
4.3 The p_T spectra of the visible tau decay product in the $Z \to \tau\tau$ sample 31
4.4 The η and p_T spectra of the true neutral pions in the single π^0 sample. 32
4.5 Number of reconstructed tracks per event in the single $\pi^\pm$ sample. 33
4.6 The η and p_T spectra of the true charged pions in the single $\pi^\pm$ sample. 33
4.7 An average photon shower shape in the strip layer the ECAL 34
4.8 Display of a tau event in the strip layer 35
4.9 Opening angle between the photons of a π^0 decay 36
4.10 Fraction of π^0 p_T in ECAL1/2 36
4.11 Fraction of $\pi^\pm$ p_T deposited on average in each layer of the calorimeters 37
4.12 Schematic of local maximum cases. 39
4.13 The Δp_T variable (Equation 4.2) vs. p_T of the second neighboring cell to the seed cell . 39
4.14 Display of an event in the $Z \to \tau\tau$ sample where a photon creates two shots across ϕ. . 40
4.15 Schematics of the ϕ-matching setups considered. 40
4.16 Distance between a photon and the closest shot to that photon 42
4.17 Display of a tau event after truth-matching of shots to photons. 42
4.18 Efficiency of the seeding algorithm to pick up a shot from a photon 44
4.19 Asymmetry in p_T between the lower p_T photon and the higher p_T photon in a π^0 decay 44
4.20 Purity obtained by the shot-finding algorithm before ϕ-matching. 45
4.21 Purity obtained by the shot-finding algorithm after ϕ-matching 46
4.22 Distance in the strip layer between the photon conversion products 47

4.23 Matrices for the cell-based algorithm before shots. 49
4.25 Number of photons matched to a selected cluster for taus decaying to 1pXn that have been wrongly reconstructed as 1p1n 49
4.24 Display of an event where photons from two neutral pions are found in the same cluster 50
4.26 Efficiency of shot counting in the single π^0 sample 52
4.27 Efficiency of shot counting in 1p1n decays from the $Z \to \tau\tau$ sample 53
4.28 Distribution of shot counting in 1pXn decays from the $Z \to \tau\tau$ sample 54
4.29 Matrices for cell-based algorithm after shots, $|\eta| < 1.3$. 55
4.30 Matrices for cell-based algorithm before/after shots, $1.5 \leq |\eta| < 1.8$. 55
4.31 Matrices for cell-based algorithm before/after shots, $|\eta| \geq 1.8$ 56
4.32 Schematic of a double-shot 57
4.33 The p_T spectrum of shot types. 58
4.34 Input variable distributions for the BDT to discriminate between shots created by 1 or 2 photons 58
4.35 Correlation matrices of the input variables for signal and for background used in the BDT to discriminate between shots created by 1 vs. 2 photons 59
4.36 Performance of the BDT for discriminating between shots created by 1 vs. 2 photons. . 59
4.37 Efficiency of shot counting after further developments. 61
4.38 Fluctuations in the fraction of hadronic energy in ECAL1. 62
4.39 Average shower shape of a $\pi^\pm$ showering in the strip layer 63
4.40 ΔR between the true $\pi^\pm$ and the closest γ 64
4.41 Distance between a track and a $\pi^\pm$ shot. 64
4.42 Probability of a $\pi^\pm$ to make a shot 65
4.43 Transverse momentum in a $\pi^\pm$ shot 66
4.44 Probability of a $\pi^\pm$ to make a shot for different tau decay modes 67
4.45 Probability of a $\pi^\pm$ to make a shot for different bins of hadronic fraction 68
4.46 Fraction of p_T found in a shot over p_T of the track 68
4.47 Prediction of the p_T of the π^0 using solely strip layer information 70
4.48 Resolution for the prediction of the p_T of the π^0 using solely strip layer information. . 71
4.49 Relative π^0 energy resolution using only strip layer information 71

A.1 Amount of material before each subcomponent of the detector. 78
A.2 Length of each layer of the electromagnetic calorimeter. 78
A.3 Noise in the ATLAS detector 79

List of Tables

1.1 The fundamental forces and their properties. 3
1.2 The fermions and their properties 4
1.3 Decay modes and branching fractions of the tau lepton 7

3.1 Optimized cuts on π^0 cluster from the cell-based algorithm 27

4.1 Selection efficiencies for the $Z \rightarrow \tau\tau$ sample with pileup. 31
4.2 Selection efficiencies for the single π^0 sample without pileup. 32
4.3 ϕ-matching: Percent gain for different $\Delta\eta \times \Delta\phi$ setups. 41
4.4 ϕ-matching: Percent loss for different window sizes 41
4.5 Thresholds on the p_T of the center cell of a shot for different η regions. 52
4.6 Results of the improvement of τ decay mode classification. 56
4.7 Variables to train a BDT that distinguishes between shots created by one or two photons 58

A.1 Segmentation of the ATLAS Calorimeters 77

B.1 Variables used to identify neutral pion clusters in the cell-based algorithm 81

Bibliography

[1] The ATLAS Collaboration, "Observation of a new particle in the search for the Standard Model Higgs boson with the {ATLAS} detector at the {LHC}", *Physics Letters B* 716.1 (2012) 1 –29, ISSN: 0370-2693, DOI: http://dx.doi.org/10.1016/j.physletb.2012.08.020.

[2] The CMS Collaboration, "Observation of a new boson at a mass of 125 GeV with the {CMS} experiment at the {LHC}", *Physics Letters B* 716.1 (2012) 30 –61, ISSN: 0370-2693, DOI: http://dx.doi.org/10.1016/j.physletb.2012.08.021.

[3] P. W. Higgs, "Broken Symmetries and the Masses of Gauge Bosons", *Phys. Rev. Lett.* 13 (16 1964) 508–509, DOI: 10.1103/PhysRevLett.13.508, URL: http://link.aps.org/doi/10.1103/PhysRevLett.13.508.

[4] Particle Data Group, J. Beringer et al., "Review of Particle Physics", *Phys. Rev. D* 86 (2012) 010001, URL: http://pdg.lbl.gov.

[5] S. L. Glashow, "Partial-symmetries of weak interactions", *Nuclear Physics* 22.4 (1961) 579 –588, ISSN: 0029-5582, DOI: http://dx.doi.org/10.1016/0029-5582(61)90469-2, URL: http://www.sciencedirect.com/science/article/pii/0029558261904692.

[6] A. Salam, "Gauge unification of fundamental forces", *Rev. Mod. Phys.* 52 (3 1980) 525–538, DOI: 10.1103/RevModPhys.52.525, URL: http://link.aps.org/doi/10.1103/RevModPhys.52.525.

[7] S. Weinberg, "Conceptual Foundations of the Unified Theory of Weak and Electromagnetic Interactions", *Rev.Mod.Phys.* 52 (1980) 515–523, DOI: 10.1103/RevModPhys.52.515.

[8] P. Higgs, "Broken symmetries, massless particles and gauge fields", *Physics Letters* 12.2 (1964) 132 –133, ISSN: 0031-9163, DOI: http://dx.doi.org/10.1016/0031-9163(64)91136-9, URL: http://www.sciencedirect.com/science/article/pii/0031916364911369.

[9] P. W. Higgs, "Spontaneous Symmetry Breakdown without Massless Bosons", *Phys. Rev.* 145 (4 1966) 1156–1163, DOI: 10.1103/PhysRev.145.1156, URL: http://link.aps.org/doi/10.1103/PhysRev.145.1156.

[10] Nobel Media AB, *The Nobel Prize in Physics 1983*, URL: http://www.nobelprize.org/nobel_prizes/physics/laureates/1984/.

[11] NASA, *Dark Energy, Dark Matter - NASA Science Dark Energy, Dark Matter - NASA Science Dark Energy, Dark Matter - NASA Science Dark Energy, Dark Matter*, URL: science.nasa.gov.

[12] M. L. Perl et al., "Evidence for Anomalous Lepton Production in $e^+ - e^-$ Annihilation", *Phys. Rev. Lett.* 35 (22 1975) 1489–1492, DOI: 10.1103/PhysRevLett.35.1489, URL: http://link.aps.org/doi/10.1103/PhysRevLett.35.1489.

[13] Nobel Media AB, *The Nobel Prize in Physics 1995*,
URL: http://www.nobelprize.org/nobel_prizes/physics/laureates/1995/.

[14] A. Stahl, *Physics with Tau Leptons*, Springer, 2000.

[15] The ATLAS Collaboration, "Measurement of τ polarization in $W \to \tau\nu$ decays with the ATLAS detector in pp collisions at $\sqrt(s) = 7$ TeV", *Eur.Phys.J.* C72 (2012) 2062,
DOI: 10.1140/epjc/s10052-012-2062-6, arXiv: 1204.6720 [hep-ex].

[16] T. Nattermann, K. Desch, P. Wienemann, and C. Zendler,
"Measuring tau-polarisation in neutralino2 decays at the LHC",
J. High Energy Phys. 04.arXiv:0903.0714 (2008) 057. 16 p.

[17] R Garoby, "Upgrade Issues for the CERN Accelerator Complex",
LHC-PROJECT-Report-1110. CERN-LHC-PROJECT-Report-1110 (2008) 6 p.

[18] CERN Press Release, *Two circulating beams bring first collisions in the LHC Two circulating beams bring first collisions in the LHC Two circulating beams bring first collisions in the LHC Two circulating beams bring first collisions in the LHC*,
URL: http://press.web.cern.ch/press-releases/2009/11/two-circulating-beams-bring-first-collisions-lhc.

[19] The ATLAS Collaboration, "The ATLAS Experiment at the CERN Large Hadron Collider", *JINST* 3.8 (2008) S08003, DOI: 10.1088/1748-0221/3/08/S08003.

[20] M Hodgkinson, D Tovey and R Duxfield, "Energy Flow Reconstruction with the eflowRec Combined Reconstruction Software in Athena 15.6.9.8", tech. rep. ATL-PHYS-INT-2011-031, Geneva: CERN, 2011.

[21] M Capeans et al., "ATLAS Insertable B-Layer Technical Design Report",
tech. rep. CERN-LHCC-2010-013. ATLAS-TDR-19, Geneva: CERN, 2010.

[22] The ATLAS Collaboration, "Measurement of the inclusive isolated prompt photon cross section in pp collisions at $\sqrt{s} = 7$ TeV with the ATLAS detector", *Phys. Rev. D* 83.5 (2011) 052005,
DOI: 10.1103/PhysRevD.83.052005.

[23] P. Giovannini and the ATLAS Liquid Argon Calorimeter Group,
"Local hadron calibration with ATLAS",
Journal of Physics: Conference Series 293.1 (2011) 012057,
URL: http://stacks.iop.org/1742-6596/293/i=1/a=012057.

[24] W Lampl et al., "Calorimeter Clustering Algorithms: Description and Performance",
tech. rep. ATL-LARG-PUB-2008-002. ATL-COM-LARG-2008-003, Geneva: CERN, 2008.

[25] W. Lampl et al., "Digitization of LAr calorimeter for CSC simulations" (2007).

[26] B. T. Winter,
"Reconstruction of neutral pions in hadronic tau lepton decays in the ATLAS detector",
Master Thesis, Universität Bonn, 2012.

[27] The ATLAS Collaboration,
"Performance of the Reconstruction and Identification of Hadronic Tau Decays with ATLAS",
tech. rep. ATLAS-CONF-2011-152, Geneva: CERN, 2011.

[28] M. Cacciari, G. P. Salam and G. Soyez, "The anti-k_t jet clustering algorithm",
Journal of High Energy Physics 2008.04 (2008) 063,
URL: http://stacks.iop.org/1126-6708/2008/i=04/a=063.

[29] F. Friedrich, “Tau Lepton Reconstruction and Identification at ATLAS”, tech. rep. ATL-PHYS-PROC-2012-025, Geneva: CERN, 2012.

[30] A. Hocker et al., “TMVA - Toolkit for Multivariate Data Analysis”, *PoS* ACAT (2007) 040, arXiv: `physics/0703039 [PHYSICS]`.

[31] S. Fleischmann, “Tau Lepton Reconstruction with Energy Flow and the Search for R-Parity-Violating Supersymmetry at the ATLAS Experiment”, PhD Thesis, Universität Bonn, 2011, URL: `http://pi.physik.uni-bonn.de/pi_plone/lhc-ilc/view.php?lang=de&c=t&id=20`.

[32] V. Scharf, “Neutral Pion Subshower Reconstruction in Hadronic Tau Lepton Decays at the ATLAS experiment”, Master Thesis, Ruprecht-Karls-Universität Heidelberg, 2009.

[33] T. Sjostrand, S. Mrenna and P. Z. Skands, “A Brief Introduction to PYTHIA 8.1”, *Comput.Phys.Commun.* 178 (2008) 852–867, DOI: `10.1016/j.cpc.2008.01.036`, arXiv: `0710.3820 [hep-ph]`.

[34] T. Sjostrand, S. Mrenna and P. Z. Skands, “PYTHIA 6.4 Physics and Manual”, *JHEP* 0605 (2006) 026, DOI: `10.1088/1126-6708/2006/05/026`, arXiv: `hep-ph/0603175 [hep-ph]`.

[35] S. Menke, *Cluster Moments*, URL: `https://twiki.cern.ch`.

I hereby certify that the work presented here was accomplished by myself and without the use of illegitimate means or support, and that no sources and tools were used other than those cited.

Bonn, ...

Date Signature